**BERGISCHE
UNIVERSITÄT
WUPPERTAL**

Computational Insights into Ion Mobility Spectrometry and Electrospray Ionization

Dissertation

zur Erlangung des akademischen Grades
Doktor der Naturwissenschaften (Dr. rer. nat.)

Vorgelegt von
Robin Hillen
geboren in Mettmann, Deutschland

Bergische Universität Wuppertal
Fakultät 4 - Mathematik und Naturwissenschaften
Physikalische und Theoretische Chemie
unter der Anleitung von
Prof. Dr. Thorsten Benter

Wuppertal, November 2023

"In the realm of knowledge, curiosity is the compass, and science the journey."

ChatGPT

Danksagung

In erster Linie möchte ich mich bei Prof. Dr. Thorsten Benter und Dr. Walter Wißdorf bedanken, ohne die diese Arbeit nicht möglich gewesen wäre! Vielen Dank für die sehr schöne Zusammenarbeit.

Außerdem bedanke ich mich bei dem großartigen Team der PTC, dass sich über die Jahre immer wieder verändert und weiterentwickelt hat und dabei nicht an Großartigkeit verloren hat.

Insbesondere möchte ich Joshi, Clara und Markus erwähnen, mit denen ich viele schöne Momente, in unserer gemeinsamen Zeit an der BUW, erleben durfte.

Ein letztes, großes Dankeschön geht an meine Familie für die Unterstützung und an Katja für den bedingungslosen Rückhalt all die Jahre!

Für Karin, Bernd & Katja.

Abstract

The topic of the work is the description of the ion dynamics within ion mobility devices as well as electrospray ion sources under different conditions. Depending on the question, various properties of the ions are determined as precisely as possible, e.g. their kinetic energy or reduced ion mobility. For this purpose, the pressure and flow profiles of the background gas are first determined and then used as input parameters for subsequent ion dynamics simulations. To model the neutral gas flow properties, either the continuum model or the Direct Simulation Monte Carlo (DSMC) approach are used. This is represented by the two programs OpenFOAM and SPARTA. For the ion trajectory calculations, SIMION is mostly used, in addition to a customized SPARTA version of the SPARTA framework. Overall, this work consists of three parts:

In the first part, a new method for the calculation of reduced ion mobilities and therefore drift velocities in a high-kinetic energy ion mobility spectrometer (HiKE-IMS) is presented. The main feature of this method is that within one simulation run, not only the ions and background gas particles and their interactions are calculated simultaneously, but also simulation parameters as the electric field can be adjusted during runtime. Subsequently, the ion mobility is determined using an example species, and then the effects of relevant simulation parameters on the results are described. In addition, other species are considered, and the calculated results are compared with the data from the literature.

The next part describes a method for determining the effect of a specific ion transfer system (for transporting ions form a HiKE device into a mass spectrometer) on the transferred ions. In this context, a two- and three-dimensional models are compared with each other with regard to the neutral gas flow properties. The obtained results are then used to analyze the ion trajectories in detail with respect to the kinetics and collision energies.

The third part presents an approach for determining the size distribution of droplets, which are formed within the electrospray ionization (ESI) process, in dependence of the induced ESI current. It is shown that the existing experimental setup can be extended by the possibility of characterizing charged droplets via the recording of induced cur-

rent transients. The simulations presented suggest that with existing hardware, such as an oscilloscope in combination with a common current amplifier, it is possible to detect droplets with approximately 10 000 charges. In addition, an evaporation model is successfully integrated into an existing collision model, to obtain more comprehensive results.

Acronyms

E/N	reduced field strength
m/z	mass-to-charge
AP	atmospheric pressure
CAD	computer aided design
CM	control mass
CRM	charge residue model
CV	control volume
DC	direct current
DSMC	direct simulation monte carlo
ESI	electrospray ionization
FD	finite difference
FE	finite element
FV	finite volume
GND	ground (electrical)
HiKE	high kinetic energy
HS	hard sphere
IEM	ion evaporation model
IMS	ion mobility spectrometer
MS	mass spectrometer
OpenFOAM	open source field operation and manipulation framework
POL	plot over line
QIT	quadrupole ion trap
RAM	random access memory
RF	radio frequency
SDS	statistical diffusion simulation
SPARA	SPARTA Result Analysis
SPARTA	stochastic parallel rarefied-gas time-accurate analyzer
TOF	time of flight
VHS	variable hard sphere
VSS	variable soft sphere

Contents

1. Scope of this Work

The scope of the present work is - in the widest sense - the calculation of the ion dynamics in different fields of application. It is mainly about an accurate description of ion trajectories and other ion properties, e.g. their reduced mobility. For this purpose, the pressure and flow profiles of electrically neutral background gas are determined for different simulation cases and then used as input parameters for subsequent ion dynamics simulations. This approach will be discussed with three major sections.

The first part discusses the determination of the reduced ion mobility for different species in different background gases. All calculations are performed in one simulation framework, namely SPARTA, which is based on the Direct Simulation Monte Carlo (DSMC) approach. A novel aspect of this approach are the custom extensions to SPARTA, which are required to allow such simulations with this program. The objective is not only to determine the effect of the background gas particles on the ions, but at the same time to model the effect of the ion motion on the background gas.

The second part discusses the details of the ion dynamics in a transfer stage between an ion mobility spectrometer (IMS) and a mass spectrometer (MS). The primary aspect here are the collision dynamics, the average collision energy and hence the effective temperature of the ions in the transfer stage. In this section some notable differences between a two- and three-dimensional model are highlighted. In addition, the integration of neutral gas flow properties into a subsequent ion trajectory simulation is described.

The last part addresses the investigation of the dynamics of large, charged liquid droplets generated by electrospray ionization (ESI). This is partly shown in models based on a simplified version of an ion source of a commercially available mass spectrometer. Special emphasis is placed on a more comprehensive description of the system in this section of the thesis. An existing evaporation model is incorporated into a collision model. In addition, challenges of transferring input data and results from one program to another are discussed.

In summary, three different programs or frameworks are used. These differ in the underlying theoretical concept and cover different application areas.

2. Software Packages

This chapter provides a brief overview of the simulation programs and pre- and post-processing tools used in this work.

2.1. SPARTA

SPARTA is the acronym for *Stochastic Parallel Rarefied-gas Time-accurate Analyzer*. It is a parallel Direct Simulation Monte Carlo (DSMC) code for performing simulations of low-density gases in two- or three-dimensional space [1]. The DSMC method was developed by Graeme Bird [2] and is widely used for large-scale rarefied gas flows (a more detailed description of the DSMC method is be found in section 3.1) The method has a wide field of applications. For example, it can be used to model the gas flow around spacecrafts during atmospheric reentry [3] or to model some basic phenomena such as the Rayleigh-Taylor instability [4]. The DSMC method, and thus SPARTA, is also able to describe gas flows in the transition regime between continuum and free-molecular flow [1]. The particle density is too low to fulfill the continuum requirements in this regime. One option to consider this in a simulation is to model the gas as individual particles and not as a continuum. Simultaneously, the particle density is too high to neglect particle particle interactions contrary to free-molecular flows. The DSMC method is able to model both aspects with a comparably small number of simulated particles in a simulation. The SPARTA code can model chemical reactions, collisions, energy transfer, and chemical reactions. The chemical reactions and the particle-particle collision models are based on a statistical approach. To reduce the computational demands, the simulation domain is separated into grid cells, and only particles in the same grid cell can interact with each other. Therefore, every simulated particle is characterized by its potential internal energy, velocity, and spatial coordinates besides the internal parameters,e.g., mass and chemical species. The collisions between particles are calculated with dedicated collision models. The variable hard sphere model (VHS) [5] and the variable soft sphere model (VSS) [6] (see section 3.5.3) are implemented in SPARTA for this purpose. Both are more accurate than the basic hard sphere (HS) model, since they consider

energy-dependent collision cross sections. Additionally, the VSS model accounts for the variable diffusion cross section and is more precise than the VHS model [7]. The DSMC model is valid as long as the underlining statistical model is valid. Therefore, the number of particles needs to be large enough to be statistically significant and the timestep and the grid cell size need to be adjusted to the given particle density (for more details, see section 4.4.1).

The SPARTA framework is designed to handle large numbers of particles and is therefore optimized for parallel computing. Geometries can be defined via text-based input files or be imported from CAD projects. The simulation grid can be adjusted in resolution in specific areas and adaptive resolution refining is possible during runtime. There is a wide variety of boundary conditions available to describe particle dynamics at walls and simulation domain boundaries, such as inflow and outflow, reflections, and periodic conditions. There are many options to receive the simulation results: The results can be exported per time step and averaged over grid and time, to get spatial or temporal averages and to condense the size of the output files. Additionally, there is a set of Python scripts called *pizza.py* available for pre- and post-processing. It allows to convert the data into the Paraview [8] PVD file format, and then the PyVista [9] library is used to read the generated PVD files.

2.2. OpenFOAM

OpenFOAM is the acronym for *Open Source Field Operation and Manipulation framework* that includes besides simulation executables approximately 100 C++ libraries. The framework contains two categories: The solvers that are designed to solve a specific problem in fluid or continuum mechanics (for a more detailed view, see section 3.2) and the utilities, which are designed to perform simple pre- and post-processing tasks, mainly involving data manipulation tasks and algebraic calculations. The solvers in OpenFOAM cover a wide range of problems in fluid dynamics, e.g., compressible gas flows with turbulence like the *rhoSimpleFoam* solver [10]. OpenFOAM is commonly used for problems which involve the prediction of fluid motion and forces, for example, the modeling of turbines or air conditioning systems. The OpenFOAM framework can be used to solve numerical problems in fluid dynamics, including heat and some basic thermodynamics, with the finite volume method [11].

Depending on the problem and the solver, pressure, velocity, and temperature within the simulation domain are the main calculated properties of the fluid. For many solvers,

additional properties are also part of the solution. The spatial region is discretized by a calculation mesh, which can be regular or irregular. An irregular mesh can include areas with a more precise resolution and areas with fewer, depending on the problem and the underlying geometry. In addition, there are many different boundary conditions available which could be applied to the simulation domain, such as in- and outflow regions or simple walls. The framework also allows changes in the geometry or the mesh during runtime [11]. Like in other codes, the geometry can be defined via simple text files or imported form CAD projects. The mesh generation is done externally or via OpenFOAM utilities, such as the simple *blockMesh* or the more advanced *snappyHexMesh* programs. The output data are processed with a customized version of ParaView [8], which is called paraFoam. This version is extended to easily access and visualize the simulation output. The output files are mostly delimited text files, which store the fluid properties in each cell of the grid [10].

2.3. SIMION

SIMION 8.1 (Scientific Instrument Services, Inc., Ringeos, NJ) is a software for the simulation of the dynamics of charged particles in electromagnetic fields. The main application field is mass spectrometry or related applications, e.g., ion mobility spectrometry (IMS). The electrode/magnetic pole geometries can be defined via a SIMION specific scripting language which allows the construction of complex geometries from geometric primitives or be imported form CAD models. Parts of the geometry can be declared as electrodes in electrostatic simulations, from which the resulting electric field is calculated. SIMION solves electromagnetic fields with a finite difference method approach (cf. section 3.3.1). The solution for each defined electrode is stored separately in so called *potential arrays*. The total resulting field can be constructed by a linear combination of each electrode solution. The applied electrode potentials act as scaling factors of the linear combination and can be quickly adjusted during runtime, without having to recalculate the entire field. This enables the possibility to apply time-dependent changes in the electric field by changing only the scaling factors during a simulation run.

Integration of charged particle trajectories is done with a Runge-Kutta method [12]. The timestep length is related to the grid resolution of the potential array and can be adjusted with the so-called trajectory quality parameter.

Additionally, SIMION has a Lua [13] programming interface, which can execute so-called user programs, which in turn facilitates the expansion of a SIMION model by

4

adding new functionality. The SIMION collision models, namely the hard sphere HS1 (see section 3.5.1) and the SDS (statistical diffusion simulation, see section 3.5.2) models, are provided as user programs as well. A set of default simulation results can be exported as delimited text files via the SIMION interface; other more specific results can be exported via custom user programs.

2.4. Data Processing

Most of the results presented in this work are processed with custom Python 3 [14] scripts or modules. The core of each script is comprised of the following python libraries: NumPy [15] and Pandas [16, 17] for data handling, SciPy [18] for data processing, e.g., triangulation, and Matplotlib [19] for data visualization and plotting. For some visualizations of flow and pressure profiles ParaView [8] (or paraFOAM) is used. Functions or packages which are used for special tasks are mentioned in the corresponding section.

3. Theory

This chapter briefly introduces the two numerical approaches behind the SPARTA and OpenFOAM frameworks presented in the previous chapter. The description begins with the Direct Simulation Monte Carlo approach followed by the continuum model, which OpenFOAM is based on. The Knudsen number is then used to describe the pressure regimes in which these two models are applied. Furthermore, the collision models and the evaporation model used for simulations are introduced.

3.1. Direct Simulation Monte Carlo

Graeme Brid first proposed the Direct Monte Carlo Simulation (DSMC) approach [2, 20]. The DSMC technique provides a probabilistic physical simulation of gas flows by tracking the movement of representative model particles in a physical space. One prerequisite is a dilute gas in which the mean free path is much larger than the particle diameter. This ensures that in combination with the probabilistic approach and a time step size smaller than the mean collision time, the particle motion is uncoupled from the collisions. This enables the possibility to use real particle diameters, but leads to the requirement of a computational mesh. This mesh overlays the total simulation domain, which includes possible geometric structures and is divided into "computational cells". Additionally, the number of real particles is represented by a smaller number of simulated particles. The ratio between simulated and real particles is called the F_{num} parameter [21]. A key concept of this method is that one simulated particle represents a large number of identical real molecules, rather than a distribution of different real molecules [22]. The DSMC method in its most simple form provides a solution of the Boltzmann equation, for time and grid sizes approaching zero and particle number approaching infinity [23]. A major downside of this method is that usually a large number of real particles are represented by each simulated particle. This generally leads to generally much larger sampled fluctuations of the macroscopic gas properties in the simulation than the fluctuations in the real gas. This can be mitigated by decreasing the F_{num} parameter or by performing several statistically independent simulation runs. The latter

then decreases the fluctuations with the square root of the sample size [21]. The following description of the DSMC procedure is based on the book "The DSMC method" written by Graeme Bird [21].

3.1.1. The DSCM Algorithm

The DSMC method is based on three physical characteristics of a dilute gas: First, the particles move in a free flight without any interaction on time scales on the order of the local mean collision time. This means, that the particles can be modelled to travel on straight lines, without any loss in accuracy. Second, the impact parameters and initial orientation of colliding molecules are randomly distributed. This has the advantage that each collision does not need to be deterministically simulated. And third, only a small fraction of the real particles needs to be simulated to an obtain accurate description of the flow. However, this also has the consequence that a DSMC simulation cannot determine precisely, which real particle actually collides and what impact parameters characterize the initial conditions of each collision [22]. The DSMC algorithm can be divided into the following steps:

1. Generate new particles, if necessary.
2. Move all particles along their molecular velocity vectors for a time step less than the local mean collision time.
3. Perform collisions stochastiscally within each computational cell, assuming collision parameters to be random.
4. Sample particles properties in each cell.
5. Return to 1.

Each time step is started with the introduction of new particles based on their spawn position and the boundary conditions at that point, if necessary. Then, the key steps are performed, namely the moving procedure of the particles, the collision interaction, and the sample of macroscopic flow properties. These three steps are discussed in more detail below. In summary, the DSMC technique capitalizes on the intrinsic characteristics of dilute gases by utilizing simulated particles that stand for a great number of identical real molecules, advancing particles with time steps close to the average collision time, and randomly selecting collision pairs and initial orientations within volumes (computational cells) near the mean free path [22].

3.1.2. Particle Move Procedures

All particles within the simulation domain are moved in each time step. The simplest approach is to move particles for their full time step, followed by the determination of the their new coordinates. Therefore, the position of each particle $\vec{s}$ is updated:

$$\Delta\vec{s} = \vec{c} \cdot \Delta t \qquad (3.1)$$

With $\vec{c}$ as the molecular velocity and Δt as the time step size. Depending on the new particle position, different actions are required. If the new particle position resides outside the computational domain or within a solid body, the appropriate boundary condition must be applied. If there is no collision with a surface or the edge of the domain, the particle is directly assigned to a compute cell. This could be the same as before or a neighboring cell. After all particles are moved and sorted into cells, the remaining physical models (e.g. collisions or cell properties) are determined on the list of particles within each cell [21, 22]. It should be noted that there are other particle motion models besides this simple approach, such as particle "ray-tracing" [22, 24].

3.1.3. Collision Procedures

Collisions between simulated particles within each computational cell are performed stochastically. During each time step, the particles are randomly paired and tested for a collision. Thus, all possible combinations of pairs are sampled in each cell. Since the potential collision partners are randomly paired, the cell size must be at or below the local mean free path as too large cells would lead to unrealistic results. The probability of a collision is proportional to the product of the collision cross section σ and the relative speed c_r of the collision partners [22]. The maximum number of possible collisions $N_{\mathrm{pc,max}}$ is given as:

$$N_{\mathrm{pc,max}} = \frac{1}{2} \cdot N(N-1) \cdot \mathrm{F_{num}} \cdot (\sigma c_r)_{\mathrm{max}} \cdot \frac{\Delta t}{V_{\mathrm{cell}}} \qquad (3.2)$$

with N as the number of particles in the compute cell, Δt as the time step size, and V_{cell} as the volume of the collision cell. Equation (3.2) requires the determination of the collision cross section σ, which is dependent on the collision model used [21]. The maximum product of the collision cross section and the relative speed $(\sigma c_r)_{\mathrm{max}}$ is an estimate of the maximum expected values within each cell. As the maximum number of possible collisions $N_{\mathrm{pc,max}}$ is known, the number of particle pairs to be tested N_{pairs} is limited as:

$$1 \le N_{\text{pairs}} \le \frac{N}{2} \tag{3.3}$$

The collision rate is then simulated by randomly selecting N_{pairs} particle pairs and calculate a collision probability P_{coll} :

$$P_{\text{coll}} = \frac{N_{\text{pc,max}}}{N_{\text{pairs}}} \cdot \frac{\sigma c_r}{(\sigma c_r)_{\text{max}}} \tag{3.4}$$

This probability is further processed by the acceptance-rejection procedure, which compares a calculated normalized probability with a randomly created value. If this normalized probability is greater than the random fraction the action or value is accepted, if not it is rejected [20–22].

3.1.4. Sampling of Flow Properties

To determine the macroscopic flow properties, the particle properties are sampled at regular time intervals. The sample size has naturally an impact on the statistical fluctuation of the determined value. The properties of the particles are determined, as given per simulated particle, which consists of a species p. Typical parameters are, for example: The total particle number $\sum N_{\text{p}}$, the weighted particle number $\sum N_{\text{p}}^{''}$, the velocity components $\sum u_{\text{p}}^{''} \sum v_{\text{p}}^{''} \sum w_{\text{p}}^{''}$, and the rotational energy $\sum \epsilon_{\text{rot,p}}^{'}$. With these particle properties the flow properties can be calculated [21]. As an example, the physical particle number density n and the overall gas density ρ can be calculated as follows:

$$n = \text{F}_{\text{num}} \frac{\sum_{\text{p}=1}^{q} (\sum N_{\text{p}}^{''})}{N_{\text{samp}} V_{\text{cell}}} \tag{3.5}$$

$$\rho = n \frac{\sum_{\text{p}=1}^{q} (m_p \sum N_{\text{p}}^{''})}{\sum_{\text{p}=1}^{q} (m_{\text{p}} (\sum N_{\text{p}}^{''}))} \tag{3.6}$$

With m_p as the mass of the particle species p and N_{samp} as the total number of samplings over which the summations are performed. There are more properties that can be obtained with this procedure. For a more comprehensive list, see [21].

3.1.5. Sampling of Surface Properties

Surface properties are determined during the particle move time, whenever a particle strikes a solid surface. The process is the same as for the sampling of the flow properties. There are some quantities that are sampled for each surface element, as for example

the number of simulated particles which interact with the given surface $\sum(N_\mathrm{p})$. These sample properties are recorded within a specific temporal duration Δt_samp. An example of a calculable flow property is the total number flux $\dot{N}_\mathrm{p}$ to a surface element with a surface area S_el:

$$\dot{N}_\mathrm{p} = \frac{\sum_{\mathrm{p}=1}^{q}(\sum(N_\mathrm{p}))\mathrm{F_{num}}}{S_\mathrm{el}\Delta t_\mathrm{samp}} \tag{3.7}$$

Other determinable variables are the pressure, shear stress, velocity and temperature slip, force and momentum [21].

3.2. Continuum Model

Continuum models approach branches of mechanics that deal with forces acting on a continuous mass rather than on discrete particles. They ignore the fact that matter is made of atoms, but deliver a sufficiently accurate description as long as the considered length scales are much greater than the interatomic distances. The sum of externally applied forces can be used to describe the flow of a fluid. These forces can be classified into two categories: body and surface forces. Body forces include centrifugal and electromagnetic forces. On the contrary, pressure, viscosity, and gravity are surface forces. To describe fluid motion, the most relevant properties of a simple fluid are density and viscosity. Other properties such as specific heat, become important only under certain conditions, such as large temperature differences [25, 26]. The following description of the continuum model is based on the book "Computational methods for fluid dynamics" written by J.H. Ferziger et. al. [25].

3.2.1. Conservation Principles

Conservation laws can be derived from the consideration of a given amount of matter or control mass (CM) and its extensive properties such as mass, momentum, and energy. In general, it is more convenient to consider a flow in a defined spatial region, the control volume (CV) than to deal with a parcel of matter passing through the region of interest. This method of fluid analysis is called the control volume approach. It starts with two extensive properties for a fluid, the mass and the momentum. For mass, which is neither created or destroyed, the conservation equation can be expressed as:

$$\frac{dm}{dt} = 0 \tag{3.8}$$

Here m is the mass and t the time. Additionally, the momentum can be changed by the action of forces. This is described by Newton's second law of motion:

$$\frac{d(m\vec{u})}{dt} = \sum \vec{f} \qquad (3.9)$$

with $\vec{u}$ as the velocity and $\vec{f}$ for the forces acting on the fluid mass. These laws with their extensive properties are translated into the CV approach: The fundamental properties are intensive rather than extensive, such as density ρ (mass per unit volume) and velocity $\vec{u}$ (momentum per unit mass). The former are properties that are independent of the amount of matter [25].

Let ϕ be any conserved intensive property (e.g. for momentum $\phi = \vec{u}$), the corresponding extensive property Φ can be written as:

$$\Phi = \int_{V_{\text{CM}}} \rho\phi dV \qquad (3.10)$$

with V_{CM} as the volume occupied by the control mass. This leads to Reynold's transport theorem, which is used to recast time derivatives of integrated quantities:

$$\frac{d}{dt}\int_{V_{\text{CM}}} \rho\phi dV = \frac{d}{dt}\int_{V_{\text{CV}}} \rho\phi dV + \int_{S_{\text{CV}}} \rho\phi(\vec{u} - \vec{u}_{\text{s}}) \cdot \vec{n} dS \qquad (3.11)$$

where V_{CV} is the CV volume, S_{CV} is the surface surrounding the CV, $\vec{n}$ is the unit vector orthogonal to S_{CV} and directed outward, $\vec{u}$ is the fluid velocity and $\vec{u}_{\text{s}}$ is the velocity with which the CV surface is moving, normally equal to zero. This equation states that the rate of change of the amount of the property in the control mass is equal to the rate of change of the given property within the control volume plus its net flux of through the CV boundary due to fluid motion, relative to the CV boundary. The last term is the convection term [25].

3.2.2. Mass Conservation

The mass conservation follows directly from Raynold's theorem (see eq. (3.11)), by setting $\phi = 1$:

$$\frac{\partial}{\partial t}\int_{V} \rho dV + \int_{S} \rho\vec{u} \cdot \vec{n} dS = 0 \qquad (3.12)$$

By applying Gauss' divergence theorem to the convection term, the surface integral is transformed to a volume integral. In addition, integration leads to a differential coordinate-free form:

$$\frac{\partial \rho}{\partial t} + \nabla(\rho\vec{u}) = 0 \qquad (3.13)$$

Equation (3.13) can be expressed in Cartesian coordinates as followed:

$$\frac{\partial \rho}{\partial t} + \frac{\partial \rho u_i}{\partial x_i} = 0 \qquad (3.14)$$

where x_i ($i = 1, 2, 3$) or (x, y, z) are the Cartesian coordinates and u_i or (u, v, w) are the Cartesian components of the velocity vector $\vec{u}$ [25].

3.2.3. Momentum Conservation

There are numerous forms of the momentum equations; mathematically they are equivalent, but from a numerical point of view, some are more difficult to deal with. Again, Raynold's theorem (see eq. (3.11)) and Newton's second law of motion (see eq. (3.9)) are used and ϕ is replaced by $\vec{u}$:

$$\frac{\partial}{\partial t}\int_V \rho\vec{u}\,dV + \int_S \rho\vec{u}\vec{u}\cdot\vec{n}\,dS = \sum \vec{f} \qquad (3.15)$$

In order to express the right-hand side of eq. (3.15) in terms of intensive properties, one has to take into account the forces that may be acting on the fluid in a control volume: surface and body forces. To eliminate the possibility that the surface forces cannot be expressed by density and velocity, it is assumed that the fluid is Newtonian. A Newtonian fluid is characterized as a fluid that follows Newton's law of viscosity, i.e., the viscosity is not coupled to the stress experienced by the fluid [27, 28]. Fortunately, the Newtonian model applies to many actual fluids. For non-Newtonian fluids, the relation is more complicated and beyond the scope of this work, but can be found in the literature [29]. The molecular rate of momentum transport for Newtonian fluids is the stress tensor T. This leads, analogously to the mass conversation, to the following equation:

$$\frac{\partial \rho\vec{u}}{\partial t} + \nabla(\rho\vec{u}\vec{u}) = \nabla T + \rho\vec{b} \qquad (3.16)$$

where b are the body forces (per unit mass). Body forces are forces originating from a source outside of the considered body, which act on the volume respectively the mass of a

body, for example the gravitational force [30]. The corresponding equation in Cartesian components is

$$\rho \frac{Du}{Dt} = \frac{\partial \rho u_\mathrm{i}}{\partial t} + \nabla(\rho u_\mathrm{i} u) = \nabla t_\mathrm{i} + \rho b_\mathrm{i} \tag{3.17}$$

where t_i and b_i are the ith components of the stress tensor, respectively, the body force. The eq. (3.17) is the so-called Navier-Stokes equation. Normally, gravity is the only body force considered [25].

3.2.4. Conversation of Scalar Quantities

The starting point for the description of other scalar quantities ϕ is an analogous equation to eq. (3.11):

$$\frac{\partial}{\partial t} \int_V \rho \phi \, dV + \int_S \rho \phi \vec{u} \vec{n} \, dS = \sum f_\phi \tag{3.18}$$

where f_ϕ represents the transport of ϕ by mechanisms other than convection and any sources nor sinks of the scalar quantity. For example, diffusion transport, which is usually described by a gradient approximation, as for example Fourier's law for heat diffusion or Fick's law for mass diffusion, which is given by

$$f_\phi^d = \int_S \Gamma \nabla \phi \cdot \vec{n} \, dS \tag{3.19}$$

where Γ is the diffusivity for the quantity ϕ. The coordinate-free vector form of eq. (3.18) and eq. (3.19) is:

$$\frac{\partial(\rho \phi)}{\partial t} + \nabla \cdot (\rho \phi \vec{u}) = \nabla \cdot (\Gamma \nabla \phi) + q_\phi \tag{3.20}$$

where q_ϕ is the source or sink of ϕ, or the so-called source term. The corresponding equation in Cartesian components is [25]:

$$\frac{\partial(\rho \phi)}{\partial t} + \nabla \cdot (\rho \phi \vec{u}) = \frac{\partial}{\partial x_\mathrm{i}} \left(\Gamma \frac{\partial \phi}{\partial x_\mathrm{i}} \right) \tag{3.21}$$

Energy Conversation

The first law of thermodynamics leads to an energy equation. It states that the rate of change in energy of a fluid is equal to the rate of heat addition to the fluid and the rate of work on the fluid:

$$\rho \frac{\partial E}{\partial t} + \rho \nabla \vec{u} = \nabla(k \nabla T) + \Phi + \vec{q}_{\mathrm{E}} \tag{3.22}$$

$$\nabla(k \nabla T) = -\vec{q} \tag{3.23}$$

where $\vec{q}$ is the heat flux vector, T the temperature, k the thermal conductivity, and Φ the dissipation function. All effects caused by viscous stresses are described with the dissipation function Φ. It is non-negative since it only contains squared terms and represents the internal energy due to the deformation work on the fluid [25, 26].

In summary, the equations governing fluid flow are more complex than they appear. They are non-linear, coupled, and difficult to solve. However, the Navier-Stokes equations are capable of accurately describing the flow of a Newtonian fluid. The first step toward a solution is simplification, for example by assuming a non-compressible fluid. But in most cases, even when simplified, these equations cannot be solved analytically. To obtain a numerical approximation, a discretization method is used. This approximates partial differential equations (PDEs) to a system of algebraic equations, which can then be solved on a computer. Overall, these approximations are applied to small domains in space and/or time. Thus, the numerical solution provides results at discrete locations in space and time [25, 31].

3.3. Discretization Methods

To solve a given partial differential equation system, a discretization method must be used. There are many approaches, the most common are: The finite difference (FD), finite volume (FV), and finite element (FE) approach. Others, such as the Lattice Boltzmann method, are used in computational fluid dynamics (CFD), but their use is limited to special classes of problems. The first step in each method is the definition of a numerical grid on which the variables are calculated. This is essentially a discrete representation of the geometric domain on which the problem is to be solved. The geometrical grid generation divides the solution domain into a finite number of subdomains. There are several ways to divide such a domain into these subdomains, depending on the spatial dimension of the domain; examples are structured (regular) grids, a block-structured grids or an unstructured grids [25] .

3.3.1. Finite Difference Method

The finite difference (FD) method is the oldest of the presented methods. It was introduced by Euler in the 18$^{\text{th}}$ century to provide numerical solutions of partial differential equations. Additionally, it is the easiest method to use for simple geometries. The starting point of this method is a differential equation ϕ. The solution domain is covered by a grid, and at each grid point, the partial differential equation is approximated by partial derivatives. To obtain these approximations to the first- and second-order derivatives of the variables with respect to the coordinates, Taylor series expansions or polynomial functions are used [31]. This leads to one algebraic equation per grid node, in which the variable value at that node and a certain number of neighbor nodes appear as unknowns:

$$A_P \phi_P + \sum_l A_l \phi_l = Q_P \tag{3.24}$$

Here P denotes the node at which the partial differential equation is approximated and the index l runs over all neighbor nodes in the grid. The coefficients A are based on the properties of the fluid and the geometric quantities. Q_P is presumed to be known and thus does not contain any unknown variable [25]. The system can be written in matrix notation as follows:

$$A\vec{\phi} = \vec{Q} \tag{3.25}$$

Where A is the matrix of the known square sparse coefficients, $\vec{Q}$ is a known vector, and $\vec{\phi}$ a vector containing the unknown values at the nodes of the grid. This potentially large system can be solved for the unknown ϕ by numerical direct or iterative solvers, such as the Jacobi iteration or the Gauss-Seidel algorithm [25, 31].

The FD method is rather simple and effective in structured meshes. The disadvantage of FD is that conservation is not enforced unless special care is taken. Conservation in this case means, that a property of the medium is conserved by moving from one computational cell to another [32]. It is also limited to simple geometries, which becomes a major disadvantage for complex flows. For simulations with complex geometries or large differences in local gradients, this represents a major limitation. In regions where the local gradients are large or where the simulation requires high local accuracy, an irregular mesh with increased spatial resolution has advantages. Using regular rectangular meshes with finite differences renders customized geometric refinement challenging. Additionally, the application of the FD method can becomes complicated when dealing with models containing discontinuities [25, 31].

3.3.2. Finite Volume Method

The finite volume (FV) method is well suited for the numerical simulation of conservation laws. As a starting point, it uses the integral form of the conservation equation,

$$\int_S \rho\phi\vec{u} \cdot \vec{n}\, dS = \int_S \Gamma\nabla\phi \cdot \vec{n}\, dS + \int_V q_\phi\, dV \qquad (3.26)$$

Let ϕ be a generic quantity of this conservation equation. The two surface integrals, indicated by S, describe convection ($\rho\phi\vec{u}\cdot\vec{n}$) and diffusion ($\Gamma\nabla\phi\cdot\vec{n}$). The volume integral, indicated by V, represents the source or sinks of the generic quantity ϕ. The simulation domain is divided into a finite number of contiguous control volumes (CVs). The governing equations are applied to each CV. A computational node, at which the variable values are to be calculated, is located at the center of each CV. This contrary to the FD method, where the CVs are the computational nodes. To obtain algebraic equations for each CV, the volume and surface integrals need to be approximated [25, 33, 34].

Since some terms of the transport equations require integration over the volume of the CV, a simple second-order approximation is used to express the surface integral as the product of the mean value of the integrand and the CV volume. The integrand is then approximated to the value at the CV center:

$$Q_p = \int_V q\, dV = \bar{q}\Delta V \approx q_p\Delta V \qquad (3.27)$$

where q_p is the value of q in the CV center. This is readily calculated, since all variables are available at the node center P; thus, no interpolation is needed [25]. For the approximation of the surface integral, the following relation is initially used. The net flux through a CV boundary is represented by the sum of integrals over all faces:

$$\int_S f\, dS = \sum_K \int_{S_k} f\, dS \qquad (3.28)$$

where f is the component of the convection ($\rho\phi\vec{u}\vec{n}$) or diffusion ($\Gamma\nabla\phi\vec{n}$) flux vector. For an exact solution, the value of the integrand f needs to be known at every point on the surface S_k. However, only the values of ϕ are known in the center of the CV. To solve this problem, two approximations are made: First, the integral is approximated in terms of the variable values at one or more locations on the cell face. Second, the cell face values are approximated in terms of the CV center value: then the midpoint rule can be applied: It states that the integral is approximated as a product of the integrand at the cell-face center and the cell-face area:

$$F_k = \int_{S_k} f \, dS = \bar{f}_k S_k \approx f_k S_k \tag{3.29}$$

Then the approximate value of f is provided on the face k. The sum over all k faces, added to equation 3.28 provides the approximation of the surface integral. In total, the number of equations and therefore unknowns is proportional to the number of CVs, which results in a well-determined system. The form of the algebraic equation for a particular CV is the same as eq. (3.24) and the matrix form of the entire simulation domain is given by eq. (3.25). The matrix structure is similar to the FD approach for a structured grid but more complex for other geometries. The finite volume method can be used with any type of grid and is suitable for more complex geometries [25]. The method is particularly appealing when dealing with problems in which the flux is a key factor, such as in fluid mechanics, due to its local conservation of the numerical fluxes. This means that the numerical flux is conserved from one discretization cell to the next [33].

3.3.3. Finite Element Method

The finite element (FE) method is largely similar to the FV method. The simulation domain is divided into a set of discrete volumes or finite elements that are generally unstructured. The distinguishing feature of the FE method is that the equations are multiplied by a weighting function before they are integrated over the entire domain. The result is a set of nonlinear algebraic equations. An important advantage of the FE-method is the ability to deal with arbitrary geometries and that grids are easily refined; each element is simply subdivided into smaller sub-cells [35, 36].

3.4. Transition from the Continuum to the DSMC Approach

Particle based simulations as the DSMC approach generally becomes prohibitively expensive, when the gas density is high and the flow physics transitions into the continuum regime. In contrast, the continuum model and the Navier-Stokes equations are relatively computationally inexpensive; unfortunately they break down in regions where the flow is rarefied. An evaluation of the applicability of the continuum model is typically based on the Knudsen number, which is the ratio of the mean free path λ (which is a function of fluid density ρ and temperature T) to a length scale D. The mean free path is given by the following equation:

$$\lambda = \frac{k_B T}{\sqrt{2}\pi d^2 p} \tag{3.30}$$

Here k_B is the Boltzmann constant, p is the gas pressure, and d the diameter of the particle. The Knudsen number is:

$$\text{Kn} = \frac{\lambda}{D} \tag{3.31}$$

For the length parameter D, a characteristic length of the model is used. It is commonly assumed that around the Knudsen numbers of Kn = 0.01, the continuum approach becomes invalid [37]. On the opposite side, a Knudsen number Kn $\geq$ 10 is considered as a free-molecular flow. A rarefied gas can not be considered as a continuous medium, nor a free-molecular flow, it represents a transition state. The Knudsen number range of this transition region is between 0.01 and 10. In this region, a further classification is common: The regime between 0.01 < Kn < 0.1 is called "slip flow" and "transition flow" between 0.1 < Kn < 10. It should be noted that this classification is based on empirical results, and thus it has no clearly defined boundaries. The exact boundary generally depends on the geometry considered [38]. In summary, the continuum approach is applicable as long as the continuum requirements are satisfied and particle based methods like DSMC are used for rarefied flows.

3.5. Collision Models

Generally, collision models are useful for the simulative description of non-vacuum systems, in which particles collide and are deflected randomly in such collisions. An example for such a situation is the motion of ions in a comparably dense background gas, in which ions and background particles interact significantly. A wide range of different models for the particle-particle interaction is available. These differ not only in their complexity but also in their scope of application. Some models, as the hard sphere collision model are numerically too expensive to be deployed in simulations with larger background pressures. In the following, the models used in this work are described in detail. The hard sphere collision and the statistical diffusion model are used in the SIMION program. The variable soft sphere model is used within the SPARTA framework.

3.5.1. Hard Sphere Collision Model

The hard sphere collision model is based on the kinetic gas theory. Here, individual collisions between the particles, mostly ions and background gas particles, are modeled. The expected frequency of these collisions is predicted by the kinetic gas theory. It depends on the pressure, temperature, and collision cross section [39]. In each simulation time step, the probability of a collision is determined. Whether the collision happens is decided in a Monte-Carlo approach by comparing the calculated probability with a random number. If a collision occurs, the ions are deflected randomly. In this process, the particles are treated as hard spheres [40]. The following assumptions apply to this model: Energy transfer between particles occurs solely via elastic collisions. The background gas particles are neutral in charge and their velocity follows the Maxwell-Boltzmann distribution, only depending on the local temperature. Furthermore, the bulk background gas is not affected by collisions between ions and background gas particles at all, but kinetic cooling and heating effects for the ions are taken into account. The model is most suitable for low pressure conditions and low densities of ions in comparison to the bulk gas. The simulation effort is increasing with increasing pressure, because every collision needs to calculated individually and the collision frequency is increasing with the pressure. Under elevated pressure conditions the models become numerically too expensive and other models are more suitable. In the case of SIMION the implementation of the hard sphere model is called HS1. The background gas pressure and velocity is provided uniformly, by analytical equations or as numerical fields for spatially resolved input parameters [12].

3.5.2. Statistical Diffusion Model

The statistical diffusion simulation (SDS) algorithm is an approach of describing the motion of ions under atmospheric pressure conditions in electrostatic and/or magnetic fields [39]. Although the hard-sphere model remains, its validity under elevated pressure conditions it is numerically far too expensive as there are approximately two million collisions per millimeter tarvel path. Therefore, the ions' motion is split into two fractions: The movement caused by diffusion and viscous effects. The diffusion part starts with obtaining the thermal speed and the mean free path by using the basic hard sphere kinetic gas theory. The values are used to predict the number of expected collisions in the current time step. On the basis of existing pre-calculated statistical data, a random number is used to obtain a standardized ion jump radius. Further information on

the statistical data provided are found in the SIMION supplementary documentation [39]. The jump radius is then scaled by the mean free path of the ions and a scaling factor. The result equals the length of the ion-shift vector. Finally, the ion is moved in a random direction with this shifting vector from its current spatial location [41]. The second part is the movement caused by viscous effects. In this segment of the algorithm, Stokes law is used to estimate local ion mobility and any background gas movement. A total acceleration for the ion is estimated, which is adjusted by a damping constant, which is inversely proportional to the mass and mobility of the ions [39, 41]. As input parameters for this model, in addition to all local parameters for the background gas (e.g., pressure, temperature, and velocities), the reduced ion mobility K_0 and the ion radius is required. If one of the last two values is not available, it is estimated by the SDS code itself. However, it is preferred to use an exact specification [12].

3.5.3. Variable Soft Sphere Model

The variable soft sphere (VSS) model introduces a softness parameter of the colliding spheres, as well as an adjustment of the radii of the colliding particles with the collision energy, compared to the classical hard sphere approach. With these adjustments, the VSS model enables more accurate calculations of ion trajectories, especially under higher kinetic energy conditions. The VSS model, besides the variable hard sphere (VHS) model, is based on the previously mentioned hard sphere model. First, the effective collision diameter is based on the kinetic energy of the collision, which means with higher kinetic energies the particle radii and thus the collision cross section become smaller. This leads to a decrease of the collision probability in higher kinetic environments. Second, a scattering parameter is additionally introduced to the model, which describes the softness of the colliding spheres. With increasing softness parameter, the distance between the spheres within a collision becomes smaller and the deflection angle is reduced. This leads to a narrower scattering distribution and less pronounced trajectory changes, as compared to the HS model. By setting the softness parameter to 1, the VSS model becomes the VHS model [6].

3.6. Evaporation Model

Later in this work, the description of charged droplets for simulation purposes is investigated. Therefore, a description of the process of solvent evaporation from those droplets is needed. The model is based of the work form E.J. Davis [42] and J.N. Smith et. al.

[43]. The model describes a one-component droplet, which is evaporating in a gaseous medium in the continuum flow regime, which means that the Knudsen number must be small ($Kn \ll 1$). In other words, the mean free path λ of the vapor must be small compared to the droplet radius. The temperature of the droplet surface must be close to the bulk gas temperature and not approach the boiling point of the droplet species. This ensures that the vapor pressure remains sufficiently low. The vapor needs to be removed from the droplet surface during the evaporation process and/or the chamber volume must be sufficiently large. Lastly, the assumptions of the ideal gas law are applied. The evaporation is described by the following equation:

$$D_{\mathrm{p}}^2 = D_{\mathrm{p},0}^2 - \frac{2 D_{\mathrm{AB}} M_A p_{\mathrm{A}}^0 (T_\infty)}{\rho_{\mathrm{a}} R T_\infty} \cdot t \tag{3.32}$$

Here D_p is the droplet diameter, $D_{\mathrm{p},0}$ the droplet diameter at the $t = 0$, t the time, D_{AB} the binary diffusivity of vapor A in gas B, M_A the molecular weight of the vapor A, $p_{\mathrm{A}}^0 (T_\infty)$ the vapor pressure at the surface droplet temperature, T_∞ the bulk gas temperature, ρ_{a} the density, and R the ideal gas constant. Thus, there is a linear function between the squared droplet diameter D_p^2 and the time t. The binary diffusivity is given by the following equation:

$$D_{\mathrm{AB}} = \frac{3}{8} \cdot \left(\frac{N}{\pi} \frac{M_A + M_B}{2 M_A M_B} \right)^{\frac{1}{2}} \cdot \frac{(k_B T)^{\frac{3}{2}}}{p \sigma_{\mathrm{AB}}^2 \Omega_{\mathrm{AB}}(T^*)} \tag{3.33}$$

with N as the Avogadro constant, $M_{\mathrm{A,B}}$ the molecular masses of species A or B, k_B the Boltzmann constant, T the temperature, p the pressure, and the average collision diameter σ_{AB} is given as:

$$\sigma_{\mathrm{AB}} = \frac{\sigma_A + \sigma_B}{2} \tag{3.34}$$

with $\sigma_{\mathrm{A,B}}$ as the collision diameter of species A or B. Additionally, the temperature-dependent collision integral $\Omega_{\mathrm{AB}}(T^*)$, which is a function of the reduced temperature $T^* = k_B T / \epsilon_{\mathrm{AB}}$. The molecular interaction force constant ϵ_{AB} is estimated as a result of the Lennard-Jones 6-12 molecular interaction potential:

$$\Phi_{\mathrm{AB}} = 4 \epsilon_{\mathrm{AB}} \left[\left(\frac{\sigma_{\mathrm{AB}}}{r} \right)^{12} - \left(\frac{\sigma_{\mathrm{AB}}}{r} \right)^6 \right] \tag{3.35}$$

where r is the intermolecular distance [42]. Bird, Stewart, and Lightfoot listed the values of the collision integrals, which are published by Hirschfelder et. al. in 1949 [44].

Equations (3.32) and (3.33) are transferred to a SIMION user program to allowing the simultaneous calculation of the changing droplet radius with the calculation of the ion trajectory. The user program is be found in appendix B.1. The evaporation model is integrated to the SDS collision model of SIMION. It takes, among other parameters, the mass and diameter of a particle as input parameter. These two parameters are updated during runtime with values from the evaporation model.

4. Integrated Simulation of Rarefied Gas Dynamics and Ion Transport with a DSMC Method

In this chapter, a new method for calculating drift velocities in a high-kinetic energy IMS is presented. The main feature of this method is that within one simulation run not only the ions and the background gas and their interactions are calculated simultaneously, but also all other simulation parameters, e.g., the electric field, are adjustable during runtime. This shall be performed simultaneously with the SPARTA DSMC simulation code. Not only the effect of the background gas on the ions is considered, but at the same time also the effects of the ions on the background gas. This approach allows for a more comprehensive representation of the physical system. Furthermore, this also provides the possibility of directly modeling chemical reactions at the same time. Here, for example, the resonant charge transfer is a very interesting problem to model. In this particular process, the charge of one ion species is transferred to a neutral particle of the same species. Both particles may have different kinetic energies and velocities. Thus, such a charge-transfer reaction will generally change the resulting drift velocity, and thus also the far more interesting energy distribution.

4.1. Introduction

For the determination of ion mobilities in an IMS, the DSMC code SPARTA is chosen due to the low-pressure conditions inside the modeled IMS. Only the consideration of electric fields and the Coulomb force acting on charged particles has to be added to the program. This allows the usage of all the advantages that SPARTA already provides, including the variable soft sphere collision model (VSS). In this chapter, this implementation is described and assessed. Subsequently, the ion mobility is determined using an example species and then the effects of important simulation parameters on the results are described. Eventually, other species are considered, and the calculated results are

compared with the data available in the literature.

4.1.1. Ion Mobility Spectrometry

Ion mobility spectrometry (IMS) is based on the separation of ions that drift in a gas in the presence of an electric field E. Knowledge about the formation of charged particles in ambient air has existed since the nineteenth century [45]. Later, in the early twentieth century, the motion of ions in an electric field with neutral background gas was described by Paul Langevin [46, 47]. 1970 the first commercial analytical ion mobility spectrometers were introduced by Cohen and Karasek [48]. Today, IMS has evolved into a powerful and widely used analytical method. On the one hand, IMS technology has improved to the extent that it is possible to build small hand-held and easy-to-use instruments [49, 50]. This leads to a wide field of applications, not restricted to a laboratory environment. These devices are used, for example, for airport security, chemical weapons monitoring, or air quality analysis. On the other hand, IMS is often used in combination with mass spectrometry (MS) to solve more complex analytical problems. In this case, IMS is used as a prefilter for MS systems [51]. The coupling of the two techniques has proven to be very advantageous, as in addition to the mass-to-charge (m/z) ratio of a molecular ion, the size-to-charge ratio or the electrical ion mobility, respectively, is also available from such experiments.

4.1.2. High Kinetic Energy Ion Mobility Spectrometry

The main difference between the high kinetic energy ion mobility spectrometry (HiKE-IMS) and a classical IMS is the operating pressure. While classical IMS systems operate under atmospheric pressure (AP) conditions, HiKE systems operate at reduced pressure typically between 10 mbar to 40 mbar. A HiKE-IMS is separated into two regions: In the first region, ion generation takes place, and the second is the actual drift region. The molecular dynamics in the sections of the instrument strongly depends on the reduced field strength E/N, which is the quotient of the electric field E and the number density N; expressed as Townsend (Td):

$$1\,\mathrm{Td} = 10^{-21}\mathrm{Vm}^2 \tag{4.1}$$

Due to the low pressure level in a Hike-IMS it is possible to achieve higher reduced field strengths up to 120 Td in both the reaction and drift region [52]. Therefore, the HiKE-IMS allows more insight into the chemical kinetics of e.g. cluster reactions. Higher

effective ion temperatures and shorter reaction times can be achieved due to the reduced pressure and greater reduced field strength [53]. The mean free molecular path exceeds that in an AP-IMS, which in turn enables the possibility to observe, for example, larger cluster systems. In an atmospheric pressure IMS the mean free path is much shorter, and only smaller cluster systems can be observed because of the higher number of collisions between the cluster and the background gas. Additionally, due to the kinetic energy of the ions, the ions gain much higher effective ion temperatures, although the HiKE-IMS is operated at low absolute temperatures.

4.1.3. Ion Mobility

In the following, drift velocities v_d are determined. To be able to compare them with the literature data, the mobility of the ions K is used. The ion mobility is a more fundamental property of an ion within a given drift gas system. It is expressed by the quotient of the drift velocity and the electric field strength E:

$$K = \frac{v_d}{E} = \frac{L}{t_d \cdot E} \tag{4.2}$$

Here, L is the length of the drift area in the IMS and t_d is the drift time of the ion. To take into account the different operating pressures and temperatures of different instruments, the reduced ion mobility K_0 is used:

$$K_0 = K \cdot \frac{N}{N_0} = K \cdot \frac{T_0}{T} \frac{p}{p_o} \tag{4.3}$$

N is the neutral number density, N_0 is the neutral density under standard conditions, p and p_0 are the pressure and standard pressure, and T and T_0 are the temperature and standard temperature. The number density can be expressed as the relation between pressure and temperature using the ideal gas law. According to theoretical studies [54, 55], the reduced ion mobility K_0 depends on various parameters:

$$K_0 = \frac{3\sqrt{2\pi}}{16} \frac{ze}{N_0} \sqrt{\frac{1}{k_B T_{\text{eff}}} \left[\frac{1}{m(T_{\text{eff}})} + \frac{1}{M} \right]} \cdot \frac{1}{\Omega(T_{\text{eff}})} \tag{4.4}$$

In addition to the mass of the charged particle m and the mass of the background gas M, the collision cross section Ω of the charged particle is of particular importance. Here, z is the charge state, e the elementary charge, and k_B the Boltzmann constant. The effective ion temperature T_{eff} reflects the effects of the collisions of the ion and the background particles, which depend on the reduced field strength. The average

collision energy is an important parameter for the dynamics of clustering and declustering reactions, which, however, have no major significance in this work. The present focus is on the theoretical possibility of determining the drift velocity in dependence on the collision cross section and vice versa.

4.2. Implementation of Electric Fields in SPARTA

SPARTA handles basic chemical reactions and arbitrary surface geometries in the simulation domain. However, albeit charged particles (charged droplets, molecular ions) are implemented in SPARTA, their interaction with external fields is currently not considered. The SPARTA framework is designed in such a way that it can be easily extended with additional custom functionalities. To give a brief overview, individual parts of the SPARTA framework are the *fixes*. A fix is an operation that is applied to the system during time stepping [56]. One example is the introduction of new particles to the simulation domain during runtime. The code for new fixes can be added and most simulation properties can be accessed and changed within the fix. The framework is written in C++, therefore, potential extensions must be provided in C++ as well. In this work, a new extension was developed to allow for the simultaneous determination of electric field force and the interaction between charged particles and neutral gas particles with the variable soft-sphere collision model. Therefore, a fix named `fix_efield.cpp` and a header-file named `fix_efield.h` (cf. appendix B.2) are added to the SPARTA source code. After compiling the code, the new fix is available, which initially could handles linear and time-constant electric fields.

4.2.1. Operation Principe of the Electric Field Fix

The electric field fix is designed to take four different parameters: The electric field vectors on each direction (x, y and z) and the species that is affected by the electric field. These species have to be charged particles. The program ensures that the given species is defined in the simulation setup and that the given charge is not zero. Furthermore, it is verified that each component of the electric field vector is a valid number. To be able to determine the acceleration of particles by the electric fields, the parameters such as mass m and charge q of the species are retrieved. Together with the time step length dt, the velocity form electric acceleration v can now be determined. The force F exerted by the electric field is determined by:

$$F_{\mathrm{x,y,z}} = E_{\mathrm{x,y,z}} \cdot q \tag{4.5}$$

The resulting acceleration a is then calculated.

$$a_{\mathrm{x,y,z}} = \frac{F_{\mathrm{x,y,z}}}{m} \tag{4.6}$$

Finally, the resulting velocity is expressed by the time step size and the acceleration.

$$v_{\mathrm{x,y,z}} = a_{\mathrm{x,y,z}} \cdot dt \tag{4.7}$$

This additional velocity component is added to the already calculated velocity. This step is performed at the beginning of each time step and is done for every particle of the given species in each dimension.

4.2.2. Testing the E-Field Fix

To verify that the custom source code is working as expected, a series of benchmark simulation runs are performed. One ion is introduced to the simulation domain and is accelerated by a constant electric field. A linear acceleration is expected because no background gas is considered in the simulation. A two-dimensional rectangle is used as the simulation domain.
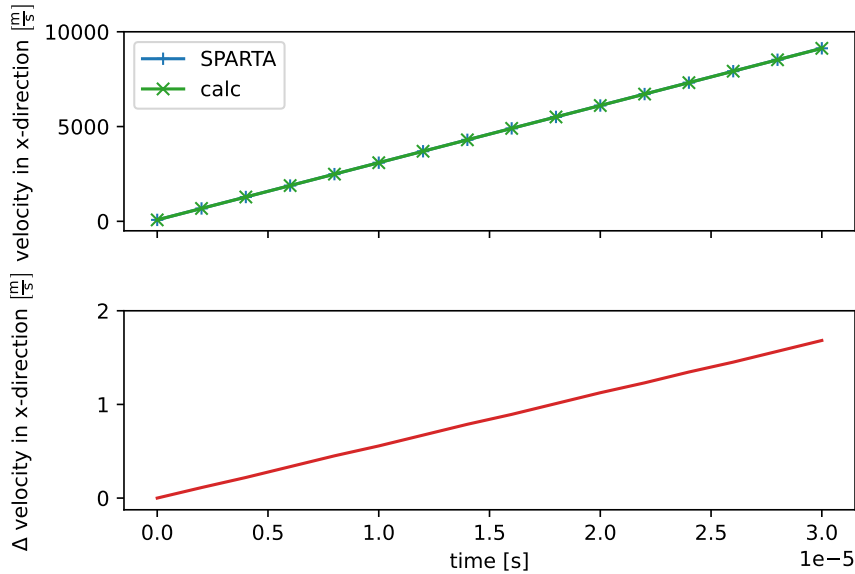
Figure 4.1.: Comparison of the achieved velocity of one particle. The blue line represents the velocity calculated with the new SPARTA fix and in green the analytically calculated velocity. On the bottom the difference between the two velocities is shown.

As shown in fig. 4.1 it is verified that both the velocity obtained by the simulation code and the analytically calculated velocities are the same. As a result, only small floating number errors are observed. It is expected from theory that an ion achieves a steady-state drift velocity after an acceleration period, when a background gas is present. The stable drift velocity obtained depends on the applied electric field strength and the background gas pressure. If the background gas pressure increases, the mean free path of the ion decreases; consequently, the collision frequency increases, and the ions are slowed down.

Table 4.1.: SPARTA simulation parameters for the e-field test case: Constant drift velocity.

Parameter	Value
Species	O_2^+ in N_2
Background gas pressure	$14.3\,\mathrm{mbar}$
n_ρ	1×10^{21}
Number of ions	approx. 100
Reduced field strength	$20\,\mathrm{Td}$

The relevant simulation parameters are listed in table 4.1. Here, n_ρ stands for the number density of the gas mixture. For three-dimensional simulations, the unit of the specified density is the number of particles per volume. For the two-dimensional case, which is present here, the unit is the effective number of particles per area, since the z-dimension thickness of the simulation box is equal to one [56].
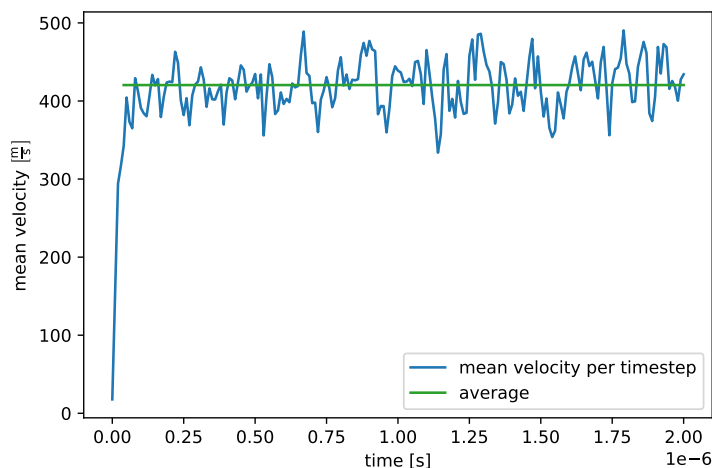
Figure 4.2.: The blue trace describes the mean velocity of all ions over the time. At the beginning a short acceleration period is apparent. After approximately 50 nanoseconds a nearly constant drift velocity is achieved, the average value is indicated by the green line.

As shown in fig. 4.2, the steady state drift velocity is reached after $50\,\mathrm{ns}$. The average drift velocity is $421\,\mathrm{m\,s^{-1}}$ with a standard deviation of around $31\,\mathrm{m\,s^{-1}}$. To obtain more

numerically stable values, the number of ions can be increased. In this case 100 ions are enough to show that a stable value is reached and the achieved value does not need to be more accurate.

4.3. Calculation of Ion Mobilities in a HiKE-IMS

To describe the quality of the determined simulated drift velocities using the extended SPARTA DSMC code, the reduced ion mobilities K_0 for different ion and background gas species pairings are calculated. Pairs of ions and background gas species are chosen on the basis of available literature data. First, the influence of some key simulation parameters, e.g., the time step size, is determined by the calculation of O_2^+ in N_2. Taking into account the results of these initial simulations, further ion mobilities for O_2^+ in CO_2 and N_2^+ in N_2 are calculated for different reduced field strengths. The detailed presentation of the simulation results is followed by an overall discussion of the results and outlook.

4.3.1. Description of the Simulation Boundary Conditions

A simplified model of a HiKE-IMS drift tube is used for all following simulations. The two-dimensional geometry consists of a drift tube with a total length 160 cm and a height of 30 cm. The electric field orientation is parallel to the x axis of the simulation domain (cf. green arrow fig. 4.3). The ions are generated in the blue area on the left. The top and bottom are simulated as walls. Particles and ions are allowed to leave the simulation domain at the right and left terminal ends. The neutral gas flow has the same orientation, in contrast to the real HiKE-IMS, as the electric field orientation. At the beginning of each simulation, the drift area is already populated with neutral gas particles according to the local pressure. All default values are valid unless explicitly mentioned otherwise. The built-in variable soft-sphere model is used as collision model [20]. The large dimension of the simulation domain is chosen to provide a sufficiently large number of neutral gas particles.

4.3.2. Description of the Numerical Evaluation

As mentioned in section 4.1.3, the reduced mobility of the ions is used to compare the simulation results with data from the literature. A small Python library named SPARA (SPARTA Result Analysis) is designed for the calculation and visualization of results.
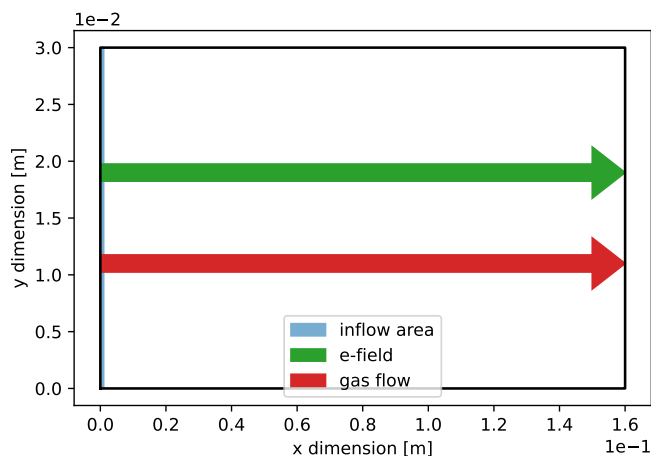
Figure 4.3.: Generic high kinetic energy IMS drift tube. The applied electric field is parallel to the x axis of the drift tube (green arrow). The neutral gas flow is orientated from left to right (red arrow). The small blue area on the left side describes the spawn area of the ions. The upper and lower domain boundaries are walls. The left and right boundaries are permeable for particles.

The reduced ion mobility is calculated as follows:

$$K_0 \left[\frac{\text{cm}^2}{\text{Vs}} \right] = 1000 \cdot \frac{v_\text{d}}{E} \frac{N}{N_0} \tag{4.8}$$

The reduced ion mobility is often expressed in $\text{cm}^2\,\text{V}^{-1}\,\text{s}^{-1}$. Here, v_d is the drift velocity, E the electric field strength , N the number density, and N_0 the number density at standard temperature and pressure. The drift velocity is calculated from the average velocity of all ions over the entire drift time. Since the effect of the ions on the neutral background gas should also be considered, the following method is developed: The SPARTA output data are transferred to VTK data [57] and for each column of the grid a vertical *plot over line* (POL) filter is applied (cf. fig. 4.4). This filter returns the values of the point-centered variables along a given line. If necessary, the filter uses interpolation to determine the values at the selected position [58]. For each POL provided dataset, the average value of this x coordinate is calculated. All values calculated in this way are then summarized in a graph. This provides the particle density as an average value for the entire drift cell depending on the x position for a given timestep. This calculation method causes the resolution to be lost in the y direction. However, because the ions

are uniformly distributed on the y axis, this dimension has no major significance.
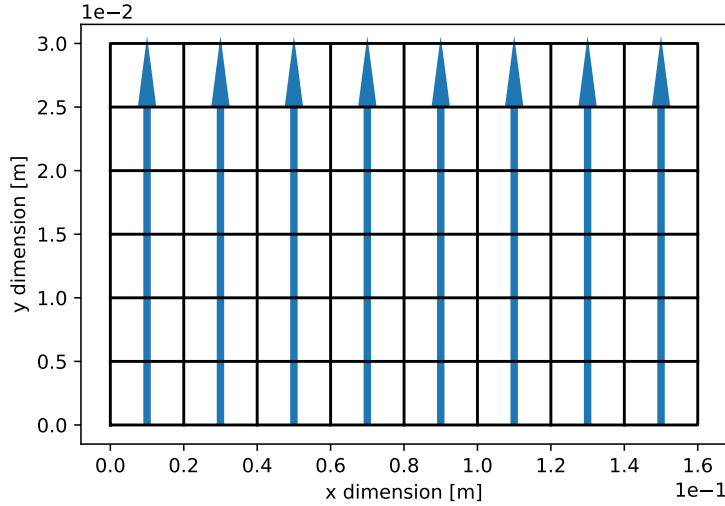
Figure 4.4.: The simulation domain is divided into grid cells (black lines). To each grid column one plot over line filter is applied (indicated as blue arrows).

Upon using the described calculation method, on the one hand, the calculated drift velocity can be converted into a comparable reduced ion mobility and, on the other hand, the influence of the ions on the background gas can be visualized and assessed.

4.4. Results

4.4.1. Variation of Simulation Parameters based on $O_2{}^+$ in N_2

The effect of different simulation parameters is investigated in the following section. Each parameter is compared with a reference simulation to determine its effect. The parameters of the reference simulation are listed in table 4.2.

The parameter F_{num} established the relation between real physical and simulation particles. For example, a value of 1×10^{21} means that one particle in the simulation represents 1×10^{21} real particles. The mean drift velocity of the ions is shown in fig. 4.5. In this case, the temporal resolution is too low for the initial equilibration phase in which the ions reach the constant drift velocity to be visible. A relatively stable drift velocity between $0\,\mu s$ to $80\,\mu s$ is established with $1330\,m\,s^{-1}$. Variations in the mean velocity are

Table 4.2.: SPARTA simulation parameters of the reference simulation run. Values printed in *cursive* are varied.

Parameter	Value
Species	$O_2{}^+$ in N_2
F_{num}	1×10^{21}
Background pressure	$14.3\,\text{mbar}$
Time step length	$2 \times 10^{-9}\,\text{s}$
Grid resolution	$3.24 \times 10^6\ \text{cells/m}^2$
Number of ions	100
Flow direction	x_{low} to x_{high}
Collision model	VSS
SPARTA version	9 Jan 2020

considered to be expected for the number of sampled ions. After this stable period the drift velocity increases to a value of $2750\,\text{m}\,\text{s}^{-1}$. For the calculation of the reduced ion mobility only the time frame with the constant velocity is selected (marked with the green line in fig. 4.5). At the end of the drift time, one expects that the overall drift velocity decreases because most of the fast ions should have left the simulation domain. However, exactly the opposite is seen, the drift velocity increases significantly.

The inhomogeneity of the background gas density is responsible for this sudden increase in velocity. As shown in fig. 4.6 the background gas density is temporally and spatially not stable. First, the area in front of the ion ensemble is considered: At 16 µs, it is observed that the background gas density is almost at the specified pressure. The density is only slightly higher. This remains stable until 88 µs. At this time, a clear decrease of the gas density in front of the ensemble is discernible. This is the reason why the drift velocity increases strongly at that time. Due to the lower background pressure, fewer collisions occur and the decelerating effect of the collisions is lost. The sharp decrease in density to the right seems to be due to the applied boundary condition: The background gas particles are allowed to leave the simulation domain at this location and the neutral gas flow is directed from left to right. Surprisingly, there is no direct increase in density on the left side of the ensemble, although new background particles enter the domain at that location. In contrast, at smaller x positions first a clear decrease is noticeable, and then an increase, which becomes more pronounced with time. It appears as if the ion ensemble is pushing the neutral gas particles together, so that they form a compression
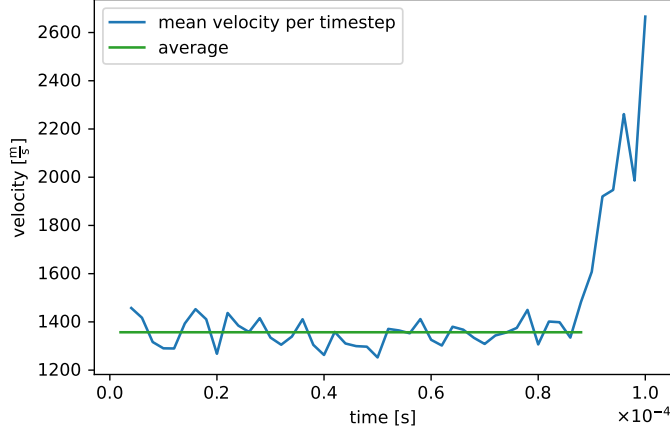
Figure 4.5.: Drift velocity results for O_2^+ ions in N_2. Simulation parameters are listed in table 4.2. The blue trace describes the mean drift velocity over all ions per timestep. The green line indicates the average value of the drift velocity, which is used for the determination of the reduced ion mobility.

wave. This leads to an area with increased density directly behind the ensemble and an area with lower density behind the area with higher density. This sinusoidal shaped wave becomes wider with increasing time; the area with higher density is never in front of the ion ensemble. However, it is noticeable that the ions pass through the drift tube with the correct density until the simulation time reaches $80\,\mu s$.

In conclusion, the value of the reduced ion mobility corresponding to a drift velocity of $1330\,\mathrm{m\,s^{-1}}$ is $5.05\,\mathrm{cm^2\,V^{-1}\,s^{-1}}$. The corresponding literature [59] value is $2.76\,\mathrm{cm^2\,V^{-1}\,s^{-1}}$, roughly a factor of two smaller. The value determined with the simulation for the reduced mobility to large and not within the expected margin of numerical and experimental uncertainty. Based on this reference reduced mobility, simulation results obtained upon variations of the input parameters are compared in the following.
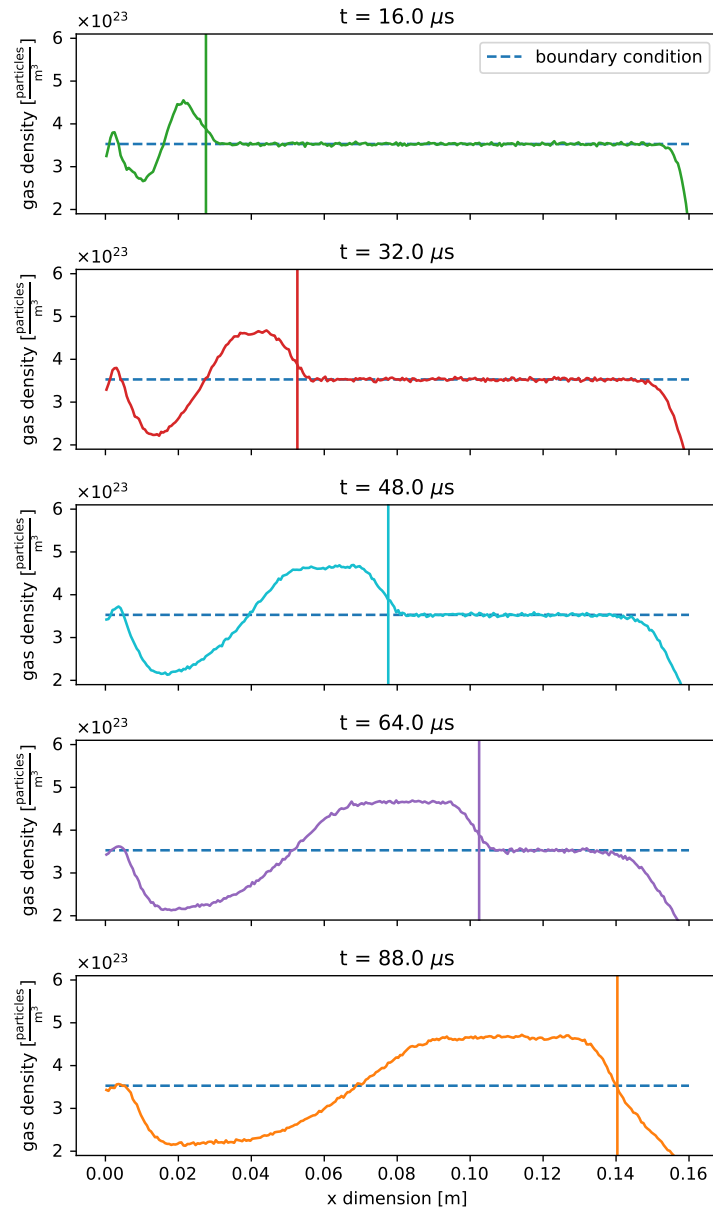
Figure 4.6.: Background gas density distribution for different times for O_2^+ in N_2. Simulation parameters are listed in table 4.2. The dashed blue line indicates the particle density according to the specified background pressure. The vertical line refers to the average x position of the ion ensemble.

Variation of the Time Step Length

As mentioned in section 3.1, the time step size Δt is a critical parameter for the DSMC algorithm. It should be small in relation to the mean collision time, and the simulated particles should move at least for one time step within each grid cell. Otherwise, no separation between the motion and collision of a particle can be made. As Eddie Yin-Kwee and Ningyu Liu describe, the time step size should be approximately equal to or less than the mean collision time for a particle [60].

$$\Delta t < \frac{\lambda}{v} \tag{4.9}$$

In other words, the time step size Δt should be smaller than the mean free path λ divided by the most probable molecular velocity v. The mean free path is given by eq. (4.10).

$$\lambda = \frac{k_{\mathrm{B}} T}{\sqrt{2} \pi d^2 p} \tag{4.10}$$

Here T is the temperature, k_{B} the Boltzmann constant, p the gas pressure, and d the diameter of the particle. Under the given conditions, the mean free path of the ions is approximately 4.41×10^{-6} m. The experimental drift velocity [53] of $742 \, \mathrm{m \, s^{-1}}$ results in a time step length that should be less than 6.0×10^{-9} s. Accordingly, the time step length of the reference simulation should already be sufficiently short. For comparison, a time step length slightly longer than the required condition and two shorter ones are investigated. The number of time steps is adjusted so that all ions reach the end of the drift cell in each simulation run.

The drift velocities are shown in fig. 4.7 and the results are listed in table 4.3. All three simulations with the time steps that satisfy the condition (eq. (4.9)) show similar profiles. Only the results of the simulation with the largest time step length looks different (cf. fig. 4.7 green line). However, the green graph shows contradictory data. On the one hand, it shows significantly lower drift speeds, but on the other hand, a short drift time, which indicates a higher speed.
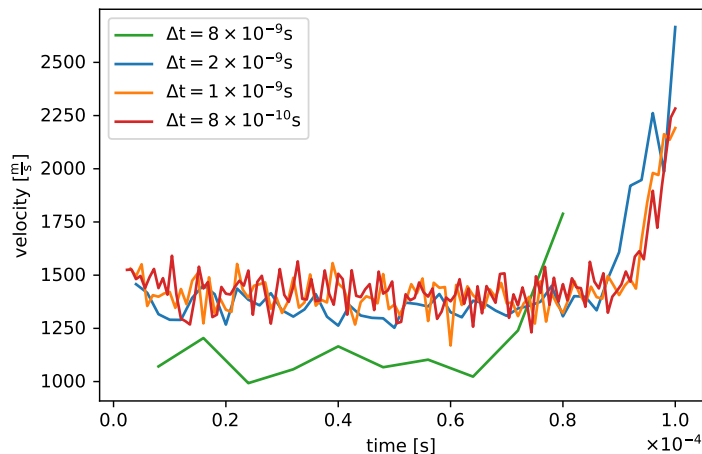
Figure 4.7.: Drift velocity results for $O_2{}^+$ ions in N_2. Simulation parameters are listed in table 4.2. Each graph represents a different time step length. The blue trace represents the reference simulation.

Therefore, the drift velocities generated by SPARTA $v_{d,s}$ (y axis values) are compared with the rudimentary calculated drift velocities:

$$v_{d,c} = \frac{L}{t_d} \tag{4.11}$$

Here L is the length, the ions passed with a stable drift speed, and t_d the time it took them to pass L.

Table 4.3.: Comparison of the results from the time step length variation.

Δt [s]	K_0 [cm^2 V^{-1} s^{-1}]	time steps/grid cell	$v_{d,c}/v_{d,s}$
8×10^{-9}	4.10	62	1.8
2×10^{-9}	5.05	205	1.2
1×10^{-9}	5.22	396	1.1
8×10^{-10}	5.29	489	1.1

The ration between these values decreases with the shorter time step length. Since the drift speed indicated by the velocity vectors as exported from SPARTA for the shortest time step length is nearly twice the drift speed calculated with eq. (4.11), the former

values are unreliable. The cause was not determined. When the advised range of the time step length is kept, this deviation appears to remain small and negligible. Another stated condition is that the particles spend at least one time step inside a grid cell. As shown in table 4.3 this condition is satisfied for all simulations. In summary, the optimum value for the reduced ion mobility is provided by the simulation run which produced an inconsistent result. The results obtained from the other simulations are slightly worse, but achieve more consistent values for the $v_{d,c}/v_{d,s}$ ratio. Consequently, no improvement can be seen compared to the data in the literature. The background gas density distribution does not show any changes to the reference simulation.

Variation of the Grid Cell Resolution

In addition to the time step length, the resolution of the grid that is used for the selection of potential collision partner for particles is another important parameter for the stability of a DSMC calculation. A general rule for the grid resolution R is that it should be one half to one third of the mean free path λ:

$$R = \frac{1}{2}\lambda \tag{4.12}$$

However, this means that the number of cells would have to increases by a factor of about 250. Accordingly, the required simulation time exceeds a reasonable time frame. The reference simulation computes around 4.2 h on 6 CPU cores, doubling the resolution with simultaneously increasing the CPU cores to 10 increases the computing time by a factor of 4. Therefore, for one simulation run, the boundary conditions are adjusted to fulfill eq. (4.12). All changes are listed in table 4.4.

Table 4.4.: Changed SPARTA simulation parameters to fulfill the stated requirement for the resolution.

Parameter	Value
Spatial scaling factor	1/100
Pressure	10 mbar
Time step length	2×10^{-10} s
Grid resolution	1×10^{11} cells/m^2

To speed up the simulation, the spatial dimensions of the IMS are scaled by a factor of 0.01. Additionally, the pressure is adjusted from 14.3 mbar to 10 mbar and the time

step length is adjusted to fit the needs of eq. (4.9). By changing these parameters the comparability between the results and the reference simulation is suffering, but necessary.
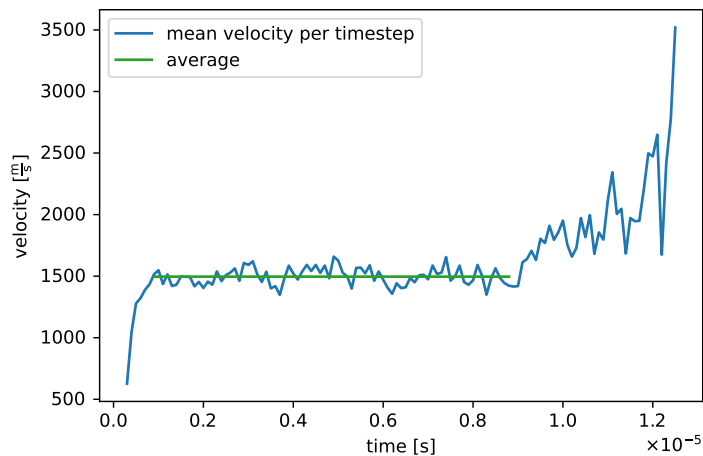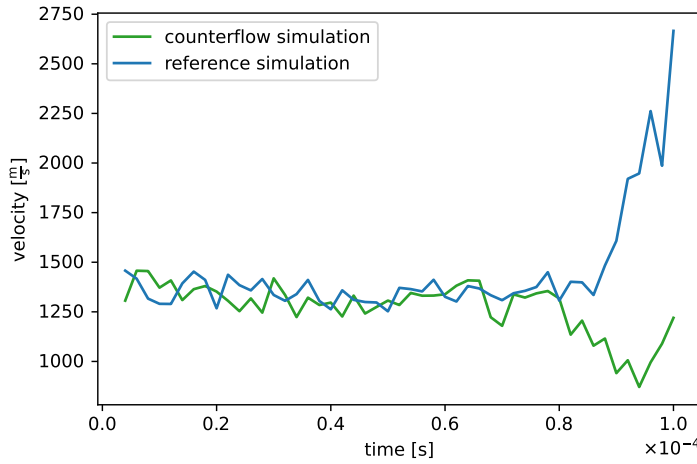

Figure 4.8.: Drift velocity results for O_2^+ ions in N_2. Simulation parameters are listed in table 4.4. The blue trace describes the mean drift velocity over all ions per timestep. The green line indicates the average drift speed, which is used for the determination of the reduced ion mobility K_0.

The pattern of the velocity profile is similar to the reference simulation as visible in fig. 4.8. An exception is that the increase of the velocity to the steady state area is visible, but this is only due to a higher sample rate of the data. Furthermore, the increase towards higher drift velocities is not as steep, but this may be caused by the overall smaller time frame in this simulation run. In this shorter time, less particles have left the domain and therefore the background pressure at the end is still a little higher as compared to the reference simulation. The average drift velocity is with $1496 \, \mathrm{m \, s^{-1}}$ slightly higher as the reference value, hence the reduced ion mobility with $5.57 \, \mathrm{cm^2 \, V^{-1} \, s^{-1}}$ as well. Thus, even a significantly enhanced grid resolution does not provide improved values in terms of ion mobility. However, the background gas density changes significantly (cf. fig. 4.9).

Now, the region in front of the ion ensemble behaves as expected. In this case, the ions have no significant influence on the background gas density in close vicinity to their position. There is still a peak on the left side of the drift tube. It is not clear whether this peak belongs to newly introduced particles or is caused by the ions; in addition it
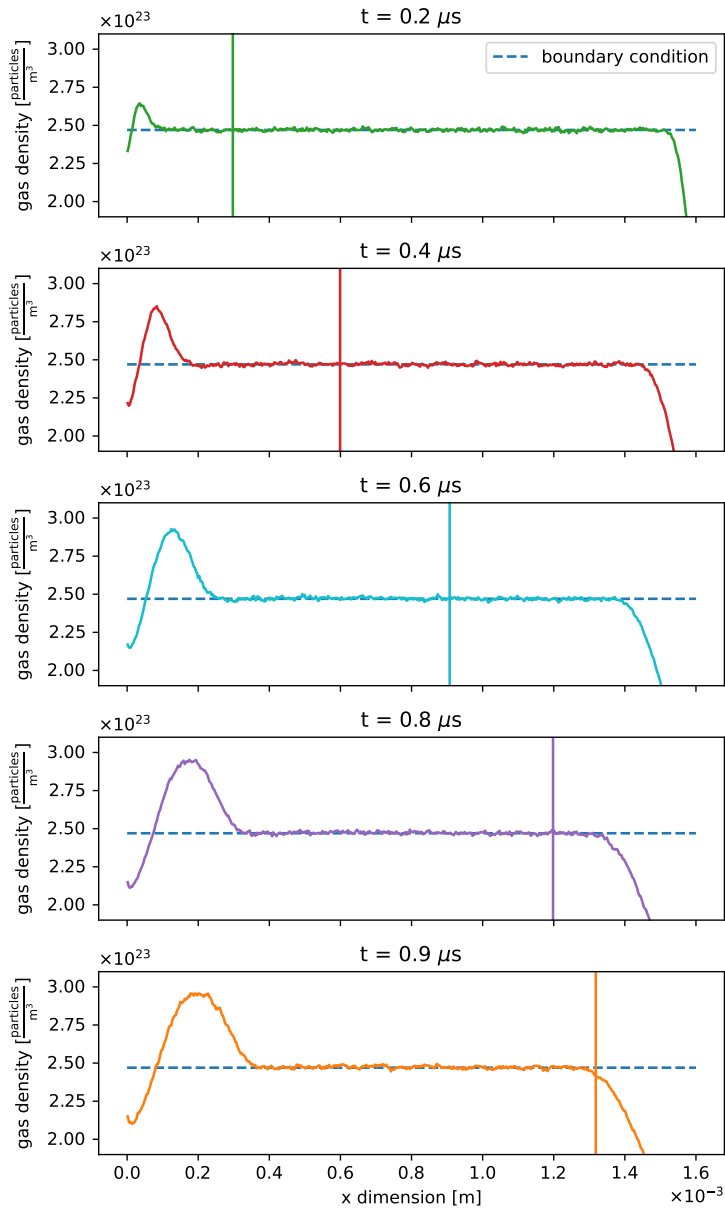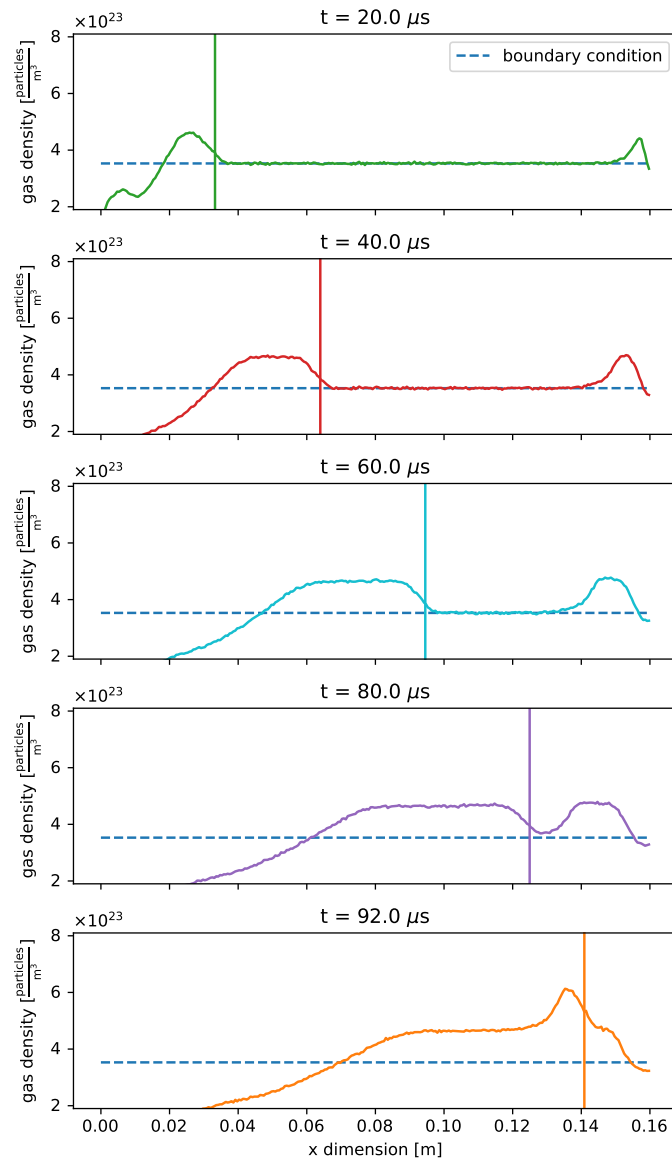
Figure 4.9.: Background gas density distribution for different times for $O_2{}^+$ ions in N_2. Simulation parameters are listed in table 4.4. The dashed blue line indicates the particle density according to the specified background pressure. The vertical line refers to the average x position of the ion ensemble.

is somehow delayed. As always, the background gas density in front of the ensemble remains stable for most of the time. The acceleration of the ions towards the end of the drift tube can also be explained by the background pressure drop.

Since it was shown that a significant increase in the grid resolution does not provide a more accurate value in terms of the ion mobility, a smaller adjustment of the resolution on the results is investigated. Here, only the resolution is adjusted in comparison to the reference simulation to ensure a better comparability. The other reference parameters remain unchanged. The resolution of the grid is improved by a factor of four and decreased to one quarter in size. The drift velocities are shown in fig. 4.10.
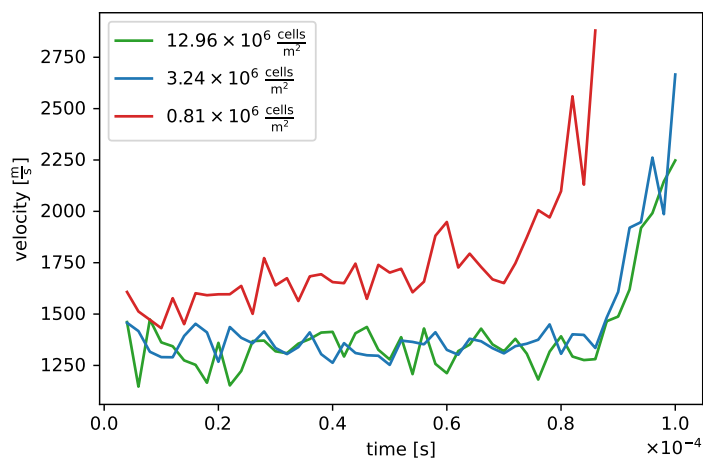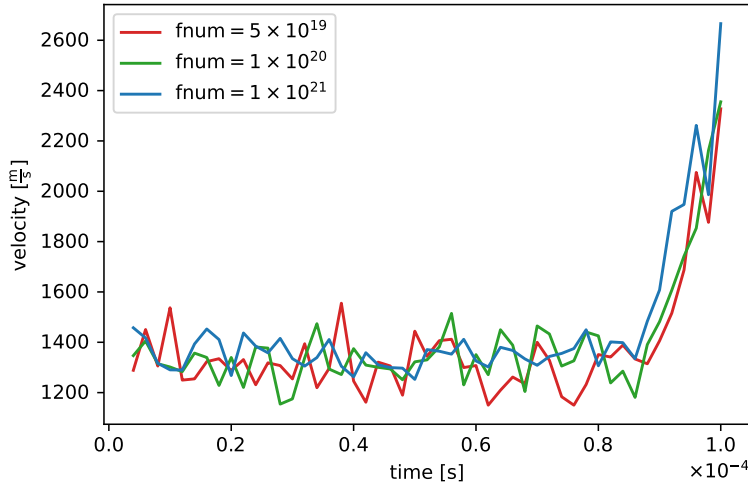

Figure 4.10.: Drift velocity results for O_2^+ ions in N_2. Simulation parameters are listed in table 4.2. Each graph represents a different grid resolution. The blue trace represents is the reference simulation.

The results show that there is no noticeable difference between the medium and higher grid resolutions, although a smaller resolution results in considerably higher drift velocities, which in turn leads to a higher reduced ion mobility of $6.09\,\mathrm{cm^2\,V^{-1}\,s^{-1}}$. The difference between the higher and the medium resolution is around $0.02\,\%$; 4.94 for the higher resolution and $5.05\,\mathrm{cm^2\,V^{-1}\,s^{-1}}$ for the standard resolution, which is well within the expected margin of numerical uncertainty. It seems that a sufficiently good grid resolution is reached with $3.24 \times 10^6\,\mathrm{cells/m^2}$. An increase in resolution only results in longer computing times.

Variation of the Flow Direction of the Background Gas

To better simulate the experimental setup, which uses a counter-flow in the drift tube, the neutral gas flow direction is changed. For all the previous studies, the neutral gas molecules are introduced on the left boundary, while the particles are introduced from the right side in the subsequent simulation.

Figure 4.11.: Drift velocity results for O_2^+ ions in N_2. Simulation parameters are listed in table 4.2. The green trace describes the simulation with the counter-flow neutral gas. The blue trace represents the reference simulation.

In contrast to the reference simulation, the velocity of the ions first decreases before it increases at the end. The region with stable drift velocity is very similar to the reference simulation. Therefore, the reversal of the background gas flow imposes no changes in the resulting ion mobility. The different behavior at the end of the drift tube is explained by the background gas density (cf. fig. 4.12).

At the end of the drift time the ion ensemble enters a region with higher density because here the new neutral gas particles are introduced. At 92 µs it can be observed that both areas with higher density merge. The ion ensemble must pass the region with elevated density at the end of the tube. Therefore, the drift speed decreases in this area, in contrast to all previous shown cases. Additionally, no elevated density at the entry of the tube is observable due to the different introduction location of the neutrals. The missing initial peak at the left terminal renders it more likely that this peak is normally

Figure 4.12.: Background gas density distribution for different times for O_2^+ ions in N_2. Simulation parameters are listed in table 4.4. The background gas flow is changed in direction. A counterflow principle is applied. The dashed blue line indicates the particle density according to the specified background pressure. The vertical line refers to the average x position of the ion ensemble.

caused by the new background gas particles and not by the passing ions. However, in the center region, the ion ensemble passes a wide area with a density according to the specified pressure of 14.3 mbar. In summary, the change of the flow direction of the neutral gas flow has no effect on the calculated ion mobility. Nevertheless, the dynamics between the neutrals and ions is clearly different in this case. If the calculated ion mobility were closer to the literature value, a closer inspection of this dynamic is recommended.

Variation of the Ratio between Physical and Simulated Particles

The ratio of physical to simulated particles (named F_{num} in SPARTA) is varied, but this only applies to the neutral gas particles and not to the number of ions. Depending on the simulation purpose, the number of simulated particles must be adjusted to obtain a statistically representative particle sample. An increase of the value of F_{num} primarily increases the calculation time, while it has less demanding additional requirements on memory. The F_{num} parameter changes from 1×10^{21} to 1×10^{20} and 5×10^{19}.

Figure 4.13.: Drift velocity results for O_2^+ ions in N_2. Simulation parameters are listed in table 4.2. Each graph represents a different F_{num} value. The blue trace represents the reference simulation.

A lower ratio between simulated and physical particles does not provide a significant improvement in terms of lower drift velocities, and the simulation results are the same

within some expected numerical fluctuations. The reduced ion mobility differs only marginally. Thus, the longer simulation times due to the lower value of F_{num} do not lead to improved results for the ion mobility.

Variation of the Number of Introduced Ions

Finally, the number of introduced ions is varied. It is noted that the reduction in the number of ions decreases the statistical certainty of the ion ensemble. The velocity profiles are independent of the number of ions (cf. fig. 4.14) as they are identical within the numerical fluctuations. As expected, an increase in numerical fluctuations is clearly visible with the decrease in the number of ions. The standard deviation of the mean velocity increases from $55\,\mathrm{m\,s^{-1}}$ for 104 ions to $410\,\mathrm{m\,s^{-1}}$ for only two ions. The best value obtained for the reduced ion mobility is $4.99\,\mathrm{cm^2\,V^{-1}\,s^{-1}}$ for 58 ions. The calculated mobility for 2 and 12 ions is $5.14\,\mathrm{cm^2\,V^{-1}\,s^{-1}}$. Overall, there is no noticeable improvement regarding the ion mobility.
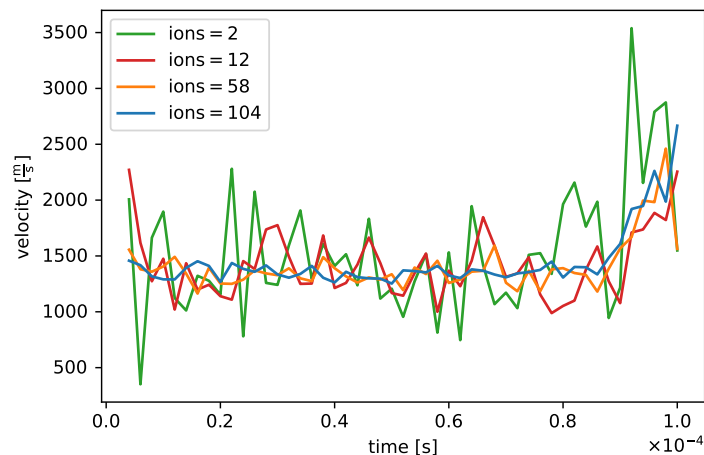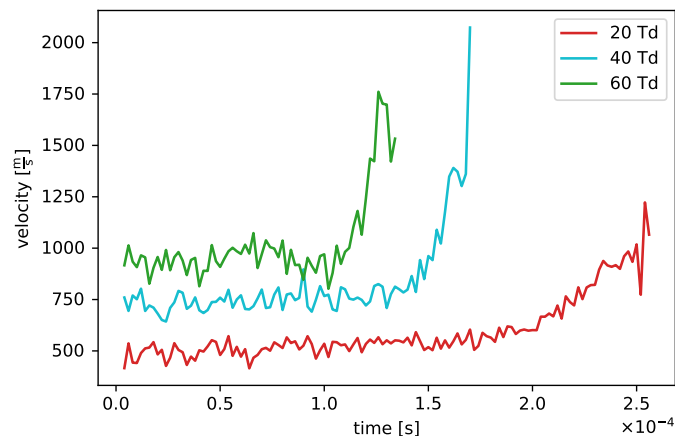

Figure 4.14.: Drift velocity results for $O_2{}^+$ ions in N_2. Simulation parameters are listed in table 4.2. Each graph represents a different number of ions. The blue trace represents the reference simulation.

In contrast to the background gas density variation data, figure 4.15 shows always the same drift time of $80\,\mathrm{\mu s}$. In this case, the number of introduced ions is varied. It is seen that it has a clear impact on the background gas density distribution. Although
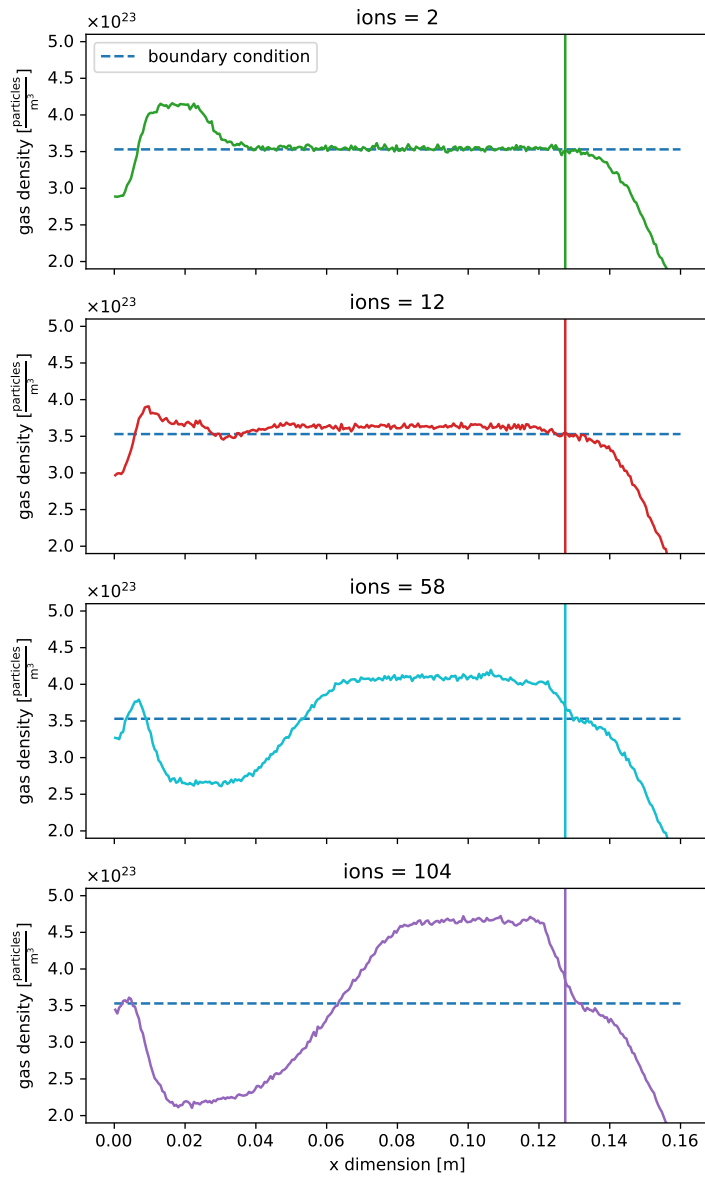
Figure 4.15.: Background gas density distribution for different number of introduced O_2^+ ions in N_2. The drift time for each frame is $80\,\mu s$. Simulation parameters are listed in table 4.4. The dashed blue line indicates the particle density according to the specified background pressure. The vertical line refers to the average x position of the ion ensemble.

there is no discernible effect on the background gas density with 2 ions, it increases as the number of ions increases. The decrease of the background gas density as well as the increase form the left side at the end of the drift tube is not affected by the number of ions. This shows that the unstable boundary conditions on the left and right sides of the drift tube do not depend on the number of ions introduced. However, this is the second time, where no direct impact from the ion ensemble to the background gas density is observed. The first time was with significantly higher grid resolution (cf. section 4.4.1). In the previous case, even with 100 introduced ions, no higher density directly after the ion ensemble is observed. Now, the latter is only the case for 2 ions. This suggests that not only the grid resolution but also the number of ions is responsible for this compression effect.

Summary of the Variation of Key Parameters

With respect to the reference simulation, it has become apparent that the determined values for the ion mobility are within the correct order of magnitude but still deviate significantly from the experimental values. As demonstrated, the ions mostly behave as expected, reaching a stable velocity after a short acceleration period. However, this is clearly too high. It was also shown that the background gas conditions towards both ends of the drift tube are not stable, but this only affects, if at all, a rather small part of the actual drift path. The effect of the ions on the background gas through which they passed is rather ambiguous. It appears as if a combined effect of the grid cell resolution and the ions themselves is responsible for this effect. If the grid resolution is significantly increased, this effect is completely absent. Additionally, the effect is not observed when the number of ions is really small. However, no significant improvement in terms of ion mobility could be achieved by any variation of the parameters. For this reason, all default values of the varied parameters (cf. table 4.2) are used for all subsequent simulations.

4.4.2. Reduced Field Strength Variation

Using two combinations of ions and background gas, the effect of different reduced field strengths is investigated. The choice of ion-background gas pairs is limited by the availability of parameters for the VSS model as well as the literature data for the different reduced field strengths. For N_2^+ in N_2, the reduced field strengths from 20 to 60 Td are investigated. For O_2^+ in CO_2 higher field strengths from 100 to 600 Td are covered. The default parameters are listed in table 4.5.

Table 4.5.: Default SPARTA simulation parameters for the reduced field strengths variation.

Parameter	Value
F_{num}	1×10^{21}
Background pressure	20 mbar
Time step length	2×10^{-9} s
Grid resolution	3.24×10^6 cells/m^2
Number of ions	100
Flow direction	x_{low} to x_{high}
Collision model	VSS
SPARTA version	9 Jan 2020

N$_2^+$ in N$_2$

A total of three different reduced field strengths are simulated: 20, 40, and 60 Td. Naturally, the drift velocity of N$_2^+$ increases with increasing reduced field strength.

Figure 4.16.: Drift velocities results for N$_2^+$ ions in N$_2$. Simulation parameters are listed in table 4.5. Each graph represents a different reduced field strength.

The shapes of the velocity profiles show no significant differences from the previous simulations. Again, a large range of constant velocities, which increases significantly towards the end. Also, the background gas density does not show differences from those already seen in section 4.4.1. The results of the corresponding reduced ion mobilities are listed below.

Table 4.6.: Comparison of the calculated and experimental [59] reduced ion mobilities for N$_2^+$ in N$_2$

E/N [Td]	$K_{0,\text{lit}}$ [cm^2 V^{-1} s^{-1}]	$K_{0,\text{sim}}$ [cm^2 V^{-1} s^{-1}]	ΔK_0
20	1.83	10.08	8.25
40	1.75	7.26	5.51
60	1.63	5.94	4.31

The largest differences are obtained for 20 Td. The drift velocity is 5.5 times higher than the experimentally determined value. The deviation between the calculated and

experimental values decreases with increasing reduced field strength: from 8.25 to 5.51 to $4.31 \, \mathrm{cm^2 \, V^{-1} \, s^{-1}}$, respectively. However, at 60 Td there is still a factor of 3.6 between the experimental and simulated values.

$O_2{}^+$ in CO_2

Due to a larger body of available experimental data, a total of four different reduced field strengths are simulated: 100, 200, 400 and 600 Td. Velocity profiles are shown in fig. 4.17.
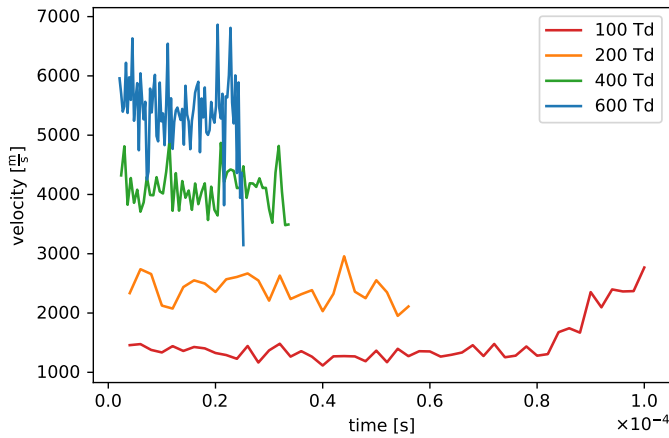
Figure 4.17.: Drift velocities results for $O_2{}^+$ ions in CO_2. Simulation parameters are listed in table 4.5. Each graph represents a different reduced field strength.

The velocity profile above 100 Td does not show an increase in the drift speed at the end of the tube, as the ions traverse the drift tube too quickly, so that no pressure drop could form at the end. At 400 Td, the velocity drops at the end. This is probably because at the last recorded data point only the slow ions from the distribution are still present, and thus the intersection velocity is lower. At 400 and even more so at 600 Td, way more data points are present, resulting in a more noisy picture. The density profile does not show any clear differences from those already shown; with the exception of the non-existing drop in pressure at the end. The increase in density after the ion package is significantly smaller, but, as already mentioned, it has very little, if any, significance. The calculated values for the reduced ion mobilities are listed in table 4.7.

The simulated values for the ion mobility are a factor of 3.6 to 2.5 times higher

Table 4.7.: Comparison of the calculated and experimental [59] reduced ion mobilities for $O_2{}^+$ in CO_2

E/N [Td]	$K_{0,\text{lit}}$ [$\text{cm}^2\,\text{V}^{-1}\,\text{s}^{-1}$]	$K_{0,\text{sim}}$ [$\text{cm}^2\,\text{V}^{-1}\,\text{s}^{-1}$]	ΔK_0
100	1.38	4.95	3.575
200	1.47	4.47	3.00
400	1.50	3.95	2.45
600	1.38	3.43	2.05

than the experimental values. The difference between the simulated and experimental data is decreasing with increasing reduced field strength, similar to the nitrogen system presented in the last section. The calculated results show a clear decreasing trend in contrast to the experimental data, although the differences in the various reduced field strengths in the literature data are much smaller. Due to the lack of literature data for a higher reduced field strength for the $N_2{}^+$ in N_2 system, it is not possible to distinguish if the higher gap between the literature and the calculated results could be caused by the lack of resonant charge transfer. It may very well be that the better matching of the calculated results for $O_2{}^+$ in CO_2 is due to i) the higher reduced field strengths and ii) that resonant charge transfer is not possible. However, even for 600 Td the difference between the literature and the calculated value is greater than the literature value itself.

4.5. Conclusion and Outlook

In summary, the integration of electric fields into the existing DSMC code SPARTA was successfully carried out. First, the functionality checks verified that the electric force is calculated correctly. If no background gas is present, SPARTA with enabled electric fields delivers the correct results. The ions are accelerated as expected in relation to the applied electric field. If background gas is added, the basic behavior of the simulated charged particles is in accordance with qualitative expectations as well. The ions are initially accelerated by the applied field and decelerated to a stable drift velocity by the collisions with the background gas. Thus, the basic requirements for determining drift velocities and the resulting ion mobilities are technically given. The calculation of the first ion mobility of $O_2{}^+$ in N_2 showed that the calculated values for mobility are on the same order of magnitude as the experimental values but almost a factor of two too high. It is also noticeable that the defined boundary conditions are not stable over

the simulation time. Strong fluctuations in the background gas density are observed. This is also noticed by the sudden acceleration of the ions at the end of the drift tube. Here, the ions enter a region in which the background gas pressure became significantly lower, and thus the extent of deceleration due to collisions decreased. However, it is also observed that the ions travel through the drift tube mostly with stable background gas pressure. In the region that the ions had already traversed, a significant increase in pressure is observed. Nevertheless, by subsequently examining the main simulation parameter, it was found that this influence of the ions on the neutral gas disappears as soon as the resolution in time and the simulation gird are sufficiently small. The relationships of the mean free path and these parameters established in the literature are used to improve the models. However, this has the consequence that the geometry size dimensions have to be reduced by a factor of 0.01 to keep the computation time and the numerical effort within a feasible range. It is shown that the ions have a significant effect on the background gas in the simulation, which should not be so pronounced. They are pushing the neutral gas particles together and form a compression wave. However, this wave does not have a large effect on the drift velocities. The compression wave is formed directly behind the ion ensemble and not in front of them. As shown in different cases, the ions traverse a large area with stable background densities that is related to the given background pressure. In case of reduced ion mobilities, no changes in the parameter set did not result in a significant improvement. Therefore, it is decided to keep the default boundary conditions for all further calculations. Interestingly, for longer time step lengths, significantly better values for ion mobilities are obtained. The reason is that the values for the velocity output by SPARTA is smaller than the velocity calculated from the distance traveled and the time of flight. Thus, although better values were determined, they cannot be relied upon in terms of stability and reliability. The reason for this is not investigated further due to the complexity of the problem and the size of the SPARTA framework. Additionally, two more pairs of ions and background gas are investigated under variation of the reduced field strength. It is found that the deviation of the ion mobility from the experimental data decreases with an increase in the reduced field strength. There is still a difference of $2.13\,\mathrm{cm^2\,V^{-1}\,s^{-1}}$ (1.30 to 3.43) between the values even in the best case. Since this difference is caused by the exceedingly high drift velocity of the ions, and since the acceleration by the electric field is correct, the issue must be found in the collision model. It appears as if that the ions do not experience enough collisions on their travel through the drift tube or are thus not sufficiently decelerated. This rational also explains why the mobility values

improve with higher field strength. Due to the higher field strength, the residence time of the ions in the drift tube is shorter, and thus the total number of collisions with the background gas decreases. By artificially increasing the collisions, i.e., by quadrupling the ion radius, a much better ion mobility is achieved. Finally, it was shown that the determinations of the ion mobilities with simultaneous consideration of the effect on the background gas are not straightforward. The deviation of the determined mobilities from the experimental data is too large and the reason for this issue is currently not known.

For this reason, another approach for the determination of ion mobilities in IMS systems is developed in our research group. For this purpose, the ion dynamics simulation framework (IDSimF) [61] is used. In this framework, it is possible to calculate ion trajectories in neutral background gas under the influence of electric fields, while not modeling the background gas particles explicitly. As stated above, the collisions model is crucial for the quality of the determination of calculated mobilities. The collision model used is based on the molecular dynamics (MD) approach. Newtonian equations of motion are solved for each individual collision of ions with the background gas particles. The acceleration acting on the particles is determined via an MD force field. This force field is a combination of the 12-6 Lennard-Jones potential, which models the repulsion over short distances between two non-bonding particles, and an ion induced dipole moment potential, which describes the attraction forces over long distances. In general, this approach allows much more accurate determinations of ion mobilities than the SPARTA approach [62], while information regarding the effect of the ions on the background gas is lost in this process. However, with the approach chosen in this work this is currently only qualitatively possible at best.

5. Modeling of a Transfer Stage between a HiKE-IMS and a TOF-MS

This chapter describes a method for the determination of the effects of an ion transfer system on ions traversing this stage. An ion guide located between a high-kinetic energy ion mobility spectrometer (HiKE-IMS) and a time-of-flight mass spectrometer (TOF-MS) is analyzed in detail with respect to the kinetics and collision energies of charged particles. First, the neutral gas flow is modeled with the DSMC code SPARTA. Two different approaches are chosen for this purpose: One is a fully resolved three-dimensional model; the other is a simplified two-dimensional axisymmetric model. The results of these two models are compared and discussed. Subsequently, the obtained results are used to determine the ion trajectories and kinetic energies of the transferred ions. This is done using the commercially available simulation program SIMION. In addition, a simple and fast method for the transformation of neural gas flow data from SPARTA to SIMION is described.

5.1. Introduction

To obtain additional information about the chemical dynamics within a HiKE-IMS, a TOF-MS instrument is coupled to the exit of the mobility analyzer. For an efficient transfer of ions from the IMS into the TOF-MS, an ion funnel followed by a quadrupole ion guide is used within a differentially pumped vacuum housing (transfer stage).

The transfer stage bridges the pressure difference between the IMS with a drift gas pressure of about $15\,\mathrm{mbar}$ to the high vacuum region of the mass spectrometer with background pressure of $7 \times 10^{-6}\,\mathrm{mbar}$. The transfer stage must transport most of the ions from the exit of the drift tube efficiently to the inlet of the MS system. In this process, electric fields are used to focus the ions within the neutral gas flow. This section investigates the first segment of the transfer stage represented by the quadrupole. Ion-molecule reactions establishing ion-bound cluster equilibria are essential in the HiKE-IMS. The clusters population distribution is strongly related to the energy the clusters
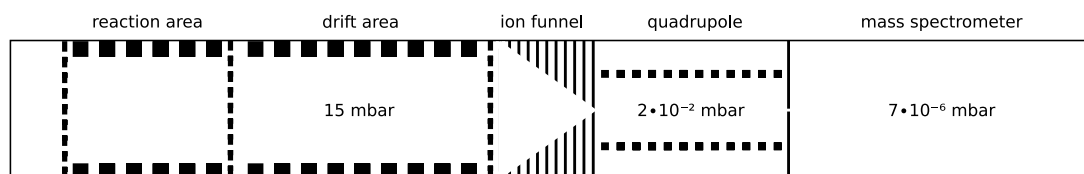
Figure 5.1.: Sketch of the HiKE-IMS (left segment), the transfer stage consisting of the ion funnel and the segmented quadrupole (center) and the mass spectrometer (right segment).

gain or lose during their lifetime. To assess the impact of the transfer stage on these clusters, the energy balance of the molecules involved during the transfer is estimated. The kinetic energy of the ions is determined as a descriptive characteristic. In the first approach, the neutral gas flow is modeled at the entrance of the segmented quadrupole. For this purpose, the SPARTA framework is used.
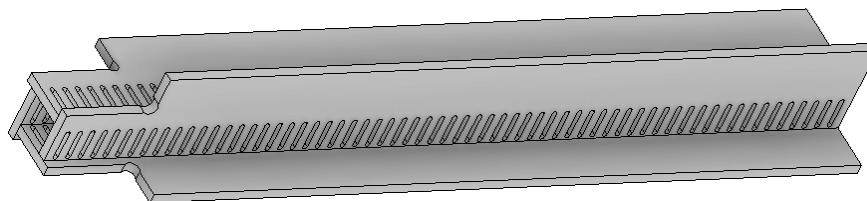
Figure 5.2.: CAD model of the transfer quadrupole. Shown are just four printed circuit boards on which the electrodes are located. Since the structure lacks the open line of sight between the rods of a classical quadrupole, there are openings in the plates to reduce the pressure on the inside.

This quadrupole is constructed using four printed circuit boards (PCBs, cf. fig. 5.2 and fig. 5.3). A two-dimensional axisymmetric model cannot be derived directly from the real model because of the angular geometry. For this reason, a modified two-dimensional approximate model is created (cf. fig. 5.4). This model is later compared with a fully developed three-dimensional model.

The advantages of the two-dimensional axisymmetric model are significantly faster calculation times, less complex geometry, and smaller size of the result data sets. In section 5.3 the calculated results of the two models are compared and evaluated.
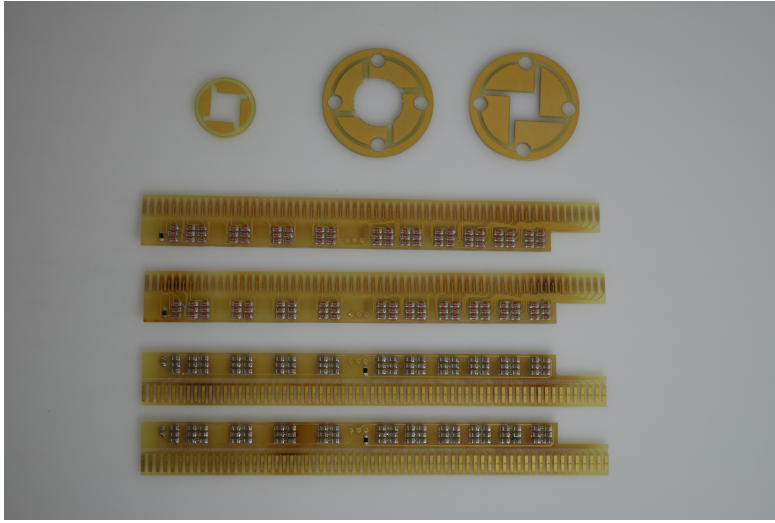
Figure 5.3.: Photograph of the four main printed circuit boards with the three associated locking rings.
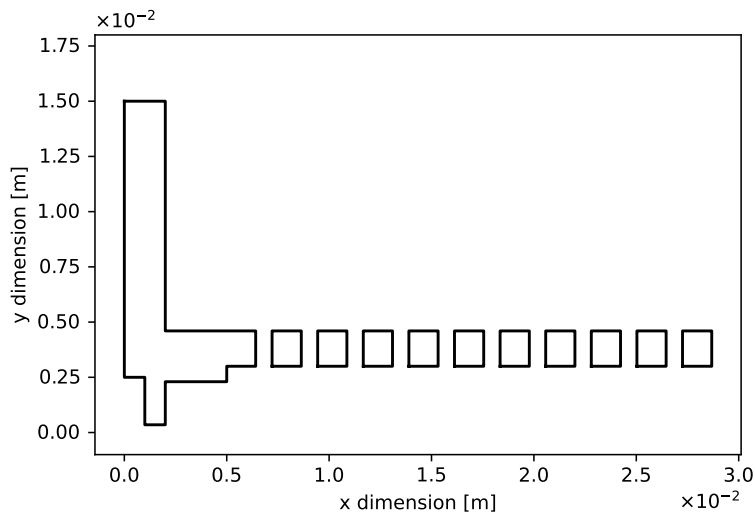
Figure 5.4.: Geometry of the two-dimensional axisymmetric model of the transfer quadrupole. The symmetry axis is with the x axis in this plot. The spacing between the different segments matches that dimension of the three-dimensional geometry.

In the next section, ion trajectories are computed considering neutral gas flow profiles obtained by gas flow simulations. The kinetic energy of the ions is determined from these trajectories. In addition, the required transformation of the output data from the neutral gas flow into a suitable input format for SIMION calculations is important in multiple parts of the work (see section 6.4.3).

5.2. Simulation Setup for the Neutral Gas Flow

The input parameters for the calculation of the neutral gas flow are obtained from experimental data. The inlet pressure at the entrance of the quadrupole is experimentally determined to be approximately 15 mbar. The outflow areas in both models (two-dimensional approximation and full three-dimensional model) are similar. The PCB quadrupole is surrounded by a flange cross, which is pumped on one side. Due to computational effort, the model is limited to a length of 0.02 m in the x dimension.

5.2.1. The Three-Dimensional Setup

The simulation parameters for the full three-dimensional model are listed in Table 5.1.

Table 5.1.: SPARTA simulation parameters for the three-dimensional neutral gas flow simulation of the PCB quadrupole.

Parameter	Value	
Dimensions	3	
Spatial simulation domain [m]:		
x	5×10^{-4}	0.02
y	-0.011	0.011
z	-0.011	0.011
Simulation grid resolution	3.95×10^{10} [cells/m^3]	
n_ρ	3.7×10^{23} (approx. 15 mbar)	
F_{num}	1×10^{19}	
Number of particles	16 948 853	
Timestep size (Δt)	2×10^{-9} s	
Species	N_2	
Collision model	VSS	
Number of time steps	150 000	

Here, n_ρ stands for the number density of the entire gas mixture. For three-dimensional simulations, the unit of the specified density is the number of particles per volume. For the two-dimensional case, the unit is the number of particles per area, since the z dimension thickness of the simulation box is equal to one. The F_{num} parameter sets the ratio between real and simulation particles. For example, a value of 1×10^{19}

means that one particle in the simulation represents 1×10^{19} real particles [1]. For a future explanation of the chosen collision model, see section 3.5.

Figure 5.2 shows the CAD model of the quadrupole. For the SPARTA simulation, a slightly simplified model is used (cf. fig. 5.5). In addition to the CAD model shown in Figure 5.2, the front end of the vacuum cross tube closest to the quadrupole and the inlet orifice are also considered in the three-dimensional SPARTA model.
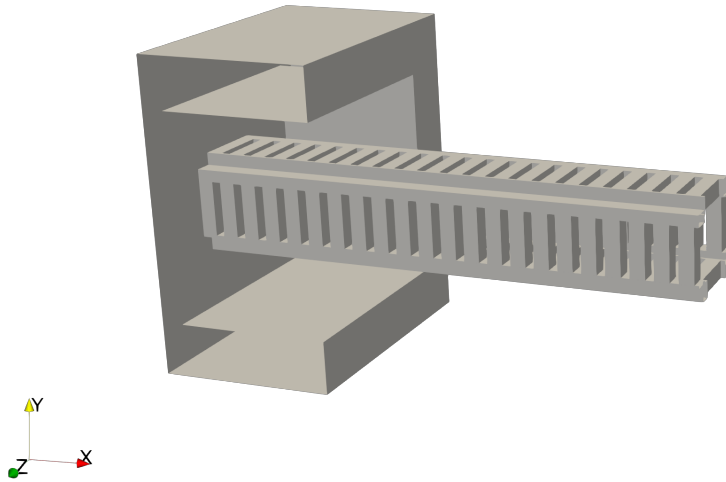
Figure 5.5.: Intersection of the simplified three-dimensional model of the PCB quadrupole with a section of the vacuum cross tube and the inlet orifice.

All curved shapes, such as the circular orifice in the front plate, are removed from the model, as this caused several error messages in SPARTA. It is a challenging task to design a geometry that is suitable for the simulation and still close to the real set-up. The particles are introduced upstream of the quadrupole, directly in front of the orifice. The top, bottom, left, right, and back side are defined as outflow areas. This means that particles that hit such boundaries are allowed to leave the simulation domain. All values derived from the numerical model of the neutral gas flow are determined at a time when the simulated system is in steady state.

5.2.2. The Two-Dimensional Setup

The simulation parameters for the two-dimensional simulation are listed in Table 5.2.

Table 5.2.: SPARTA simulation parameters for the two-dimensional neutral gas flow simulation of the PCB quadrupole.

Parameter	Value	
Dimensions	2	
Spatial simulation domain [m]		
x	5×10^{-4}	0.02
y	-0.011	0.011
Simulation grid resolution	1.77×10^7 [cells/m^2]	
n_ρ	3.7×10^{23} (approx. $15\,\mathrm{mbar}$)	
F_{num}	1×10^{16}	
Number of particles	$1\,125\,166$	
Timestep size (Δt)	$2 \times 10^{-9}\,\mathrm{s}$	
Species	N_2	
Collision model	VSS	
Number of time steps	$300\,000$	

In Figure 5.6 the model of the two-dimensional axisymmetric model is shown. The light blue area marks the location, where the new particles are introduced to the simulation domain (red dotted line).

Figure 5.6.: Two-dimensional axisymmetric geometry of the PCB quadrupole. The red dotted box marks the simulation domain. The bottom line of this rectangle describes the symmetry axis. New particles are introduced in the blue area.

5.3. Comparison of the Two- and Three-Dimensional Simulations

The SPARTA calculations are used to determine the neutral gas flow and pressure profiles. Pressure and velocity distributions are significant for the dynamics of the ion motion within the neutral gas. Therefore, the calculated flow profiles have to be transferred to the SIMION model for the calculation of ion trajectories and ion energy distributions. Since the ions and neutral gas particles must pass through the small orifice at the front of the quadrupole, the area near the central axis through the quadrupole is the most relevant region for the ion trajectory simulation. The pressure and velocity profiles along the center (main) axis of the quadrupole structure are calculated with the Paraview software [8] and the "Plot Over Line" (POL) filter. This filter calculates the values of the point-centered variables along a given line in an XY-plot. If necessary, the filter uses interpolation algorithms to determine the values at the selected location [58].

5.3.1. Comparison of Flow Profiles at the Center of the Simulation Domain

In the two-dimensional case, the POL filter is applied close to the symmetry axis (cf. fig. 5.7). In the three-dimensional case, the POL filter is located exactly in the center of

the orifice. The length of the cutline is $0.02\,\mathrm{m}$ and is equal for both cases and corresponds to the total simulation domain.
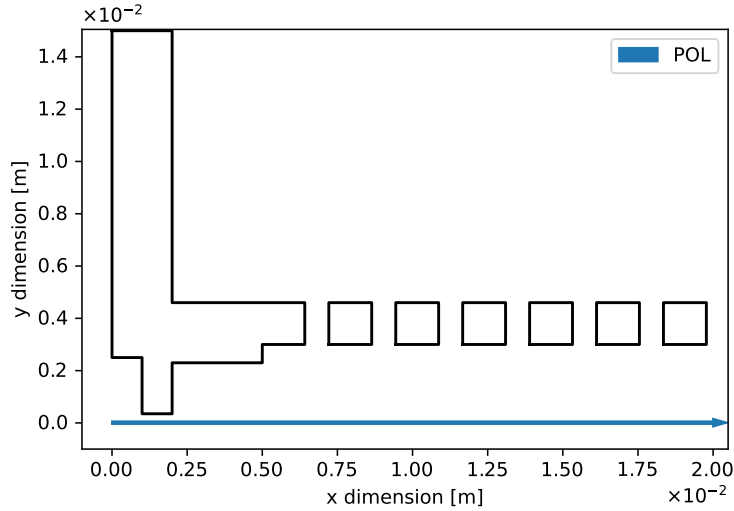
Figure 5.7.: Two-dimensional axisymmetric geometry of the PCB quadrupole. The blue arrow indicates the cutline of the POL filter and the rotational axis.

The comparison of pressure profiles (cf. fig. 5.8 top) shows only minor differences between the two- and three-dimensional models. The boundary conditions at the front of the entrance of the quadrupole are identical. Within the first $2.5\,\mathrm{mm}$ the pressure drops significantly. After $2.5\,\mathrm{mm}$, minor differences are observed, but the terminal pressure after $20\,\mathrm{mm}$ is identical. Inspecting the flow velocities in the x direction (cf. fig. 5.8 center), a similar pattern becomes apparent. The curves rise rapidly, with a maximum of about $600\,\mathrm{m\,s^{-1}}$ in the three-dimensional case and $520\,\mathrm{m\,s^{-1}}$ in the two-dimensional case. Additionally, the x positions of the two maxima are almost identical; however, different final speeds are reached. The final speed is $550\,\mathrm{m\,s^{-1}}$ in the three-dimensional simulation and approx. $200\,\mathrm{m\,s^{-1}}$ higher than in the two-dimensional approximation. This is the first time an effect of the smaller number of particles in the two-dimensional simulation is noticeable. In the three-dimensional case, the number of particles is larger by a factor of about fifteen. This can be seen in the rectangular velocity jumps at higher x values. These large deviations occur because of the low absolute number of particles. The average value is clearly more affected by the individual particle velocities.

In comparison, the radial speeds are similar after 5 mm (cf. fig. 5.8 bottom). In the simplified two-dimensional simulation, a significant increase at 2.5 mm is observed, which is not present in the full three-dimensional case. These observations could be due to the fact that in the two-dimensional case, an axisymmetric geometry is used. In this case, the x axis is not only the axis of rotation, but also the axis that passes through the center of the quadrupole entrance orifice (fig. 5.6). In the three-dimensional case, there is no such rotation axis. The conditions are not completely identical, as the generated values are determined exactly on the axis in the 3D case and just above the axis in the two-dimensional case. Nevertheless, in the three-dimensional case, a much lower increase in the radial velocity is noticeable. This may depend on the emulation approach of the two-dimensional axisymmetric simulation for a three-dimensional space. After this increase, the two velocity curves equalize again. The rectangular steps in the two-dimensional velocity curve are even more pronounced here. In addition to the lower absolute number of particles, this is also due to the fact that even fewer particles move away from the main flow direction. As mentioned above, the focus of these simulations is the determination of ion trajectories and energies. Accordingly, the area at higher pressure, i.e., at the beginning of the quadrupole, is significantly more important than the area at lower pressure; thus, more collisions of ions with the background gas take place in the entrance region of the quadrupole. Consequently, the first 2.5 mm have the greatest impact on the ion trajectory, as well as on the ion energy influenced by collisions. Further downstream on the ion pathway, the pressure and the number of potential collision partners are significantly lower. Therefore, the numerical artifacts of the traces and the different velocities of the two simulations are not really decisive at higher x values. In short, the pressure and x velocity traces are almost identical. Only the initial peak in the radial velocity distribution distinguishes the two models.
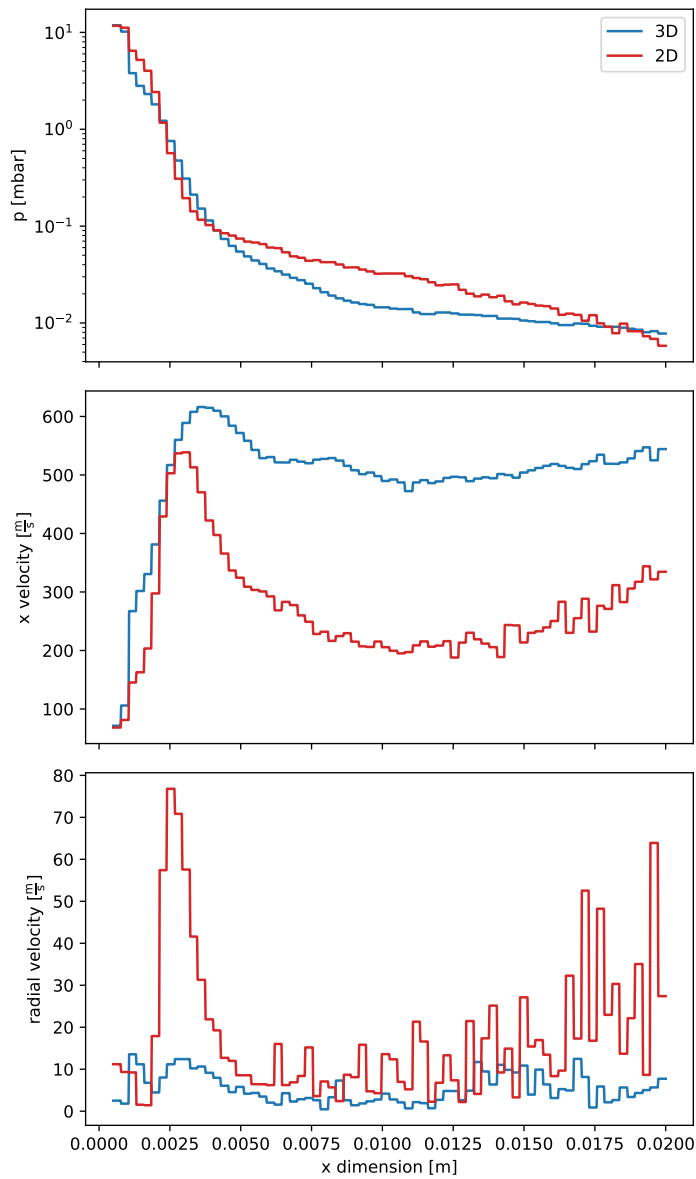
Figure 5.8.: Pressure (top), velocity in x direction (center) and radial velocity (bottom) profiles as function of the x position in the center of the PCB quadrupole. The blue traces represent the three-dimensional and the red traces the two-dimensional axisymmetric model. The pressure profiles are plotted on a logarithmic scale.

5.3.2. Comparison of Flow Profiles close to the PCB Electrodes

In this comparison, the cutline of the POL filter in the three-dimensional model is located directly at the holes of the PCB quadrupole. In this case, the geometry of the two-dimensional axisymmetric model is almost identical to the local geometry near the cutline in the three-dimensional model.
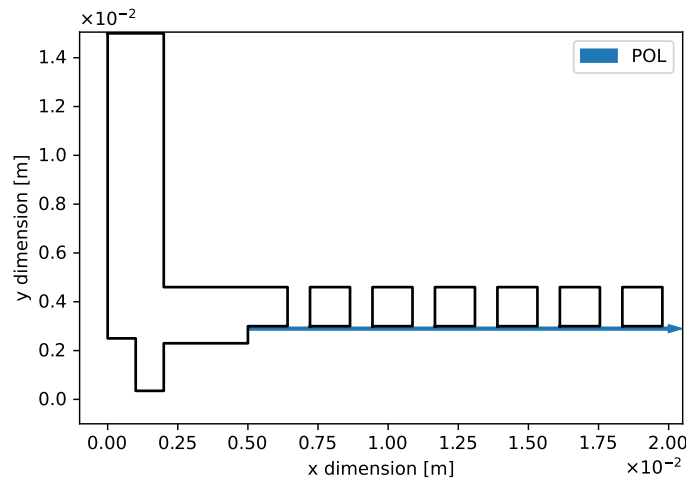
Figure 5.9.: The two-dimensional axisymmetric model. Blue line represents the path of the POL filter.

All profiles start at an x value of 5 mm (cf. fig. 5.9). Both pressure profiles have the same characteristics. The local minima in the traces are at the x positions where the holes are located on the circuit board. However, they are significantly different in absolute value. With higher x values, both become closer, just before the end of the simulation domain, where they drift apart again (cf. fig. 5.10 top). The same applies to the velocity in the x direction. Most of the time, the absolute values differ significantly. In the three-dimensional case, an initial rapid increase is observed, followed by a relatively constant value. In the two-dimensional case, it is exactly the opposite (cf. fig. 5.10 center). Considering the radial velocity is considered, the traces are almost identical, with the exception that the velocities calculated in the three-dimensional case are initially significantly higher. With an increasing x values, the velocities equalize to the same level (cf. fig. 5.10 bottom). Overall, the differences in pressure and velocity near the electrodes are much larger than those at center of the quadrupole. This is consistent

with the fact that the two models also differ significantly at this point. While the spatial environment in the center of the quadrupoles is more or less identical, pronounced differences can be seen at the edges. As seen in Figure 5.5, the cutouts in the electrodes are not completely continuous. There are no such cutouts where the electrodes intersect. The two-dimensional model, on the other hand, has continuous holes when the structure is rotated along the x axis. In addition, the rotation creates a round shape rather than an angular shape, as in the three-dimensional case.
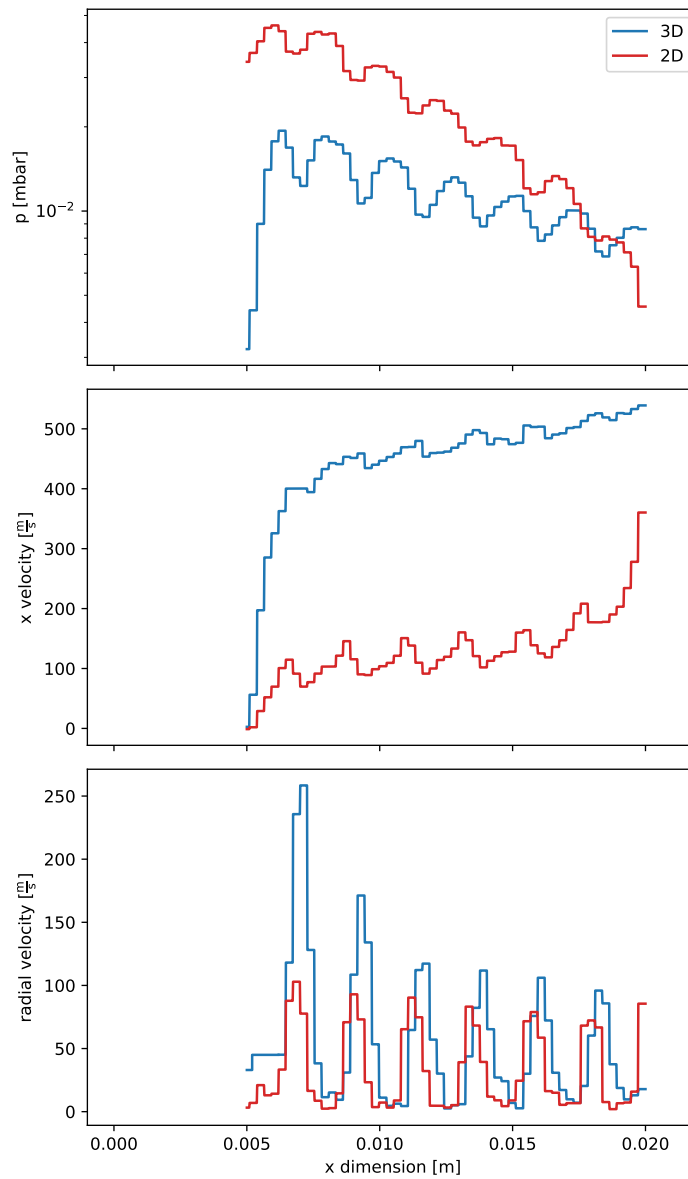
Figure 5.10.: Pressure (top), velocity in x direction (center) and radial velocity (bottom) profiles as function of the x position close to the electrodes of the PCB quadrupole. The blue traces represent the three-dimensional and the red traces the two-dimensional axisymmetric model. The pressure profiles are plotted on a logarithmic scale.

5.3.3. Creating a Flow Field for Ion Trajectory Calculations

It has been shown that the difference varies greatly depending on the spatial domain of comparison. While the differences between the two- and three-dimensional models are still small at the center of the quadrupole, they become more apparent at the edge of the model. The flow calculations are used as input parameters for the ion trajectory calculations. Since charged particles in a focusing quadrupolar field are to be calculated, the residence probability of these near the edges of the geometry close to the electrodes is rather low. Therefore, the determined profiles from the two-dimensional model are used for further calculations. Pressure profiles, as well as the velocity distribution in the x direction, are expressed as analytical functions and are then incorporated into the ion trajectory model. This method is the simplest way to use the generated profiles in calculating the ion trajectories. For each profile, one or more fitting functions are used for the modeling (fig. 5.11).
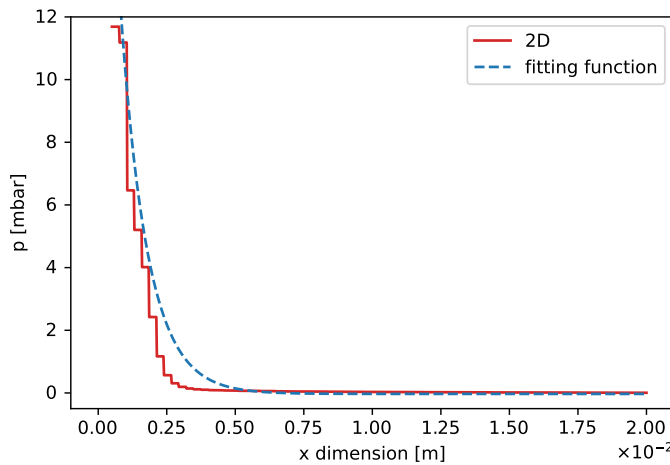
Figure 5.11.: Red trace: Calculated pressure profile along the main axis of the two-dimensional axisymmetric simulation.Blue trace: Applied fitting function in blue.

An exponential function of the form $a \cdot e^{bx} + c$ is used to describe the pressure profile. The maximum value is set to the inlet pressure of around 15 mbar. The same procedure is used to describe the velocity profiles. Since a two-dimensional axisymmetric flow simulation is used as a data source for the three-dimensional ion trajectory sim-

ulation, the two-dimensional profile is rotated numerically to obtain an approximate three-dimensional flow profile. Since the symmetry axis is also the x axis of the coordinate system, the radial length of the vector $|\vec{l}_{\text{y,z}}|$ at a specific x position is determined by:

$$|\vec{l}_{\text{y,z}}| = \sqrt{y^2 + z^2} \tag{5.1}$$

Here, y and z are the corresponding Cartesian coordinates. The radial velocity v_{r} is divided into a y and z part, and the length of the y, z vector is used as normalization factor, to obtain the components of the radial velocity in the three-dimensional space:

$$v_{\text{y}} = \frac{y}{|\vec{l}_{\text{y,z}}|} \cdot v_{\text{r}} \tag{5.2}$$

$$v_{\text{z}} = \frac{z}{|\vec{l}_{\text{y,z}}|} \cdot v_{\text{r}} \tag{5.3}$$

All values and fitting functions are listed in appendix A.1.

5.4. Ion Trajectory Simulations at the Entrance Area of the Quadrupole

The simulated trajectories are determined to obtain an estimate of the kinetic energy distributions of the ions that enter the quadrupole area. For this purpose, the SIMION software is used. The hard-sphere model packaged with SIMION (HS1) is slightly modified and used as a collision model for the trajectory simulations. The analytical functions determined in the previous section are implemented into the collision model. Depending on the x position, the local pressure from the pressure function is applied. Moreover, the velocity of each ion is additively composed of the velocity calculated in SIMION and the neutral gas velocity. The kinetic energy is considered to get an overview of the energy balance of the ion ensemble

$$K_{\text{e}} = \frac{1}{2} \cdot m \left(\sqrt{v_{\text{x}}^2 + v_{\text{y}}^2 + v_{\text{z}}^2} \right)^2 \tag{5.4}$$

The kinetic energy K_{e} is calculated from the mass m and the velocity components in each spatial direction v_{x}, v_{y} and v_{z}. These values are obtained from the SIMION simulation. The two main factors that influence the velocity and thus the kinetic energy are the applied electric field in the quadrupole and the collisions the ions experience.

Table 5.3.: SIMION simulation parameters for the ion trajectory simulations at the entrance area of the PCB quadrupole.

Parameter	Value
Dimensions	3
Background pressure	calculated SPARTA profiles
Number of ions	$1,000$
Ion mass	$55\,\text{Da}$
Ion charge	1+
Initial kinetic energy	$0.3\,\text{eV}$
Reduced field strength	$120\,\text{Td}$
Background gas	Air
Temperature	$20\,°\text{C}$
SIMION version	8.1

For trajectory calculations, $1,000$ ions with an *m/z* of 55 and an initial kinetic energy of $0.3\,\text{eV}$ are initialized at the entrance aperture of the housing. As the models before, the simulation domain is limited to a length of $20\,\text{mm}$ in the x direction. The ions undergo around $997 \pm 254(1\sigma)$ collisions during their flight through the first $20\,\text{mm}$ of the quadrupole, as shown in fig. 5.12.

5.4.1. Collisions depending on the Ion Location

It is estimated that most collisions of the ions occur in the first $5\,\text{mm}$ of the calculated pressure drop in the quadrupole. Then the mean free path increases and the associated collision frequency decreases rapidly.

Figure 5.13 demonstrates that most collisions occur within the first $5\,\text{mm}$ as expected. In contrast, the total collision number remains at a rather constant value in the region further away from the inlet into the quadrupole. Accordingly, collisions are the most important factor for the change of the kinetic energy at the beginning of the trajectories. Downstream of the high-pressure region at the entrance, acceleration by the electric field becomes much more significant, as described in the following.
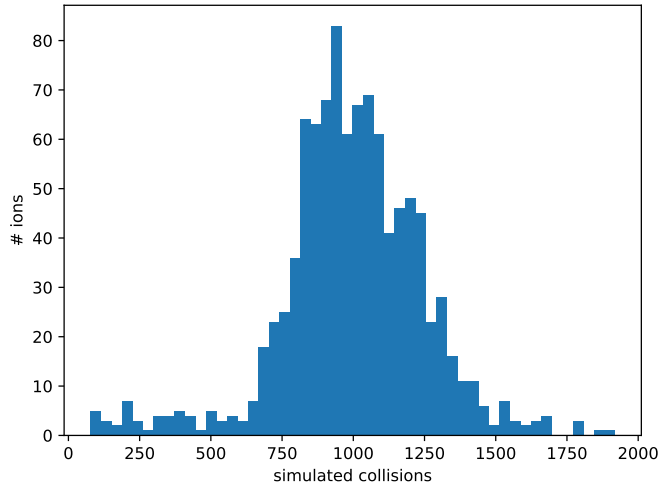
Figure 5.12.: Frequency of simulated collisions in the first 20 mm of the quadrupole. The mean value is 997 with a standard deviation of 254(1σ). The minimum number is 77 and highest value is 1919.
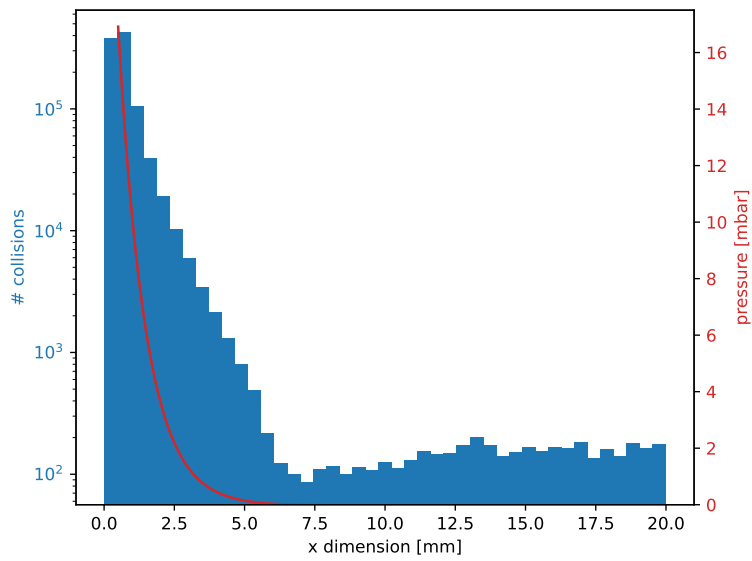
Figure 5.13.: Number of collisions on a logarithmic scale as a function of the x position of the ions (blue area). In comparison, the simulated pressure as a function of the x position is plotted (red curve).

5.4.2. Kinetic Energy Distribution

The calculated velocities of the simulated ions are used to determine the kinetic energy according to eq. (5.4). The kinetic energy and position of the ions are recorded in $1\,\mu s$ intervals. Figure 5.14 shows the kinetic energy distribution in dependence on the x position of the ions. The number of simulated ions is comparatively high at the quadrupole entrance. On the one hand, this is due to the larger residence time in this area, which is caused by the higher local pressure there. On the other hand, this is due to the smaller available volume caused by the quadrupole entrance orifice geometry. As the axial x position increases, the ion density near the central axis decreases. Furthermore, the number of collisions, and therefore the energy exchange with the background gas, decreases, and the energy gain by the electric field gradient increases. This leads to an overall increase of the kinetic energy and a broader energy distribution. The maximum of the distribution shifts towards higher kinetic energies. Overall, an increase in kinetic energy is verified.
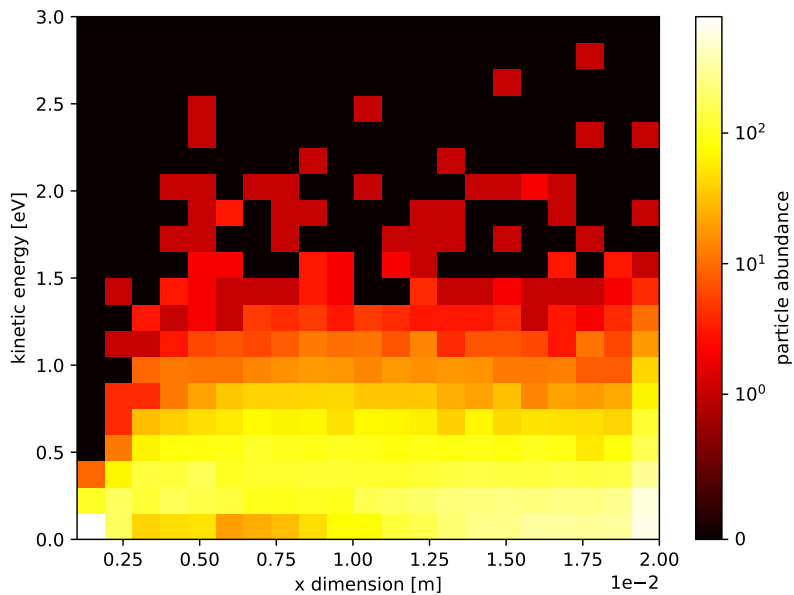
Figure 5.14.: Kinetic energy distribution versus the ion x position. The colors maps the particles abundance. The sampling points are determined every microsecond. Accordingly, the number of points in the area with higher pressure is higher.

5.5. Conclusion and Outlook

It is demonstrated that the use of two different simulation approaches for the description of ion trajectories in a HiKE-IMS - TOF-MS transfer stage is readily possible. Integration of neutral gas flows into these simulations is easy to realize, albeit some limitations. It has been shown that the two-dimensional axisymmetric simulation results are similar to the three-dimensional model results under some constraints. With less complex geometries, further advantages of the two-dimensional axisymmetric simulation become apparent: One issue not mentioned so far is the creation of the three-dimensional model. It may appear trivial at first glance, especially if CAD models are already available, but there are some difficulties to overcome. First of all, the creation of a simulation grid from these CAD models needs to be handled with care. As shown in chapter 4, the grid resolution is directly coupled to other simulation parameters, such as the time step size or the velocity achieved by the particles. In addition, the grid resolution has to match the spatial dimension of the underlying geometry model. It has to be fine enough to resolve all corners and edges of the model. Especially curved elements cause some problems. With increased grid resolution, the computation time increases as well. Another advantage of the two-dimensional simulation is that a significantly smaller amount of particles (approx. one million) is required to populate the simulation domain, as compared to approx. seventeen million in the three-dimensional case (cf. table 5.1 and table 5.2). Since all particles have to be stored in the random access memory (RAM) of the computing node, the memory requirements of the three-dimensional case are significantly higher. In contrast, the creation of a geometry for the two-dimensional axisymmetric simulation is much easier. The model becomes simpler, even if some geometric features cannot be reproduced directly. One simulation run with the two-dimensional model took a few days, whereas the three-dimensional model ran for about one month.

It was shown that, especially on the main axis through the system, the differences in the neutral gas flow are rather small. In particular, a similar final pressure was determined. The development of the pressure also shows good accordance in both cases. The velocity profile in the main direction also shows qualitatively the same profiles, although the velocities calculated in the three-dimensional case are in part significantly higher after the first 2.5 mm. However, towards the end of the simulation domain, the two begin to converge again, although a clear difference in the absolute values remains. The radial velocity distribution shows differences within the first few millimeters. In the two-dimensional case, a peak can be seen, which is absent in the three-dimensional one. After this peak, both settle back to the same level. When the profiles are not compared

on the main axis, more pronounced differences become apparent. While pressure and radial velocity are similar and differ only in the absolute values achieved, the velocities in the direction of the main axis differs significantly. Since the neutral gas flow profiles are subsequently used to determine the energy gained by charged particles passing through the quadrupole, the flow profiles at the main axis are selected. This is justified by the quadrupolar field that guides the ions on a stable trajectory along the main axis. Thus, the residence probability of the ions near this axis is much larger. A complete three-dimensional neutral gas flow profile would lead to higher coverage, but is more complex in terms of implementation (cf. section 6.4.3).

The selected profiles were described by one or more fitting functions and then transferred to the SIMION model. The application of fitting functions provides a versatile approach to integrate the neutral gas flows into the ion trajectory calculations. All profiles were generated from the two-dimensional axisymmetric simulation. To extend the radial velocity profiles to the higher-dimensional space, they were numerically rotated. It was not clarified which of the two approaches is closer to the experimental setup that describes the velocity distribution. Here, the experimental data must be determined to describe the integrity of the two models. Also, the influence of the simplified three-dimensional geometry was not further investigated.

The ion trajectory calculations and the consideration of the kinetic energy distributions were readily done. It was shown that the model behaved as expected. Most collisions of the ions with the neutral gas occur at the beginning of the quadrupole, since the local pressure is high in contrast to that of the remaining areas of the quadrupole. Accordingly, the mean free path is much smaller, and the collision frequency is higher. Since the quadrupole has a direct current (DC) field in addition to the radio frequency (RF) field, which describes a gradient between the entrance and the end of the quadrupole, the ions also accelerate when passing through the structure. Thus, the observed increase in the kinetic energy of the ions is also plausible. In the artificial simulation case, all ions started with a fixed kinetic energy at the orifice of the quadrupole entrance. Due to collisions, the broadening of the kinetic energy distribution is observed as expected. In this work, the ion trajectories are represented with a basic approach, which can be extended. It is, e.g., possible to determine the effects of the electrical parameters of the quadrupole transfer stage by simultaneous consideration of the transfer performance. Furthermore, the influence of the transfer on the kinetic energy distribution can be estimated. By introducing a chemical reaction model, any chemical reaction can also be described because of the energy balance of the ions, allowing a more comprehensive view

of the entire system.

6. Determination of Droplet Size Distributions generated by Electrospray Ionization

This chapter addresses the determination of the droplet size distribution produced by the electrospray ionization (ESI) process. Electrostatic induction is used for that purpose. It is demonstrated using a Bruker HTCplus mass spectrometer as an example geometry. One focus of this chapter is to generate supporting models to simplify the interpretation of experimental results. Second, this chapter covers more in-depth the description of ion trajectory simulations. This includes the application of fully spatially resolved neutral gas flow and pressure profiles, as well as the use of an evaporation model.

6.1. Introduction

Electrospray ionization is one of the most common ionization methods in mass spectrometry. The formation of charged droplets is the initial step of the complex analyte vaporization and ionization process. The droplets decrease in size due to the loss of neutral solvent molecules which leads to an evaporation and fission cascade, which is significantly affected by the ion source conditions. Experimental evidence shows that charged droplets from an ESI needle traverse the ion source region and are aspirated as intact particles into MS vacuum systems. This phenomenon is only sparsely described in the literature; current mass spectrometry textbooks covering ESI do not mention this process at all. In the latter, quantitative droplet evaporation in the ion source is generally assumed.

6.1.1. The ESI Process

Detailed information on the ESI process, experimental investigations and molecular dynamic simulations of charged droplets within this process are comprehensively compiled in a recently published dissertation [63].

For a better understanding of the following investigations, only a brief overview of the ESI process is given: Electrospray ionization is a commonly used ionization technique for mass spectrometry [64–69]. The concept was first presented by Dole et al. [64]. The analyte is dissolved in a liquid solution and then sprayed from a narrow capillary within a strong electric field gradient in the ion source of the mass spectrometer. This process usually takes place under atmospheric pressure conditions. During the spray process, charged droplets are formed, which are guided by electric fields towards the entrance of the mass spectrometer. Because of the interaction with the typically heated background gas in the ion source, these droplets evaporate and eventually release bare gas phase ions at the end of the process. These ions are detected afterwards in the mass spectrometer analyzer. Unlike other ionization techniques, ESI is considered a "soft" technique. Larger, more fragile molecules such as proteins can be ionized by ESI without significant fragmentation of the molecular ion.

The ESI process can be divided into three main steps [68, 70]: The first step is the formation of charged droplets at the ESI emitter tip. Second, the droplets undergo a shrinking and fission cascade. These processes are driven by multiple forces, primarily the interaction of the droplets with the background gas and electrostatic forces within the droplet: Due to solvent evaporation, induced by the temperature of the background gas, the droplet evaporates, which leads to an increasing charge density within the droplet. When the charge density reaches a critical limit, the surface tension of the droplet is overcome, resulting in a fission event. The last event in this cascade is the Coulomb explosion [71], leading to the formation of the bare gas-phase ions.

Droplet Formation

As shown in fig. 6.1, the charged droplets are emitted from the tip forming Taylor cone. Typically, voltages of up to 5 kV are applied between the ESI emitter and the entrance system of the mass spectrometer [68]. The resulting string electrical field gradient leads to polarization of the liquid. Depending on the polarity of the applied voltage, positive or negative ions gather near the meniscus of the liquid, leading to the formation of the Taylor cone [72, 73]. Due to electrodynamic effects within the liquid, droplets of almost uniform size leave the cone in a jet toward the MS entrance [74–76]. The process takes place since the Coulombic repulsion of the charges is higher than the surface tension of the liquid. After a droplet is emitted, the meniscus of the liquid reforms a spherical shape and the process of charge accumulation at the meniscus tip is repeated until the limit is reached in the next cycle. Under ideal conditions, this cone-jet mode is a stable process
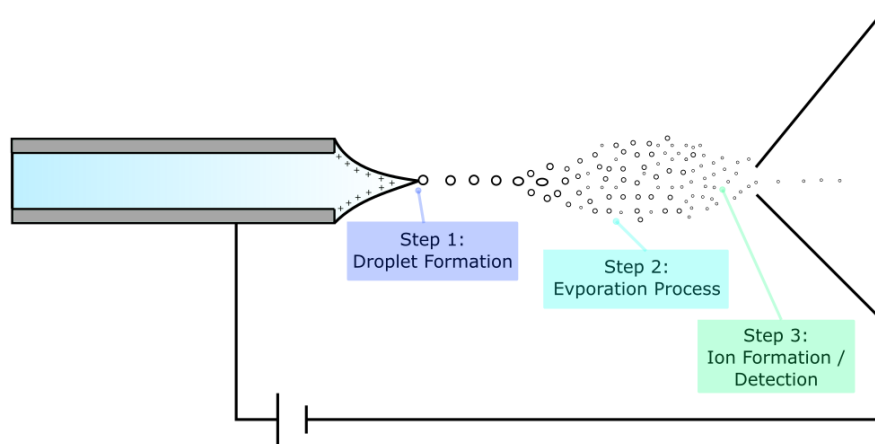
Figure 6.1.: Schematic of an ESI emitter in an ion source. A Taylor-cone forms at the tip of the ESI emitter needle. A high voltage is applied between the ESI needle and the inlet of the mass spectrometer. Charged droplets are formed at the tip of the Taylor-cone, which decrease in size as they approach the entrance of the mass spectrometer system [63].

and leads to a constant droplet formation. In the real world, the spray constitution heavily depends on various parameters. There are numerous different possible spray modes [74] generating a large span of droplet sizes, which is also experimentally observed. The experimentally determined droplet sizes vary from 1 to 200 µm [43, 77–84]; most reported sizes are between 20 and 100 µm.

Evaporation Process

The second step after droplet emission is the evaporation of the solvent. Usually, ESI sources have systems installed such as heated dry gas stream into the ion source chamber to support the evaporation process [67]. During the evaporation process, more and more solvent molecules enter the gas phase, and the charge density inside the droplet increases. At some critical point, the electrostatic force of the solvated charges overcomes the surface tension of the droplet, and the charged droplet splits into smaller ones (Coulomb explosion). As one droplet creates several smaller droplets during this process, the charge number per droplet becomes smaller, and the new droplets are more stable. This

process repeated several times. Contrary to what the name suggests, the characteristic of the Coulomb explosion is the emission of smaller droplets in a jet-like way from the mother droplet [79]. The general process of electrostatic disintegration of droplets was first described by Lord Rayleigh, who found the following equation to describe the limit of charges Q a droplet can contain by a given radius r [71]:

$$Q = 8\pi(\epsilon_0 y r^3)^{\frac{1}{2}} \tag{6.1}$$

with ϵ_0 as the vacuum permittivity and y the surface tension of the liquid. With this equation, a limit can be determined at which number of charges a droplet becomes unstable, which is called the Rayleigh limit. Mostly, the disintegration of droplets starts at 80 % to 100 % of their calculated Rayleigh limit [43, 78]. Furthermore, a typical droplet lifetime is around 1 s at a travel velocity 45 to 55 cm s^{-1} [78]. The lifetime exceeds the residence time in a typical ion source with a length of 2 to 5 cm; droplets are thus most likely entering a mass spectrometer vacuum system.

Ion Formation and Detection

The last step of the ESI process is the release of analyte ions from the droplets. However, the formation of bare analyte ions is not the primary focus of this work and is therefore only briefly described. There are several models that attempt to describe this process. First, there is the charge-residue model (CRM) that was developed by Dole. He suggested that at the end of the solvent evaporation and droplet fragmentation process there is only one analyte molecule left in the droplets. After the solvent has completely evaporated from these aggregates, only the charged analyte molecule remains and is transferred to the mass spectrometer [64]. This kind of process is considered to be the primary formation process of lager analyte ions [70]. In addition, there is the ion evaporation model (IEM), which was introduced by Iribarne and Thomson [85, 86]. They postulate that formed analyte ions are still solvated by a few solvent molecules. This process applies better to smaller analytes [70]. For the sake of completeness, the chain ejection model of Konermann is also be mentioned [87]. To summarize, all proposed mechanisms end with essentially bare analyte ions, which is contrary to experimental evidence [88]. Because of their relatively high charge, the droplets have high electrical mobility in the gas phase, which enables a path to easily penetrate the mass spectrometer vacuum system, even when ion optical elements are present to extract ions from the neutrals.

6.1.2. The Rayleigh Limit

As described in the previous section, the Rayleigh limit represents the number of charges a droplet can contain before fission occurs due to the Coulomb explosion. Throughout this chapter, droplets are simulated at different locations on a mass spectrometer. Since the actual size of the droplets in each of these instrument regions varies, a selection of different droplet sizes is considered to investigate the dynamics of droplets with different sizes. It is assumed that the solvent is water with a surface tension of $72.8\,\mathrm{mN\,m^{-1}}$, a density of $1.0\,\mathrm{g\,cm^{-1}}$ and a vacuum permittivity of $6.85 \times 10^{-12}\,\mathrm{F/m}$. With eq. (6.1), the volume V_s of a sphere, the density ρ (cf. eq. (6.2)) the mass m of a droplet can be determined by (cf. eq. (6.3)):

$$V_\mathrm{s} = \frac{4}{3}\pi r^3 \text{ and } \rho = \frac{m}{V} \tag{6.2}$$

$$m = \frac{4}{3}\pi r^3 \rho \tag{6.3}$$

In combination with the number of charges at the Rayleigh limit, the m/z for a given droplet radius can be determined. For this chapter eleven different characteristic droplet sizes with corresponding masses and charges are calculated (see table 6.3). Depending on the region of interest in the mass spectrometer vacuum system, only a selection of them is used.

6.1.3. The Implementation of Electrostatic Induction in SIMION

The encyclopedic definition of electrostatic induction is: "The electrostatic induction [is] the modification in the distribution of electric charge on one material under the influence of nearby objects that have electric charge" [89]. A negatively charged object brought near an electrically neutral object induces a positive charge on the near side and a negative charge on the far side of the neutral object due to the electrical force acting on the mobile charge carriers in the object. This phenomenon is described by an extension of Kirchoff's current law, the Ramo-Shockley theorem. It links the current flowing in an external circuit, for example, a current amplifier, to the motion of the charge within the system [90]. A generalization of the original theorem relates microscopic charge motion with macroscopic current in complex systems. The Ramo-Shockley theorem states that the current induced I on the $\mathrm{k^{th}}$ electrode by N particles is as follows:

$$I_{\mathrm{k}} = \sum_{i=1}^{N} q_{\mathrm{i}} \cdot v_{\mathrm{i}} \cdot E_{\mathrm{k}}(r_{\mathrm{i}}) \tag{6.4}$$

With q_i as the charge of the ii^{th} free charge and its velocity $v_{\mathrm{i}} \cdot E_{\mathrm{k}}(r_{\mathrm{i}})$ weighted with the weighting field in position r_{i}. The weighting field E_{k} represents the geometrical coupling between the free charge at the point r_{i} and the electrode k. It is determined by solving the Laplace equation with all other electrodes set to zero volts and the electrode k at $1\,\mathrm{V}$. The total current is calculated by summing over all free charges i. An alternative form of eq. (6.4) gives the induced charge on the electrode $\mathrm{k^{th}}$:

$$q_{\mathrm{k}} = -q_{\mathrm{i}} \cdot V_{\mathrm{k}}(r_{\mathrm{i}}) \tag{6.5}$$

Here, V_{k} is the weighting potential analogous to the weighting field E_{k} [91] [92]. With these relationships, the induced current and the induced charge of the passing ions can be determined. To calculate induced currents in an ion trajectory simulation, an already existing SIMION user program is modified and used.

6.2. Capillary Spray

In this section, an existing experimental setup is retrofitted with a device capable of characterizing charged droplets originating from an ESI source via the detection of induced currents. Originally, this setup was designed for optical measurement methods. First, some simple edge cases are investigated. Therefore, the shape and general response of the recorded induced ion current transients are analyzed in these test cases. Subsequently, a simplified flow field of the bulk gas flow exiting the MS inlet capillary is created with OpenFOAM. This flow field is used as input parameter for ion trajectory and ion current transient calculations in SIMION. These results are then evaluated based on their potential significance in a real-world experiment.

6.2.1. Description of the Experimental and Simulation Setup

As mentioned above, the modeled experimental setup was initially intended for optical measurements. It was proposed to represent the first vacuum stage of a Bruker HCTplus mass spectrometer. The ions and potentially large charged particles/droplets enter the first vacuum stage from an atmospheric pressure (AP) ion source through an inlet capillary. The vacuum region is evacuated by a vacuum pump (cf. fig. 6.2). Due to the inlet

capillary, the flow to this first region is restricted, so the pressure in the first vacuum stage is in the range of a few mbar. The experimental setup is based on the construction of the real MS instrument. It is primarily a sealed metal chamber in which the pressure is regulated to 5 mbar by an attached vacuum pump. The ions and neutral gas particles enter this volume through an MS inlet capillary with a length of approximately 20 cm, which connects the detection volume and an ionization region. This ionization region is at atmospheric pressure. Additionally, windows are placed to the chamber on one side for the intended optical measurements.
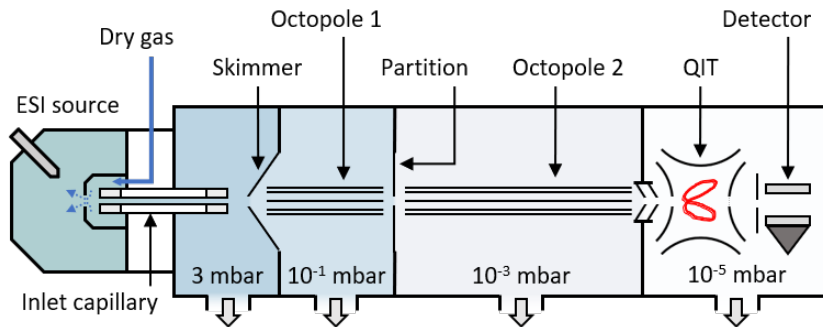
Figure 6.2.: Schematic sketch of the Bruker HCTplus instrument with attached Apollo AP-ESI source [93].

For induction current detection, three additional electrodes are added to the model of the experimental system. The first electrode is the metal-coated capillary end itself. This is followed by the detection electrode and finally the counter electrode (cf. fig. 6.3). The voltage gradient is applied between the capillary end held at ground potential and the counter electrode, biased at -200 V. Because the simulations consider cations, the counter electrode imposes an attractive potential gradient for the simulated charged particles.
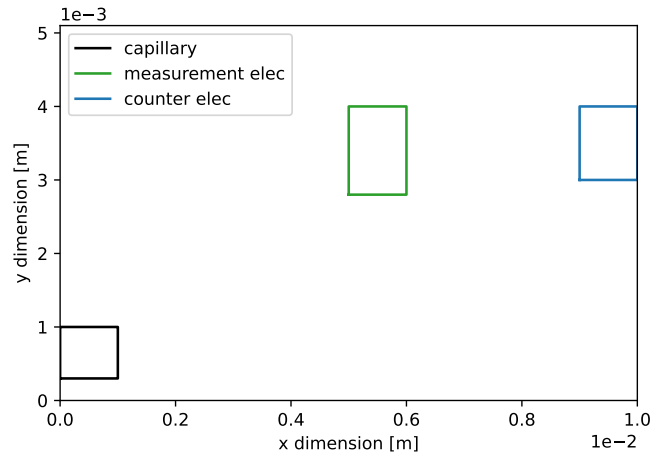
Figure 6.3.: Scheme of the axisymmetric model geometry for the ion current detection in the first vacuum stage of the Bruker HCTplus MS instrument. The x axis is the symmetry axis. The black box represents the capillary end with an inner diameter of 0.6 mm. The detection/ion current pick up electrode is drawn in red and the counter electrode in blue.

The inner radius of the capillary is 0.6 mm, 5.6 mm for the detection, and 6.0 mm for the counter electrode, respectively. A three-dimensional model is used for the SIMION ion trajectory and induced current simulations (cf. fig. 6.4). The ions' starting position is within the inlet capillary in the last millimeters before the capillary end.

To obtain more accurate results for the neutral gas velocities and the pressure profile, the two-dimensional model is geometrically extended for the OpenFOAM calculations (cf. fig. 6.5). The capillary extends 18 cm to the left, corresponding to the actual length of the capillary. This is necessary to be able to calculate the correct pressure drop within the inlet capillary. Furthermore, the model was extended 8 cm to the right, to capture more of the expanding gas jet from the capillary.

The experimental recording of the transients is performed with the RTE1054 oscilloscope (Rohde & Schwarz GmbH & CO. KG, Munich, Germany). To determine small currents, the use of a sensitive charge amplifier, in the case of the current experiments, a DHPCA-100 (Femto Messtechnik GmbH, Berlin, Germany), is mandatory. This device has a maximum amplification factor of 1×10^8 V/A, which allows the detection of current pulses in the pA (1×10^{-11} A) range, provided the noise background is sufficiently low.
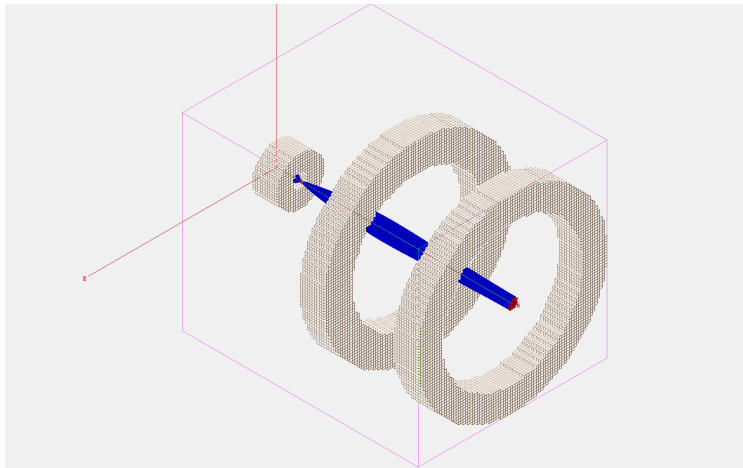
Figure 6.4.: Three-dimensional SIMION model for the ion current detection located in the first vacuum stage of the Bruker HCTplus MS instrument. The blue lines represent example ion trajectories.
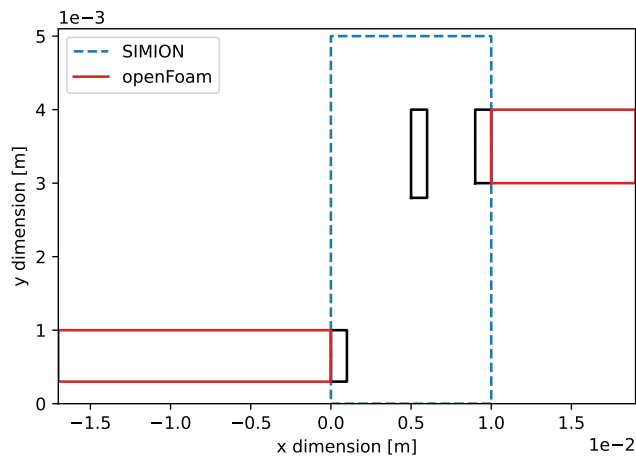
Figure 6.5.: Scheme of the axisymmetric model geometry for the ion current detection located in the first vacuum stage of the Bruker HCTplus MS instrument extended for the OpenFOAM simulations. The area marked by the blue dotted line describes the section which is used for the SIMION calculations. The extended geometry for the OpenFOAM neutral gas flow simulations is drawn in red.

6.2.2. Investigation of the Response of the SIMION Induction Model to Edge Cases

In the following part some responses of the simulated induced current to interesting edge cases are presented. To simplify the model, no background gas and no collision model is applied. Therefore, there is no neutral background gas flow. Although these simplifications render the applicability of the model results to actual experimental observations less meaningful, they provide insight into the behavior of the model under ideal conditions. For this consideration, only one type of particle or droplet is used. In this case, it is an aggregate with a diameter of 3.7 nm carrying a total of ten positive charges, which regarded as the reference droplet in this section. The diameter is calculated with the Rayleigh limit for this number of charges. For all further calculations, 1000 ions per species are introduced into the simulation domain.

Product of Charge and Velocity
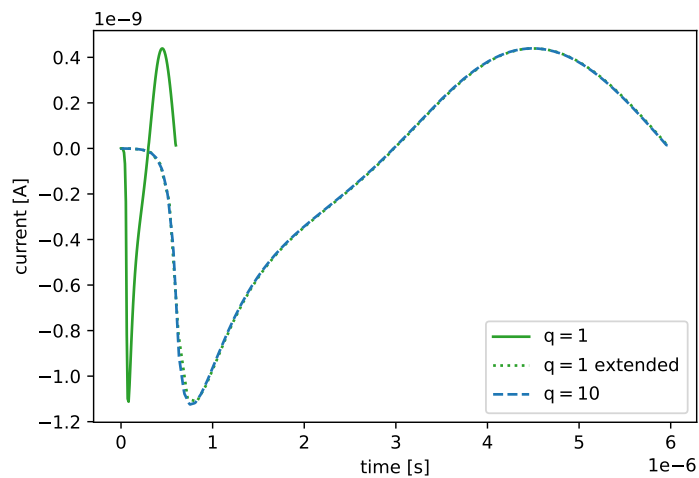
Figure 6.6.: Induced current versus the total time of flight. The dotted green trace describes the transient induced by a droplet with one positive charge and a ten times higher velocity. The solid green trace is extended in time by a factor of ten for a better representation of the shape of this trace. The blue trace describes the induced current of the reference droplet species (10 charges, *m/z* 1597.2).

As stated in eq. (6.4) the induced current I_k at the detection electrode depends on the product of the charge q and the velocity v of the charge carrier. This means that under certain circumstances, ions with different charges cannot be distinguished if the product of charge and velocity results in (almost) identical values. For easier calculations, the velocity of the droplet species (diameter: 3.7 nm; charge: 10+) at the beginning of the detection electrode is determined with an electric gradient of -200 V between the capillary and the end electrode (cf. fig. 6.3). Generally, the ions are under constant acceleration, but in this case, their velocity is set to a constant value. Both species do not experience any kind of velocity change. The speed of the reference droplet is set so 1671 m s^{-1}, this is the speed this droplet would have obtained at the beginning of the detection electrode, if the acceleration is turned on. The charge number of the comparison species is one and therefore the velocity increases by a factor of ten, to 16 710 m s^{-1} resulting in an identical charge/velocity product. As shown in fig. 6.6 the shape of the induced current over time appears to be similar for both species (cf. fig. 6.6; dotted traces). Due to the higher speed of the comparison species, the transient is clearly compressed. Under ideal conditions, it should be possible to distinguish between these two species. The extent to which this is possible under real-world conditions is discussed later. However, it turns out that the shape of the transient is basically identical but on different time scales.

Spatial Distance of Ions passing through the Detection Electrode

As seen in fig. 6.6, the passing ions induce a negative current first by approaching the electrode. After they pass the electrode, the polarity of the induced current changes, until the distance of the ion to the electrode becomes too far, and the induced current finally drops to zero. It needs to be clarified whether an ion passing the detection area of the electrode at a certain distance cancels the previously induced current of the previous ion in a regular stream of ions. For this purpose the ions are separated into two packages containing 1000 ions each and are launched with a time delay. The time delay corresponds to the time it takes for one ion package to pass the detection electrode. It is determined by the quotient of the distance between the starting point of the ions and the detection electrode, and the velocity of the ion package. The time delay has a value of 0.625 µs. As shown in fig. 6.7, the two ion packages can be clearly identified in the transient as two minima in the green trace. Thus, the shape of the trace changes, but a total cancellation of the induced current is not observed. For this reason, the original course of the reference ion package (cf. fig. 6.7 blue trace) is fitted with a
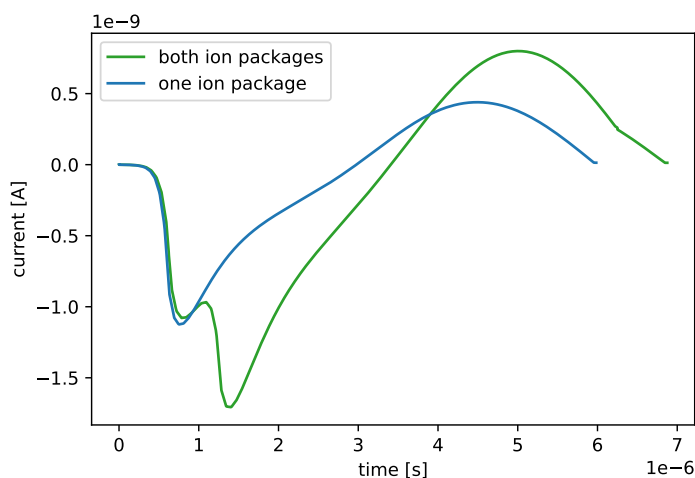
Figure 6.7.: Induced current with the total time of flight. The green trace shows the induced ion current signal resulting from two ion packages which are started with a time delay of 0.625 µs between each other. For comparison, the signal from a single ion package passing by the detection electrode is shown in blue.

higher-order polynomial and then integrated. The overall sum of the integral is positive; thus, elimination by subsequent ions is not possible since the positive part predominates. This behaviour is expected as the charged particles experience a constant acceleration, and therefore, the product of charge and velocity increases with time.

Detection of Droplet Signals with Constant Ion Current

As previously described, larger aggregates are rather the exception. The probability of detecting smaller ions, respectively bare analyte ions, is significantly higher. Since the primary focus of the planned experiment is the detection and possibly identification of droplets, the question is whether charged droplets can be detected in a continuous stream of smaller ions. For this purpose, the 1000 H_3O^+ ions are uniformly introduced into the simulation in a time range of 30 µs. Groups of droplets with 1, 10, and 100 individual droplets are added after 2 µs to this base ion current. The corresponding calculated transients are shown in fig. 6.8. Only with the largest groups of 10 and 100 additional droplets a noticeable effect on the recorded transient is recognized. The effect is still very small for 10 droplets and becomes clearly apparent only for the largest group of 100 added droplets. This suggests that the detectability of droplets in a continuous
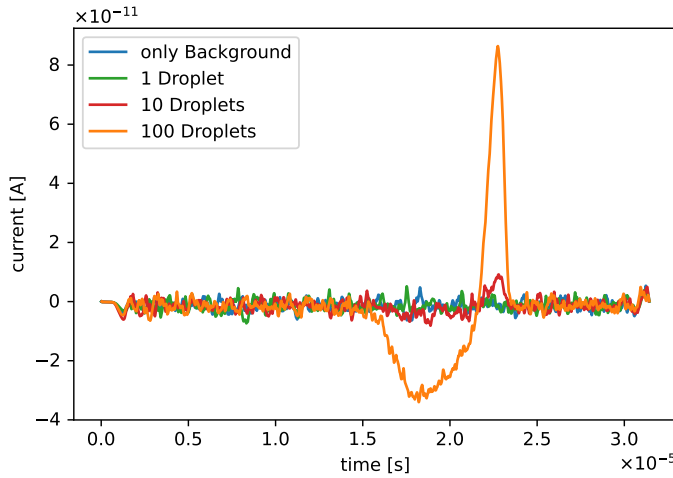
Figure 6.8.: Induced current versus the total time of flight. Transients represent 1000 background ions distributed over time with additionally introduced reference droplets.

stream of other charged particles is likely to be difficult. It is also important to note that the 100 droplets have reached the detection electrode almost simultaneously. If they are distributed over a longer period of time, it will have a negative influence on the detection sensitivity for such aggregates. However, the droplet species considered in this simulation is very small in terms of droplet size and charge number. With larger droplets, the effect on the recorded current will obviously be much more pronounced. The peak height generated by the passing droplet is linearly related to the number of charges in the droplet (see eq. (6.4)).

Overall, the simulations show that under ideal conditions, it is theoretically possible to recognize droplets by their induced current upon passing through a detection electrode. A total cancellation of the signal due to the passing of multiple droplets seems improbable. Also, ions or droplets with the same charge and velocity product should be distinguishable from each other with sufficient temporal separation between the droplets. Nevertheless, an issue becomes apparent here: If both of the variables, respectively, velocity and charge, are unknown, it is nearly impossible to determine the size or charge number of the droplet by induced current detection alone. With the aid of the transient records, very large aggregates in the stream can be spotted. In addition, if one of the two variables could be determined by another detection method, it appears to be feasible

that these methods can provide a possibility for sizing droplets.

6.2.3. Calculated Flow and Pressure Profiles

For a more detailed description of the droplet and ion trajectories in the gas expansion at the inlet capillary exit, the neutral gas flow and the pressure profile are determined with an OpenFOAM simulation. In this case OpenFOAM instead of SPARTA is used, due to the higher pressure in this simulation domain. The simulation parameters are listed in table 6.1. The simulated geometry is shown in fig. 6.9. Since the outflow from the capillary reaches supersonic speeds, a solver with compressible gas enabled is used. A turbulence model is omitted in favor of numerical stability. This could play a role inside the capillary, but is not of particular interest to the questions considered here.

Table 6.1.: OpenFOAM simulation parameters of the system similar to the first vacuum stage of the Bruker HCTplus MS.

Parameter	Value
Dimensions	2 (axisymmetric)
Solver	rhoPimpleFoam (transient)
Timestep size (Δt) [s]	1×10^{-9}
Turbulence model	off
Compressible gas	on
Gas mixture	Air
Input pressure [mbar]	1013.25
Background gas pressure [mbar]	5
OpenFOAM version	8

For the determination of the pressure drop along the inlet capillary, it is extended to its actual length of 18 cm. Thus, the atmospheric pressure is assumed at the entrance of the capillary, and the pressure profile can be described more precisely. The additional extension of the geometry at the right end became necessary due to the appearance of numerical instability at the intersection between the right boundary and the symmetry axis. Since the solver used is of transient nature, the model is extended so that a stable flow is established in the area of interest, i.e., the area around the detection electrode. The results are shown in fig. 6.9. The profiles are mirrored on the symmetry axis.
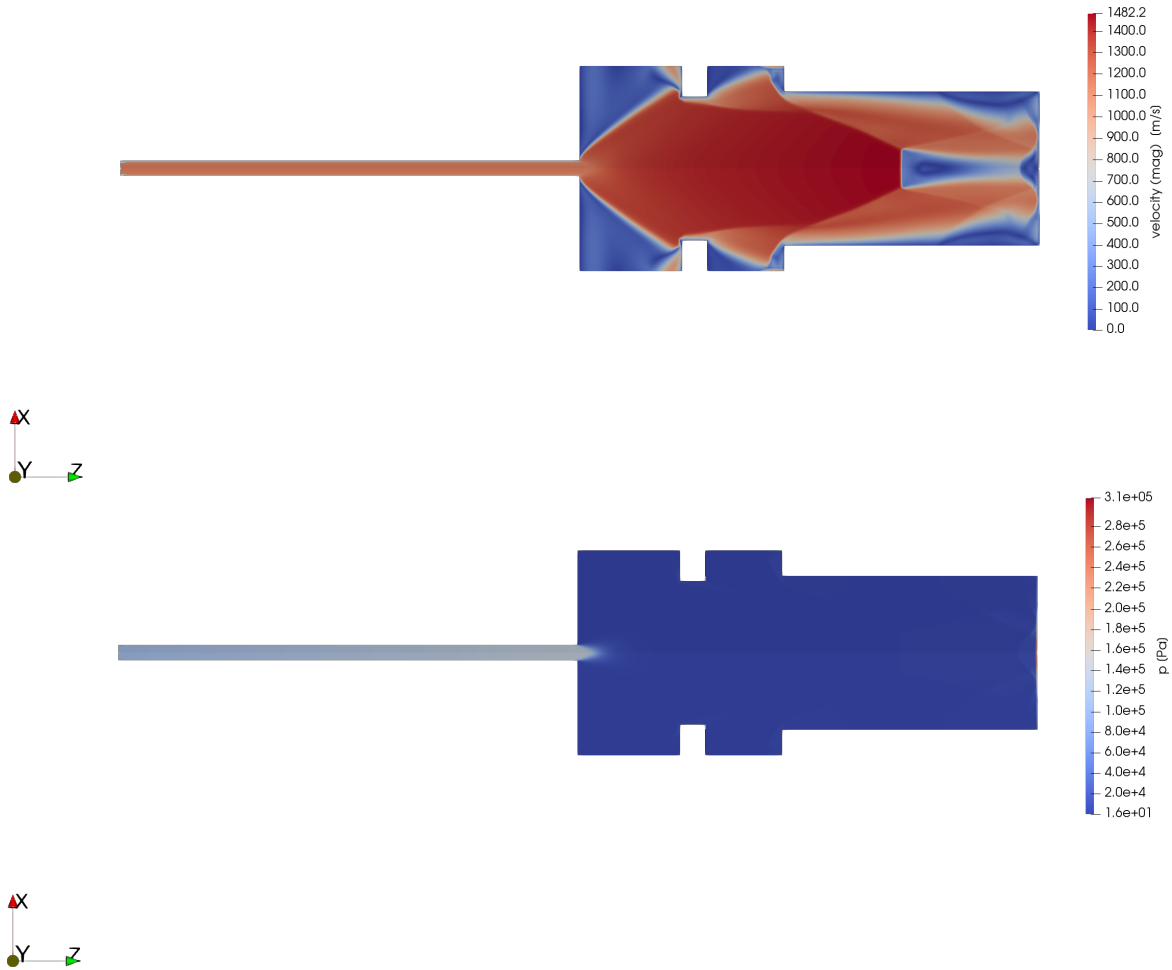
Figure 6.9.: Pressure and flow profiles, mirrored at the symmetry axis (x axis). The magnitude of the velocity profile (top) and the pressure profile (bottom) when a stable flow condition in the area of interest is reached by the transient solver.

In order to be able to use the flow and pressure profile in the SIMION SDS model, the approximate profiles are described by several fitting functions (see appendix A.2) and integrated into the collision model. As in Section 5.3.3, the radial components of the axisymmetric profiles are numerically divided into the y and z directions. After enabling the SDS collision model with the calculated flow and pressure profiles as input parameters, the velocity of the charged particles is slower (cf. fig. 6.10). In addition, the shape of the recorded transient changes, while the maximum signal amplitude remains nearly identical (cf. fig. 6.11).
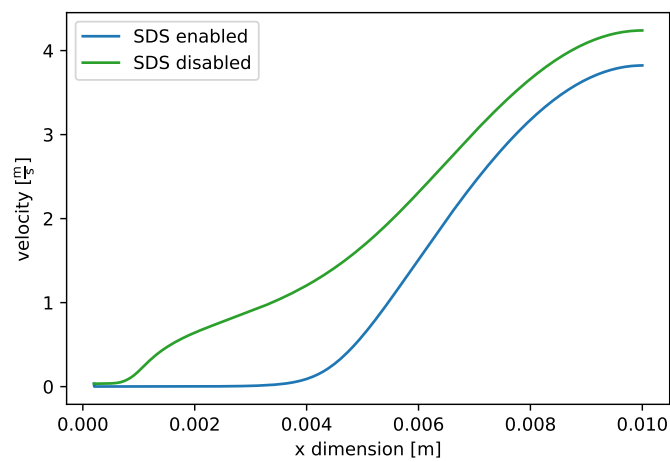
Figure 6.10.: Velocity of one droplet with a radius of 3.7 nm and 10 positive charges in dependence on the x position. The blue line is with the enabled SDS collision model and previously calculated flow and pressure profiles. The green line is without any kind of collision model and profiles.
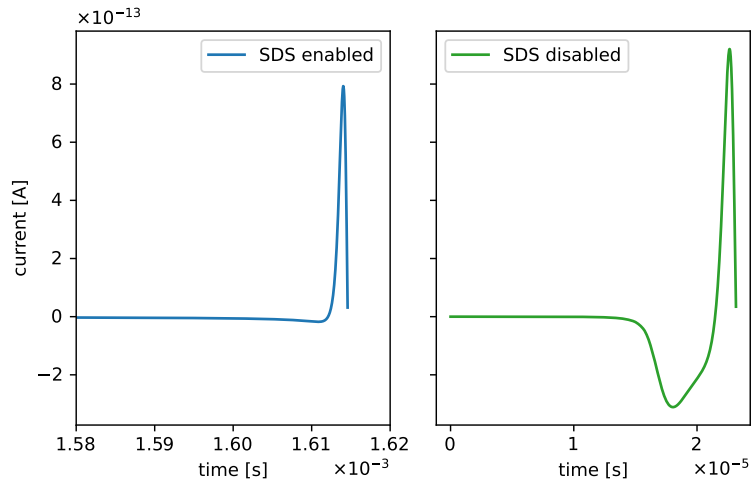
Figure 6.11.: Comparison of the calculated transients of one droplet with a radius of 3.7 nm and 10 charges with (left) and without (right) enabled collision model. The shape differs, but the maximum current remains nearly the identical.

6.2.4. Investigation of Induced Ion Current as a Function of the Particle Size

The SDS model with the previously determined flow and pressure profiles is used for all subsequent ion trajectory simulations to provide an as realistic simulation as possible with the currently available neutral background gas data. The simulation parameters are listed in table 6.2.

Table 6.2.: SIMION trajectory simulation parameters of the system similar to the first vacuum stage of the Bruker HCTplus MS.

Parameter	Value
Dimensions	3
Collision model	SDS (with pre-calculated flow fields)
Number of ions	100
Temperature	298 K
Background gas	air
SIMION version	8.1

For this purpose, eleven different droplet sizes are selected, and their maximum induced current is determined. The size of the droplets is distributed between 3.7 nm and 100 μm. Since it is not clear which size of the particles actually enter the first vacuum stage of a typical MS through the capillary, this wide range of droplets is selected. As always, the droplets are at their Rayleigh limit with the corresponding diameter and charge. The droplet parameter and maximum induced currents are listed in table 6.3.

Since the listed currents are induced by one hundred ions each, a droplet with a diameter of 0.37 μm can theoretically be detected with the detection setup as described above (see section 6.2.1). For smaller droplets, the induced current is probably too small unless a hundred or more of them pass the detection electrode almost quasi-simultaneously.

Figure 6.12 shows the dependence of the current on the diameter, mass, and charge of the droplets. As these values increase, the detected current also increases, as expected. The dependence of the induced current on the diameter of the droplets is described by the following function, with a determination coefficient of $R^2 = 0.999$:

$$I[\mathrm{A}] = \frac{4.34 \times 10^{-7} \cdot d[\mathrm{m}]}{1.37 \times 10^2 + d[\mathrm{m}]} + 2.05 \times 10^{-9} \tag{6.6}$$

Table 6.3.: Droplet parameters with corresponding maximum induced currents of 100 droplets at the same time.

Diameter [µm]	Mass [u]	Charges	Ind. current [A]
3.7×10^{-3}	15 972	10	6.56×10^{-11}
1.7×10^{-2}	1 604 482	100	2.54×10^{-10}
8.0×10^{-2}	1 604 482	1×10^3	8.46×10^{-10}
0.37	1.59×10^8	1×10^4	2.73×10^{-9}
1.71	1.59×10^{10}	1×10^5	8.86×10^{-9}
5	3.94×10^{13}	4.98×10^5	2.02×10^{-8}
10	3.15×10^{14}	1.41×10^6	3.45×10^{-8}
25	4.92×10^{15}	5.57×10^6	6.91×10^{-8}
50	3.94×10^{16}	1.57×10^7	1.16×10^{-7}
75	1.33×10^{17}	2.89×10^7	1.53×10^{-7}
100	3.15×10^{17}	4.46×10^7	1.87×10^{-7}

With d as the diameter of the droplet. It is noted that this function derived from the idealized simulation is not necessarily directly applicable to the actual experiment.
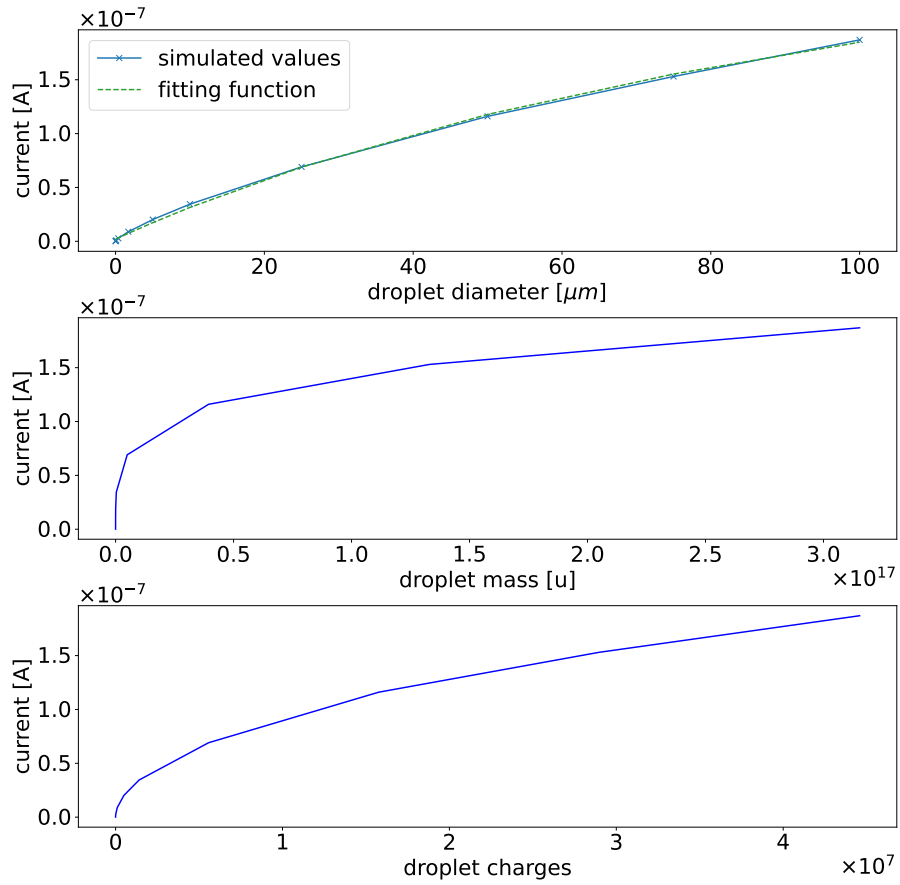
Figure 6.12.: The maximum current detected as a function of the droplet diameter (top), the droplet mass (center) and the number of charges per droplet (bottom). The dependence of the induced current on the droplet diameter it fitted with a function represented by the dotted green line.

6.2.5. Summary

In summary, it has been shown that the existing experimental setup is certainly extendable to detect the charged droplet induced current by adding two more electrodes. However, the distinction between the droplet signal and the background ion current is not necessarily straight-forward. This situation improves as the droplets increase in size or their numbers become larger. Furthermore, a charged particle with 10 000 charges can probably be detected by a combination of available devices, such as the RTE1054 oscilloscope and the DHPCA-100 amplifier. It is noted that no background signals are considered in the idealized simulations. In general, it becomes apparent that detection of the induced current provides another important parameter for the description of large charged aggregates, since there is a clear correlation between the diameter and the induced current. Although this cannot be used to determine the droplet diameter exactly, it probably provides a valuable estimate of the size of the droplets. The method can be used in combination with other detection methods to arrive at a more complete picture of the droplet ensemble. As mentioned above, this particular experimental setup was originally intended to perform optical measurement methods, such as laser scattering measurements. By combining these two methods, it should be possible to obtain more detailed information about the droplet size distribution. In addition, it was shown once again that combining the neutral gas flow and ion trajectory calculations leads to more comprehensive results. The model created in this section can be adapted by obtaining parameters to support the interpretation of experimentally generated data.

6.3. Bruker HCTplus Analyzer Region

The previous section investigated the size distribution of the droplets in the first vacuum stage directly at the exit of the transfer capillary of the Bruker HCTplus. In this chapter, a region is investigated that is located further downstream in the instrument. Previous work [93] has shown that the quadrupole ion trap (QIT) can be replaced by a direct ion current detector (Faraday cup) in this specific instrument, as there is some space available between the second focusing octopole and the subsequent lenses and the Faraday cup (cf. fig. 6.2). In this space, a induced current detection electrode can be placed, which would allow detection of passing droplets.

In this section, an existing SIMION model ([93]) of this area is used, which is extended with two additional detection electrodes. In addition, a neutral gas flow field already exists from SPARTA simulations and is used as input parameter for the ion trajectory

simulations. The instrument settings of the Bruker HCTplus, as the octopole RF frequency and amplitude, add several degrees of freedom to the model. Therefore, a fixed set of instrument parameters is used for all subsequent simulations. The parameter set has a significant influence on the transmission of different droplet sizes. In a multipole, the applied voltages define a mass-to-charge window, in which ions have a stable trajectories. Those without a stable trajectory are deflected and hit the electrodes of the multipole. By dynamically varying these voltages, the entire mass range is scanned, and thus a mass-to-charge spectrum is created. In this case, this entire scanning part is omitted, because the electrical configuration of the instrument significantly increases the complexity of the entire system. The focus is on generating transients with a set of parameters which are stable over time. The results obtained should be considered as a proof of concept. They should give an idea whether it is worth the effort to build such an experimental setup. Therefore, in the following chapter, a fixed configuration of the instrument will be used. However, to date, no experimental data are available.

6.3.1. Description of the Simulation Model

The simulation domain of the HCTplus begins at the exit of the first octopole (cf. fig. 6.2), followed by an octopole partition plate, the second octopole, two focusing lenses, the droplet detection electrodes, and the Faraday cup (cf. fig. 6.13). Electrode potentials used are listed in table 6.4.

Table 6.4.: Electrode potentials for the ion trajectory simulations in the Bruker HTCplus analyzer region.

Electrode	Voltage [V]
Octopole 1 DC	12.0
Octopole partition	6.8
Octopole 2 DC	1.7
Focusing lens 1	−5.00
Focusing lens 2	−60.0
Faraday Cup	0.0

The applied RF voltage has a frequency of $3\,\text{MHz}$ and an amplitude of $75\,\text{V}$. The RF voltages of the neighboring rods are phase shifted by 180°. The interaction of the droplets with the neutral background gas is performed with the HS1 collision model
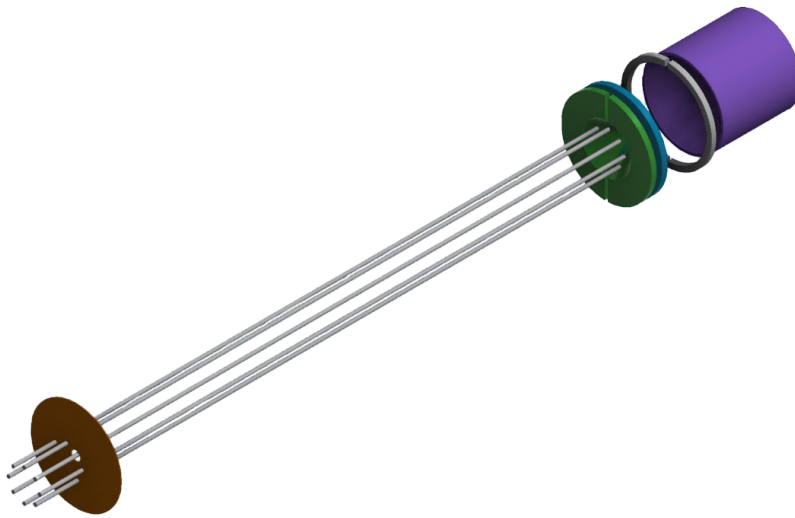
Figure 6.13.: Octopole model used for SIMION trajectory simulations. Electrodes from left to right: octopole 1 rods, octopole partition plates (orange), octopole 2 rods, two focusing lenses (green and cyan), detection electrodes (grey), and the Faraday cup electrode (purple).

due to the low pressure of approx. 10^{-3} to 10^{-5} mbar in the simulated region. The background gas is nitrogen. Position-dependent pressure and background gas velocities are calculated within a SPARTA simulation. The geometric model is based on previous work within the working group [93] and is extended by the two detection electrodes for the droplet induced current (cf. fig. 6.13, gray electrodes). The SIMION base model is also taken from this previous work, including the neutral gas and pressure profiles, and extended to determine induced current transients. All subsequent results are based on the shown configuration. All values and fitting functions for the neutral gas flow are listed in appendix A.3.

6.3.2. Results

Droplets with a diameter exceeding 10 µm are omitted, because penetration of such large aggregates thus far downstream is assumed to be rather unlikely. Under the selected conditions, only a smaller fraction of the introduced droplets reaches the detection electrode and the Faraday cup. In each simulation run, a total of 100 ions of the respective species are introduced into the simulation domain. The introduction area is located at the exit of the first octopole (cf. fig. 6.13). In addition to the induced current, the transmission yield of each species is determined. The transmission yield is defined as the fraction of all charged particles that reach the Faraday cup divided by all introduced particles. This transition yield is mainly influenced by the chosen electrical parameters of the hole system. A sample of the ion trajectories calculated is shown in fig. 6.14.
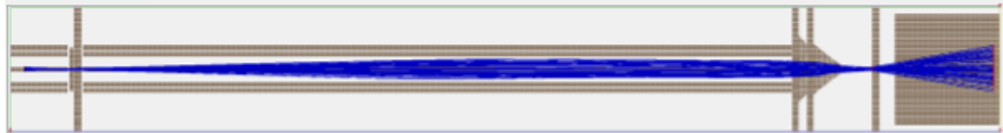
Figure 6.14.: Charged droplet trajectories of 100 charged particles with 10 charges and a diameter of 3.7 µm in the octopole region of the Bruker HCTplus.

Despite the smaller droplets trajectories shown in fig. 6.14, most of the larger droplets hit one of the two focusing lenses at the end of the second octopole while the remaining fraction mostly passes the detection electrode. An example transient signal of the induced current is shown in fig. 6.15. The results for all droplets are listed in table 6.5.
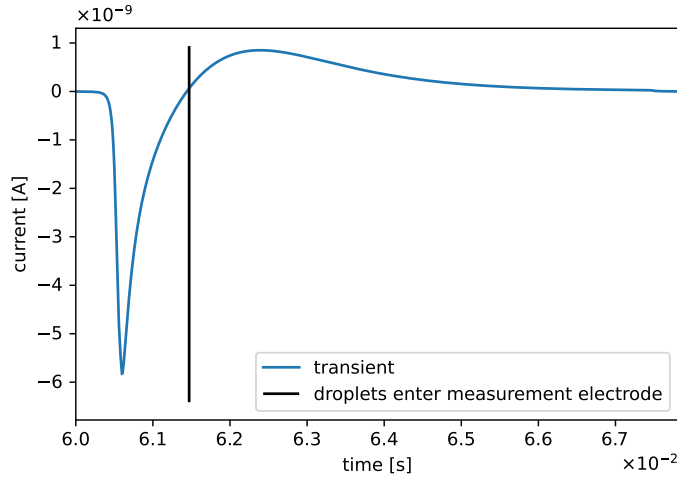
Figure 6.15.: Simulated transient of the model run with the largest droplet of the selected simulated droplet ensemble in the analyzer region of the Bruker HTCplus. The selected species has a diameter of 10 µm and carries approx. 1.41×10^6 charges. Only 26 of 100 droplets have reached the detection electrode. The blue trace represents the recorded transient and the black vertical line indicates the mean time at which the droplet group passes the detection electrode.

Table 6.5.: Particles parameters with the corresponding absolute induced current and survival yields for the given transfer conditions.

Diameter [µm]	Charges	Abs. Ind. current [A]	Transmission Yield [%]
3.7×10^{-3}	10	1.02×10^{-11}	98
1.7×10^{-2}	100	2.18×10^{-11}	20
8.0×10^{-2}	1×10^3	1.04×10^{-10}	22
0.37	1×10^4	5.69×10^{-10}	31
1.71	1×10^5	1.50×10^{-9}	25
5	4.98×10^5	3.78×10^{-9}	28
10	1.41×10^6	5.83×10^{-9}	26

Compared to the results presented in the previous chapter (cf. table 6.3) the induced currents are all smaller. This is due to the fact that significantly fewer droplets, and thus significantly less charge, pass the measuring electrode. As mentioned in the previous section, the information obtained from the detected currents alone is not sufficient to determine the droplet size. In this case, the whole process is more complicated due to the additional degrees of freedom, namely the entire perational parameter set of the instrument (e.g. RF voltages of the octopole). In addition, it is noted that the measurement of induced currents may be disturbed by oscillating electric fields. In the presented case, the field of the octopole or the focusing lens could reach the detection electrode. If this is adversely affecting induced ion current measurements, this needs to be assessed by experimental investigations or electrostatic simulations. In summary, it was be shown that with existing data a comprehensive model of this area of the Bruker HCTplus can be generated. The results of theses simulations can contribute to the correct interpretation of the experimental data. Furthermore, the model can be easily adapted to other boundary conditions, such as specific transfer settings.

6.4. Comprehensive Description of a Simplified ESI Chamber

The aim of this section is to describe a simple experimental approach to directly determine the droplet size distribution that is emitted by an ESI needle. As the ion trajectories become more complex in this scenario, the simplified approach to express flow and pressure fields as simple analytical fitting functions is no longer a valid option. Therefore, the determined flow and pressure fields from a OpenFOAM simulation are converted to SIMION potential arrays, which cover the hole simulation domain with spatially resolved flow information. Since this simulation domain is under atmospheric pressure conditions, the evaporation model (see section 3.6) is be used. Therefore, the main goal is to obtain an ion trajectory simulation with fully resolved flow and pressure fields and a collision model with a built-in evaporation process.

6.4.1. Description of the Simulation Setup

As mentioned above, the primary goal of the presented simulation is to see if such kind of simple approach can aid in the determination of the size distribution which is emitted by a commercially available ESI source. Thus, the experimental effort needs to be minimized to make it as simple as possible. This resulted in a setup (cf. fig. 6.16) in which an ESI emitter (blue) is placed between two plate electrodes (red and green). The
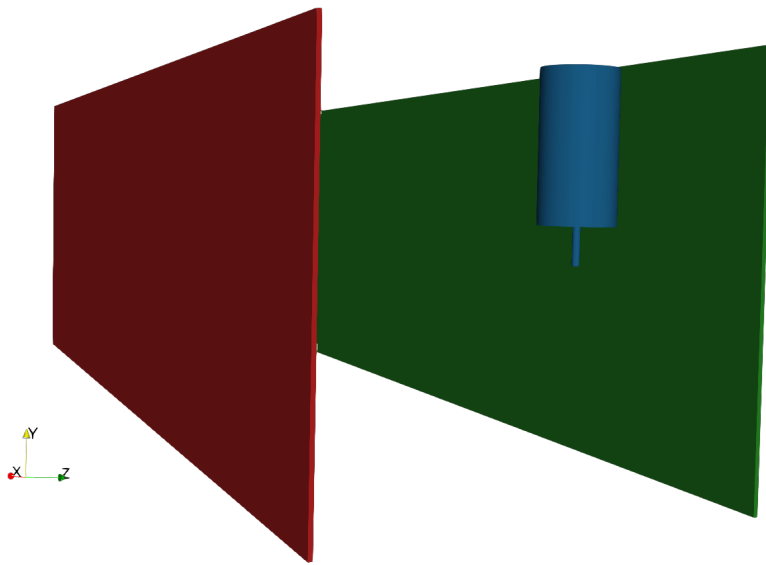
Figure 6.16.: Basic model of a simplified ESI chamber. In blue the ESI emitter with attached ESI needle. In green the ground electrode and in red the counter electrode. The neutral gas flow is in x direction. The simulated droplets are introduced into the simulation directly below the ESI needle.

green electrode and the ESI emitter are grounded, while a deflection voltage is applied to the counter electrode (red). The voltage is varied in multiple simulation runs between $-1\,\mathrm{kV}$ to $-5\,\mathrm{kV}$ with a step size of $1\,\mathrm{kV}$. The neutral gas flow direction is in the viewing direction of fig. 6.16 (x direction) and is uniformly introduced to this front boundary. For the ion trajectory simulations, the ions are introduced directly below the tip of the ESI emitter. Table 6.6 lists the droplet species selected for all subsequent simulations.

Table 6.6.: Droplet parameters at the Rayleigh Limit of the six selected species for the ESI chamber simulations.

Diameter [µm]	Mass [u]	Charges
5	3.94×10^{13}	4.98×10^{5}
10	3.15×10^{14}	1.41×10^{6}
25	4.92×10^{15}	5.57×10^{6}
50	3.94×10^{16}	1.57×10^{7}
75	1.33×10^{17}	2.89×10^{7}
100	3.15×10^{17}	4.46×10^{7}

6.4.2. Calculated Flow and Pressure Profiles

The neutral gas flow and the background pressure are calculated with OpenFOAM to create a more comprehensive picture of this simplified ESI source. The *SimpleFoam* solver is applied in this case, which is a steady-state solver for incompressible, turbulent flow using the SIMPLE algorithm. It is selected for multiple reasons: A steady-state solver is selected because it provides a static, time-independent flow field in the simulation domain when it successfully converges. The pressure in the simulation is at atmospheric level, and no large changes are expected within the simulated geometry. Therefore, there is no need for a compressible solver. The *SimpleFOAM* solver has support for diverse turbulence models, which is used to describe the change in flow around the ESI emitter as precise as possible without actual experimental flow parameters. In total, three different initial flow speeds are chosen: 1, 3, and $5\,\mathrm{m\,s^{-1}}$. The simulation parameters are listed in table 6.7.

All three simulation runs for the different initial velocities converged. In fig. 6.17 the flow and pressure profiles inside the simulated chamber are visualized. Significant effects on the flow and pressure profiles are observed around the ESI emitter, as expected. The
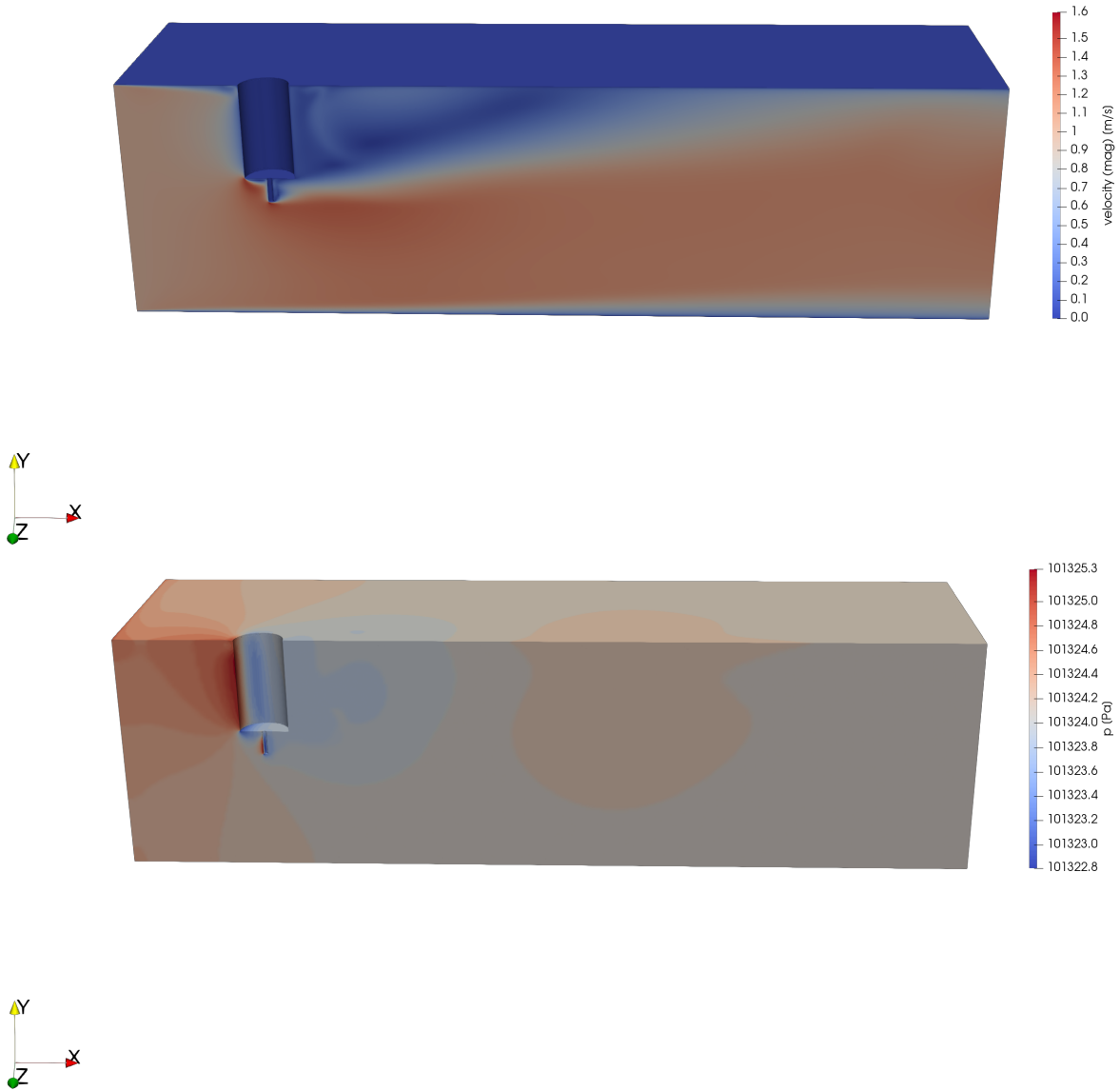
Figure 6.17.: Static (steady-state) flow (top) and pressure (bottom) profiles in the the
ESI chamber with an initial velocity of $1\,\mathrm{m\,s^{-1}}$.

Table 6.7.: OpenFOAM simulation parameters for the simplified ESI chamber.

Parameter	Value
Dimensions	3
Solver	SimpleFoam (steady-state)
Turbulence model	k-ϵ
Compressible gas	off
Gas mixture	Air
Input pressure [mbar]	1013.25
Input velocities [m/s]	1 and 3 and 5
OpenFOAM version	8

region directly below the ESI needle is the area of the highest interest, because the simulated charged droplets are introduced at this position in the subsequent trajectory simulations. As presented in more detail, the trajectories of the charged droplets are strongly influenced by the local flow field at this position. The different flow fields are named below according to their input velocity, e.g., flow field with $3\,\mathrm{m\,s^{-1}}$.

6.4.3. Converting the Obtained Flow Field

As in all previous simulations, the flow and pressure profiles needed to be converted into a format that can be used in the SIMION trajectory simulations. In all previously shown simulations the obtained profiles are translated to comparably simple analytical equations, which are then applied as input parameter to the collision models used in SIMION. In all these cases, the obtained profiles are applied with highest accuracy to some kind of axis, which matched the main trajectory of the ions, as shown for example in section 5.3.3, the axis matches the center axis through the PCB quadrupole or as in section 6.2.3 the ions traverse only in one direction with a narrow radial distribution. If radial profiles were applied, their starting point was always at the given main axis. In this case, no such behavior is expected, and therefore, the conditions for such simplification are no longer valid. The flow fields obtained from the OpenFOAM simulations thus need to be converted to a format that can be used in SIMION. The significant difference between the two simulation approaches is that OpenFOAM uses a mostly irregular grid, so that specific regions can be resolved with more precision. In contrast, SIMION uses a strictly structured, hexagonal, grid. The flow and pressure values are assigned to each

point on the calculation grid. Generally these two grids do not match; therefore, the values on the SIMION grid nodes must be interpolated from nearby grid points of the OpenFOAM grid. To achieve this, the Delaunay triangulation [94] is used. In three-dimensional space, it searches for a set of four points which form a tetrahedron in which there is no additional grid point in the surrounding sphere. Applying this method to all nodes on a grid, a minimal triangulation is obtained. With this triangulation, the unstructured grid from the OpenFOAM simulation can be translated into a regular grid for the SIMION simulation. A Python module was written, which was updated multiple times to fit these specific needs. In this module, the SciPy Delaunay module [18] is used.

The large number of cells and points on the OpenFOAM grid lead to unexpected problems. In this specific case, the OpenFOAM grid contains $7,102,214$ grid nodes, and this needed to be translated into a regular grid of $3,500,000$ individual points. The time-consuming and numerically demanding step is the calculation of the vertices and weights of the Delaunay triangulation. This calculation time of these vertices and weights took approx. 30 days on an AMD Opteron 6282 SE system (2.6 GHz, with a boost clock of 3.3 GHz). The main problem is currently no usable parallel version of the Delaunay triangulation publicly available. Therefore, it can be performed only in serial mode, which renders these calculations very time consuming with larger point cloud sets. As a minor optimization for this process, an export functionality for the vertices and weights is implemented. In this case, triangulation itself only needs to be performed once for a given OpenFOAM grid and must not be performed several times for the same grid with different overlying flow and pressure values. In the future, a means to speed up these kinds of calculation is required. The main challenge is that the domain cannot be easily split into smaller domains for multiprocess calculations, due to the flip algorithm employed. This leads to an overall run time of $\mathcal{O}(n^2)$. There are some faster algorithms for Delaunay triangulation, but only for the two-dimensional case [95] [96]. The last step is the conservation of the now regular grid fields into a SIMION potential array, which have a predefined structure. These can be produced with SIMION board utilities and then imported into the SIMION workbench.

6.4.4. Results

Influence of the Flow Field depending on Particle Size

The influence of the flow field on the simulated charged particles is investigated to verify whether the conversion of the flow field to SIMION potential array is correct. Therefore,

the positions at which the ions hit the electrode are recorded, expressed in x and y coordinates on the counter electrode. In the following table, the coordinates with regard to the neutral gas flow velocity are listed. For this purpose, the smallest droplet and the largest droplet (with diameters of 5 µm and 100 µm) species are chosen.

Table 6.8.: Impact coordinates on the counter electrode of the smallest and largest droplet of the used ion ensemble with standard deviation. The simulation contains 1000 ions per run and a voltage of $-5\,\mathrm{kV}$ is applied at the counter electrode.

Species		$1\,\mathrm{m\,s^{-1}}$	$3\,\mathrm{m\,s^{-1}}$	$5\,\mathrm{m\,s^{-1}}$
small	x [mm]	69 ± 2	73.7 ± 0.4	76 ± 2
	y [mm]	36.2 ± 0.4	36.5 ± 0.4	34 ± 1
large	x [mm]	60 ± 7	60 ± 6	60 ± 6
	y [mm]	4 ± 2	4 ± 2	4 ± 2

As listed in table 6.8, the impact position of the smallest droplets changes with variation in the flow of the neutral gas. On the contrary, there is almost no coupling between the larger droplet impact position and the neutral gas flow velocity. This behavior is as expected as it is much easier to change the trajectories of lighter species than it is for much heavier ones; in this case the smallest species is around 90 times lighter than the largest. In addition, there is a clear impact of the flow field on the lighter droplets: The x positions of the impact are moved to larger values with increasing background velocity in that direction. Thus, the converting process of the flow fields is successfully achieved.

Impact of the Applied Evaporation Model on the Droplet Species

Regardless which model is used for the description of the ESI process, the droplet radius decreases with time. So far, the evaporation of the droplets has been disregarded in the models applied. Therefore, an evaporation model is implemented into the SIMION SDS model (for further information, see section 3.6). As shown in fig. 6.18, the model changes the diameter and mass of the charged particles simulated, which are coupled to the SDS collision model.

The beginning of evaporation follows a more or less linear loss of mass and diameter. When the model approaches its endpoint, after which it is no longer valid to describe the loss of mass, the function is no longer linear. This iss be seen in fig. 6.18, where
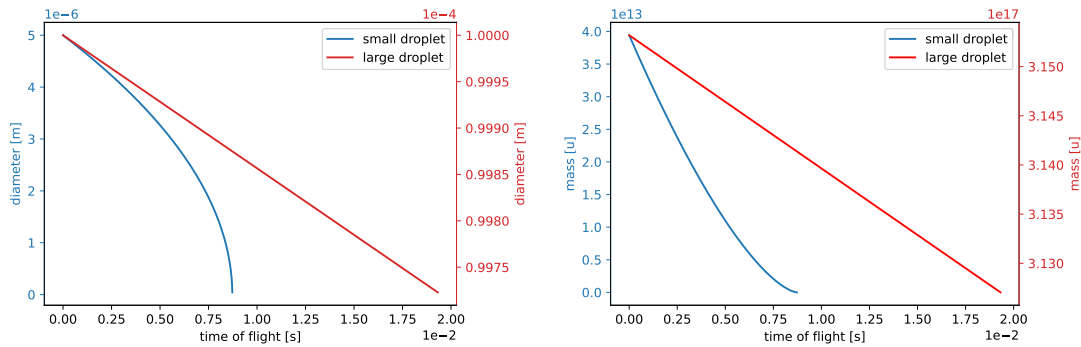
Figure 6.18.: Change of droplets diameter (left) and mass (right) with the time of flight. The small droplet (blue) has an initial diameter of 5 µm and the large (red) 100 µm.

during flight time the mass and diameter functions of the larger droplet are nearly linear, whereas the graphs of the smaller droplet clearly show a non-linear behavior with longer flight time. In addition, the larger droplets need significantly more time to hit the counter electrode, because of their higher mass and diameter. These observations are expected and thus the implemented evaporation process is working.

Spatial Separation of the Different Droplet Sizes

If not noted otherwise, all subsequent simulations are performed with enabled evaporation model. As mentioned above, the main idea is that different droplets hit different regions at the counter electrode. In a hypothetical experimental setup, the counter electrode could be divided into different regions, and the current of the ions terminating at the electrode could be detected spatially resolved.

As shown in fig. 6.19, the two lighter droplets hit the electrode at larger y values. On the contrary, the four larger droplet species are not spatially separated. It is noticeable that with higher masses, the size of the impact area increases. This could result from the longer flight times and therefore the increased diffusion of these larger droplets. They experience significantly more collisions on the way towards the counter electrode and therefore may repeatedly change their flight direction. For the three larger droplets (diameters: 50, 75 and 100 µm), the impact space is cut at a y value of zero. They do not hit the electrode and left the simulated domain through the bottom of the chamber. The shift in the x direction is much smaller than in the y direction.
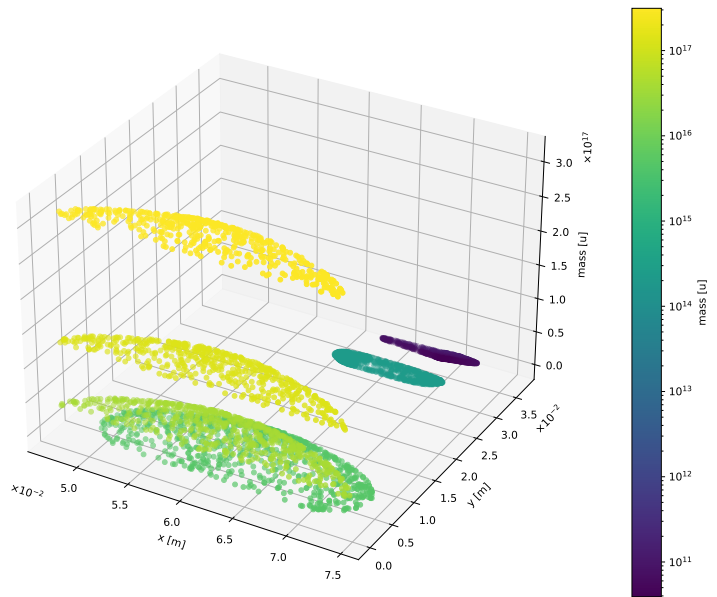
Figure 6.19.: Droplet termination positions on the counter electrode; the dots indicate the x and y position of the impact. On the y axis and by the color the mass of the droplet is indicated. The neutral initial gas velocity is $1\,\mathrm{m\,s^{-1}}$ and a DC voltage of $-5\,\mathrm{kV}$ is applied. The two lighter droplet species, with a diameter of $5\,\mu\mathrm{m}$ to $10\,\mu\mathrm{m}$ are spatially separated from the other groups, whereas the four other overlap.
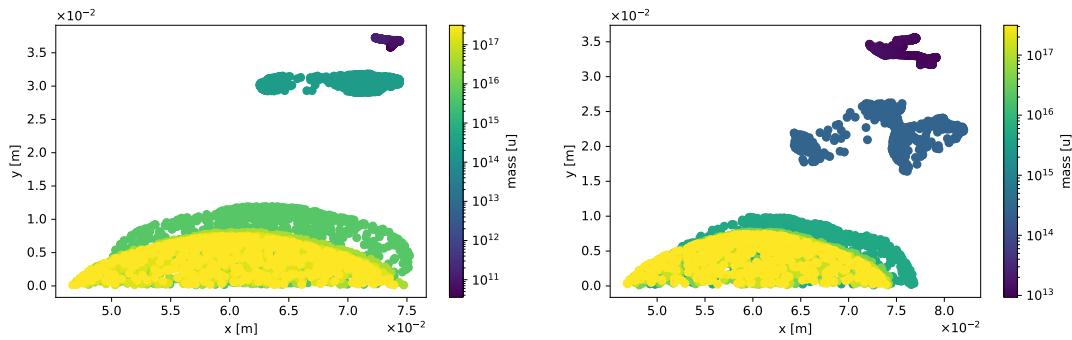
Figure 6.20.: Droplet termination positions on the counter electrode: The dots indicate the x and y position where droplets hits the counter electrode. The color represents the mass of the droplets. The left side has an initial neutral gas velocity of 3 and the right of $5\,\mathrm{m\,s^{-1}}$. In both cases a DC voltage of $-5\,\mathrm{kV}$ is applied.

If the two highest neutral gas velocities are compared (cf. fig. 6.20), it becomes apparent that the overall mass loss of the droplet species is greater, which is most obvious for the smallest droplet species. This is because the small droplets are more influenced by the higher background gas velocity in the x direction and therefore have a longer travel distance and flight time. This notion is also indicated by the higher observed x values. Compared to the background velocity of $1\,\mathrm{m\,s^{-1}}$ (cf. fig. 6.19), the impact distribution becomes initially narrower (cf. fig. 6.20 left) and then becomes broader and more asymmetric (cf. fig. 6.20 right).
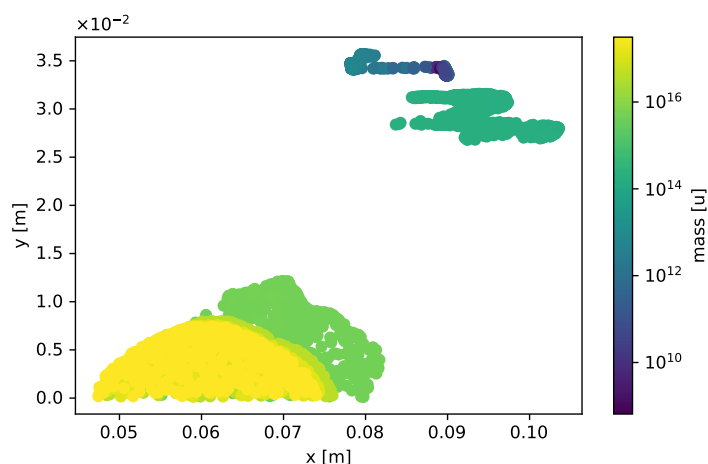
Figure 6.21.: Droplet termination position on the counter electrode: The dots indicate the x and y position where a droplet hits the counter electrode. The color represents the mass of the droplets. The initial neutral gas velocity is $5\,\mathrm{m\,s^{-1}}$ and a DC voltage of $-1\,\mathrm{kV}$ is applied.

The same behavior is seen in the comparison of fig. 6.20 (right) and fig. 6.21. In both cases an initial neutral gas velocity of $5\,\mathrm{m\,s^{-1}}$ is applied, but here voltage is reduced to $-1\,\mathrm{kV}$ between the two electrodes. With a smaller electric field gradient, the time of flight becomes longer and lighter droplets are more influenced by the neutral gas flow. For example, the $10\,\mathrm{\mu m}$ droplet species is shifting about $20\,\mathrm{mm}$ towards higher x values.

6.4.5. Summary

It is shown that with this particular setup, only the lighter droplets could be spatially resolved. The distance between the electrode and the counter electrode needs to be increased to obtain better resolution. But even then, a spatial resolution of the largest droplet species considered is very unlikely. Nevertheless, the proposed experiment may be used to describe the ratio between smaller and larger droplets. If the counter electrode is divided in the y direction, for example in two or even three sections, the ratio between small droplets or analyte ions and larger aggregates could be determined. An increase in the neutral gas flow leads to a larger separation in the x direction, but also increases the broadening in the impact zone. The x resolution is even worse than in the y direction. Therefore, an increase in neutral gas flow is not promising.

Even though the separation of the droplets with this setup is not optimal, it is shown that the simulation of ion trajectories worked well. The conversation of the OpenFOAM flow and pressure fields is still numerically demanding, but is basically working. For smaller systems, or even two-dimensional cases, the computing time is much shorter than for the model presented here. Larger or more complex systems are not recommended without employing a more effective triangulation method. The evaporation model works as expected, and with the coupling to the SDS collision model, the new mass and diameter of the droplets is updated every time step. This opens the way to the calculation of more realistic trajectories. It is stressed though that experimental data are needed to validate this enetire approach.

6.5. Conclusion and Outlook

In the first section of chapter 6, some special edge cases with regard to induced current calculations of droplets are described. In a simplified simulation setup, no cancelation of produced ion current transients due to the following droplets is oberved. In addition, it was shown that with the addition of two additional electrodes the existing setup can be used to perform induced current measurement. In combination with simulations such as those discussed in section 6.2, this approach can be used to determine droplet size distributions in an environment similar to the first vacuum stage of a commercially available mass spectrometer. If results of e.g. the laser scattering experiments are included, a detailed description of the droplet system should be reachable. In addition, a further electrode can be introduced to determine the velocity of a droplet, so a direct determination of the droplet charge becomes possible. The simulations suggest that with existing hardware, such as the oscilloscope in combination with a common sensitive amplifier, it is possible to detect droplets with approx. $10\,000$ charges.

In section 6.3 it is shown that ion current detection are also possible much further downstream in the Bruker HCTplus instrument. According to some previous work, there is space left to place a detection electrode in the actual instrument. Even if the results shown here are intended to serve as a first proof-of-principles calculation, the statement is still relevant. If experimental data become available, this simulation model may be helpful for data interpretation.

Finally, in section 6.4 it is demonstrated that it is not possible to fully spatially resolve the wide range of droplet sizes present in an ESI source with the employed minimal setup. However, some species were separated. More importantly, it is shown

that the integration of different programs and models can be combined into one trajectory simulation. There are still some difficulties that need to be overcome, such as the transformation of simulation grids from OpenFOAM to SIMION. In the end this also worked well, but is inefficient and time consuming for large simulation grids. In addition, the evaporation model is successfully integrated into the SDS collision model and works as expected.

In summary, the presented models are in an early and simplified state and should thus be further expanded. Depending on the comparison between simulation and experiment, the simulation models can be adapted and improved by further extensions. The goal is to model a commercially available ESI source, as for example the Apollo AP-ESI source from Bruker. Then, a more accurate description of the droplet ensemble at the entrance of MS systems could be provided. Furthermore, it would be important to determine which droplet sizes can penetrate such an MS system at all.

7. Final Conclusion and Outlook

To summarize this work, the following section is divided into three parts. First, the focus is on the technical part, which deals with the combination of different simulation approaches and combining them to a more comprehensive description of the physical system. In the second part, a conclusion is given on the three results chapter. Finally, a short outlook is given based on the work presented.

1) Three different simulation programs/frameworks were used in this work: Open-FOAM and SPARTA to model neutral gas flows in different pressure regimes. As long as the continuum approach is valid, OpenFOAM was used and in the more rarefied regimes SPARTA was employed. For the ion trajectory calculations, SIMION and SPARTA were used. Since SIMION cannot calculate neutral gas flow and pressure profiles, the results had to be always imported from one of the other programs. Because the ions mostly moved in rather linear trajectories, these flow and pressure profiles were mostly be represented by analytical functions. These are used as input parameters for a SIMION user program. When this assumption was no longer valid, the fully spatially resolved three-dimensional flow fields from OpenFOAM were successfully converted into SIMION potential arrays. In addition to the profiles, SPARTA was extended with the possibility to model acceleration by an external electric field force. It was shown that the algorithm implemented agrees with the analytical solution. Additionally, an analytical equation for the evaporation of droplets under atmospheric conditions was successfully implemented into the SIMION SDS collision model. The change in droplet mass and therefore droplet diameter as a result of evaporation directly influences the SDS collision model. It was further shown that the combination of the evaporation model with the collision model works. Due to the lack of experimental results, this model was not verified.

2) To summarize the results obtained, the determination of reduced ion mobilities with SPARTA is addressed. As mentioned above, the implementation of the electric force works in principle. Upon addition of a background gas, the ions experience an acceleration period followed by a steady-state drift velocity, as expected. For O_2^+ ions in N_2 background gas, the obtained values for the reduced mobilities are on the same order of magnitude as the experimental values, but almost a factor of two too high.

It was shown that the simulation boundaries are not stable over simulation time, as a compression wave induced by the ions was observed. However, the effect of the unstable conditions of the ion mobility calculations is negligible. Two additional pairs of ions and background gas are investigated under the variation of applied reduced field strengths. Even if the gap between the literature and the calculated values decreases with increasing reduced field strength, the obtained values are still too high. Knowing that the acceleration by the electric field is correct, it is most likely that the collision model causes these problems, but the final reason was not identified.

Proceeding with the modeling of a transfer stage between a HiKE-IMS and a TOF-MS, it was shown that it is possible to determine the effects of the transfer parameter on the transferred ions with respect to transmission efficiency and energy gained. For this case, a two- and three-dimensional model of the transfer was created and compared. It was shown that depending on the sampled region, the obtained results are either very similar or deviate. Luckily, the differences between the two- and three-dimensional models were small in the center of the modeled quadrupole, which is the region of interest. With subsequent ion trajectory calculations, it was illustrated that the ions experience most collisions at the entrance of the quadrupole, where the local pressure is still high and therefore gain the highest internal energy in this region.

In the last section, the focus was on the determination of the droplet size distribution, which is generated by electrospray ionization sources. For this purpose, the detection of induced current transient was chosen. Initially, it was demonstrated that no cancelation of the induced current signal due to the following droplets occurs. On the basis of the experimentally available hardware, it was shown that approximately 10 000 charges are detectable. On the basis of a Bruker HTCplus mass spectrometer, two different regions were more or less precisely modeled and extended by the possibility of detecting induced currents. These simulations should be considered as proof-of-principles calculations, which show that these experiments are feasible. Additionally, these models can be helpful in interpreting experimental results as soon as they become available. Finally, a rudimentary ESI source was designed, primarily to define a test case for the most comprehensive simulation in this work, which included an evaporation model and with fully spatially resolved neutral gas flow fields. However, it was shown that this setup is not capable of fully separating the wide spectrum of introduced droplets, but a ratio between smaller and larger droplets was successfully calculated.

3) Moving on to the outlook, the last chapter of this work is the part with the largest potential. After modeling the simplified ESI source, the next step is to design a com-

mercially available ESI source, as for example the Apollo AP-ESI source from Bruker. This should allow a more comprehensive description of the droplet ensemble in the ion source. Furthermore, it would be important to determine which droplet sizes can actually penetrate the MS vacuum system. Additionally, it is of major interest to outline the effect of the ESI spray parameters on the droplet size distribution and whether that can be simulated. As always, it is important to compare the computed results with experimentally determined data for validation purposes. On the technical side, it is important to speed up conversion of three-dimensional flow fields from OpenFOAM or SPARTA to SIMION, with a more efficient triangulation method.

List of Figures

List of Tables

References

[1] *SPARTA direct simulation monte carlo (DSMC) simulator*, SPARTA, (2023) http://sparta.sandia.gov (visited on 09/21/2023).

[2] G. A. Bird, "Approach to translational equilibrium in a rigid sphere gas", Physics of Fluids **6**, 1518 (1963) DOI: 10.1063/1.1710976.

[3] M. Fang, Z.-H. Li, Z.-H. Li, J. Liang, and Y.-H. Zhang, "DSMC modeling of rarefied ionization reactions and applications to hypervelocity spacecraft reentry flows", Advances in Aerodynamics **2**, 7 (2020) DOI: 10.1186/s42774-020-00030-1.

[4] M. A. Gallis, T. P. Koehler, J. R. Torczynski, and S. J. Plimpton, "Direct simulation monte carlo investigation of the rayleigh-taylor instability", Physical Review Fluids **1**, 043403 (2016) DOI: 10.1103/PhysRevFluids.1.043403.

[5] G. A. Bird, "Definition of mean free path for real gases", The Physics of Fluids **26**, 3222–3223 (1983) DOI: 10.1063/1.864095.

[6] K. Koura and H. Matsumoto, "Variable soft sphere molecular model for inverse-power-law or lennard-jones potential", Physics of Fluids A: Fluid Dynamics **3**, 2459–2465 (1991) DOI: 10.1063/1.858184.

[7] W. Morokoff and A. Kersch, "A comparison of scattering angle models", Computers & Mathematics with Applications **35**, 155–164 (1998) DOI: 10.1016/S0898-1221(97)00265-4.

[8] U. Ayachit, *The ParaView guide: updated for ParaView version 4.3*, edited by L. Avila, in collab. with B. Geveci, Full color version (Kitware Inc, Clifton Park, NY, 2015), ISBN: 978-1-930934-30-6.

[9] C. Sullivan and A. Kaszynski, "PyVista: 3d plotting and mesh analysis through a streamlined interface for the visualization toolkit (VTK)", Journal of Open Source Software **4**, 1450 (2019) DOI: 10.21105/joss.01450.

[10] C. Greenshields, *OpenFOAM v8 user guide* (The OpenFOAM Foundation, London, UK, 2020), https://doc.cfd.direct/openfoam/user-guide-v8.

References

[11] C. J. Greenshields and H. G. Weller, *Notes on computational fluid dynamics: general principles* (CFD Direct Limited, Reading, UK, 2022), ISBN: 978-1-399-92078-0.

[12] D. Manura, *User manual SIMION 8.1* (2005).

[13] R. Ierusalimschy, *Programming in Lua: 5.3 edition* (Roberto Ierusalimschy, Apr. 26, 2016), ISBN: 978-85-903798-6-7.

[14] G. Van Rossum and F. L. Drake, *Python 3 reference manual* (CreateSpace, Scotts Valley, CA, 2009), ISBN: 978-1441412690.

[15] C. R. Harris, K. J. Millman, S. J. Van Der Walt, R. Gommers, P. Virtanen, D. Cournapeau, E. Wieser, J. Taylor, S. Berg, N. J. Smith, R. Kern, M. Picus, S. Hoyer, M. H. Van Kerkwijk, M. Brett, A. Haldane, J. F. Del Río, M. Wiebe, P. Peterson, P. Gérard-Marchant, K. Sheppard, T. Reddy, W. Weckesser, H. Abbasi, C. Gohlke, and T. E. Oliphant, "Array programming with NumPy", Nature **585**, 357–362 (2020) DOI: 10.1038/s41586-020-2649-2.

[16] W. McKinney, "Data structures for statistical computing in python", in (2010), pp. 56–61, DOI: 10.25080/Majora-92bf1922-00a.

[17] T. P. D. Team, *Pandas-dev/pandas: pandas*, version v2.1.1, Sept. 20, 2023, DOI: 10.5281/ZENODO.3509134.

[18] P. Virtanen, R. Gommers, T. E. Oliphant, M. Haberland, T. Reddy, D. Cournapeau, E. Burovski, P. Peterson, W. Weckesser, J. Bright, S. J. van der Walt, M. Brett, J. Wilson, K. J. Millman, N. Mayorov, A. R. J. Nelson, E. Jones, R. Kern, E. Larson, C. J. Carey, İ. Polat, Y. Feng, E. W. Moore, J. VanderPlas, D. Laxalde, J. Perktold, R. Cimrman, I. Henriksen, E. A. Quintero, C. R. Harris, A. M. Archibald, A. H. Ribeiro, F. Pedregosa, and P. van Mulbregt, "SciPy 1.0: fundamental algorithms for scientific computing in python", Nature Methods **17**, 261–272 (2020) DOI: 10.1038/s41592-019-0686-2.

[19] J. D. Hunter, "Matplotlib: a 2d graphics environment", Computing in Science & Engineering **9**, 90–95 (2007) DOI: 10.1109/MCSE.2007.55.

[20] G. A. Bird, *Molecular gas dynamics and the direct simulation of gas flows*, Oxford engineering science series 42 (Clarendon Press ; Oxford University Press, Oxford : New York, 1994), ISBN: 978-0-19-856195-8.

[21]   G. A. Bird, *The DSMC method*, Version 1.2, 2013 (CreateSpace Independent
       Publishing Platform, North Charleston, South Carolina, 2013), ISBN:
       978-1-4921-1290-7.

[22]   I. D. Boyd and T. E. Schwartzentruber, *Nonequilibrium gas dynamics and
       molecular simulation*, 1st ed. (Cambridge University Press, Jan. 1, 2017), DOI:
       10.1017/9781139683494.

[23]   W. Wagner, "A convergence proof for bird's direct simulation monte carlo
       method for the boltzmann equation", Journal of Statistical Physics **66**,
       1011–1044 (1992) DOI: 10.1007/BF01055714.

[24]   C. Zhang and T. E. Schwartzentruber, "Robust cut-cell algorithms for DSMC
       implementations employing multi-level cartesian grids", Computers & Fluids **69**,
       122–135 (2012) DOI: 10.1016/j.compfluid.2012.08.013.

[25]   J. H. Ferziger, M. Perić, and R. L. Street, *Computational methods for fluid
       dynamics*, Fourth edition (Springer, Cham, 2020), ISBN: 978-3-319-99693-6.

[26]   C. Pozrikidis, *Fluid dynamics: theory, computation, and numerical simulation*,
       3rd ed. 2017 (Springer US : Imprint: Springer, New York, NY, 2017), DOI:
       10.1007/978-1-4899-7991-9.

[27]   R. L. Panton, *Incompressible flow*, Fourth edition (John Wiley and Sons, Inc,
       Hoboken, New Jersey, 2013), ISBN: 978-1-118-41573-3.

[28]   G. K. Batchelor, *An introduction to fluid dynamics*, 14. print, Cambridge
       mathematical library (Cambridge Univ. Press, Cambridge, 2010), ISBN:
       978-0-521-66396-0.

[29]   R. B. Bird and J. M. Wiest, "Constitutive equations for polymeric liquids",
       Annual Review of Fluid Mechanics **27**, 169–193 (1995) DOI:
       10.1146/annurev.fl.27.010195.001125.

[30]   F. Irgens, *Continuum mechanics* (Springer, Berlin, 2008), ISBN:
       978-3-540-74298-2.

[31]   Y. Saad, *Iterative methods for sparse linear systems*, 2nd Edition (SIAM,
       Philadelphia, 2003), ISBN: 978-0-89871-534-7.

[32]   J. Qin, Y. Chen, and X. Deng, "On the role of global conservation property for
       finite difference schemes", Journal of Computational Physics **440**, 110437 (2021)
       DOI: 10.1016/j.jcp.2021.110437.

References

[33] R. Eymard, T. Gallouët, and R. Herbin, "Finite volume methods", in *Handbook of numerical analysis*, Vol. 7 (Elsevier, 2000), pp. 713–1018, DOI: 10.1016/S1570-8659(00)07005-8.

[34] H. K. Versteeg and W. Malalasekera, *An introduction to computational fluid dynamics: the finite volume method*, 2nd Edition (Pearson Education Ltd, Harlow, England ; New York, 2007), ISBN: 978-0-13-127498-3.

[35] O. C. Zienkiewicz and R. L. Taylor, *The finite element method*, 5th Edition (Butterworth-Heinemann, Oxford ; Boston, 2000), ISBN: 978-0-7506-5049-6.

[36] C. Pozrikidis, *Introduction to finite and spectral element methods using MATLAB* (Chapman and Hall/CRC, June 20, 2014), DOI: 10.1201/b17067.

[37] I. D. Boyd, G. Chen, and G. V. Candler, "Predicting failure of the continuum fluid equations in transitional hypersonic flows", Physics of Fluids **7**, 210–219 (1995) DOI: 10.1063/1.868720.

[38] G. Karniadakis, A. Beşkök, and N. R. Aluru, *Microflows and nanoflows: fundamentals and simulation*, Interdisciplinary applied mathematics v. 29 (Springer, New York, NY, 2005), ISBN: 978-0-387-22197-7.

[39] Adaptas Solutions LLC., *SIMION 2020 supplemental documentation* (2020), https://simion.com/info.

[40] L. Ding, M. Sudakov, and S. Kumashiro, "A simulation study of the digital ion trap mass spectrometer", International Journal of Mass Spectrometry **221**, 117–138 (2002) DOI: 10.1016/S1387-3806(02)00921-1.

[41] A. D. Appelhans and D. A. Dahl, "SIMION ion optics simulations at atmospheric pressure", International Journal of Mass Spectrometry **244**, 1–14 (2005) DOI: 10.1016/j.ijms.2005.03.010.

[42] E. J. Davis, "Microchemical engineering: the physics and chemistry of the microparticle", in *Advances in chemical engineering*, Vol. 18 (Elsevier, 1992), pp. 1–94, DOI: 10.1016/S0065-2377(08)60122-2.

[43] James N. Smith, Richard C. Flagan, and J. L. Beauchamp, "Droplet evaporation and discharge dynamics in electrospray ionization [†]", The Journal of Physical Chemistry A **106**, 9957–9967 (2002) DOI: 10.1021/jp025723e.

[44] C. F. Curtiss and J. O. Hirschfelder, "Transport properties of multicomponent gas mixtures", The Journal of Chemical Physics **17**, 550–555 (1949) DOI: 10.1063/1.1747319.

[45] W. C. Röntgen, "On a new kind of rays", Science **3**, 227–231 (1896) DOI: 10.1126/science.3.59.227.

[46] Paul Langevin, "Une formule fondamentale de theorie cinetique", Ann. Chem. Phys. **5**, 245 (1905).

[47] H. Borsdorf and G. A. Eiceman, "Ion mobility spectrometry: principles and applications", Applied Spectroscopy Reviews **41**, 323–375 (2006) DOI: 10.1080/05704920600663469.

[48] M. J. Cohen and F. W. Karasek, "Plasma chromatography –a new dimension for gas chromatography and mass spectrometry", Journal of Chromatographic Science **8**, 330–337 (1970) DOI: 10.1093/chromsci/8.6.330.

[49] G. A. Eiceman, A. P. Snyder, and D. A. Blyth, "Monitoring of airborne organic vapors using ion mobility spectrometry", International Journal of Environmental Analytical Chemistry **38**, 415–425 (1990) DOI: 10.1080/03067319008026945.

[50] G. Eiceman and Z. Karpas, *Ion mobility spectrometry* (CRC Press, June 23, 2005), DOI: 10.1201/9781420038972.

[51] A. B. Kanu, P. Dwivedi, M. Tam, L. Matz, and H. H. Hill Jr., "Ion mobility–mass spectrometry", Journal of Mass Spectrometry **43**, 1–22 (2008) DOI: 10.1002/jms.1383.

[52] M. Allers, A. T. Kirk, N. von Roßbitzky, D. Erdogdu, R. Hillen, W. Wissdorf, T. Benter, and S. Zimmermann, "Analyzing positive reactant ions in high kinetic energy ion mobility spectrometry (HiKE-IMS) by HiKE-IMS–MS", Journal of the American Society for Mass Spectrometry **31**, 812–821 (2020) DOI: 10.1021/jasms.9b00087.

[53] M. Allers, A. T. Kirk, C. Schaefer, D. Erdogdu, W. Wissdorf, T. Benter, and S. Zimmermann, "Field-dependent reduced ion mobilities of positive and negative ions in air and nitrogen in high kinetic energy ion mobility spectrometry (HiKE-IMS)", Journal of the American Society for Mass Spectrometry **31**, 2191–2201 (2020) DOI: 10.1021/jasms.0c00280.

[54] E. A. Mason and E. W. McDaniel, *Transport properties of ions in gases* (Wiley, New York, 1988), ISBN: 978-0-471-88385-2.

[55] L. A. Viehland, *Gaseous ion mobility, diffusion, and reaction*, Vol. 105, Springer Series on Atomic, Optical, and Plasma Physics (Springer International Publishing, Cham, 2018), DOI: 10.1007/978-3-030-04494-7.

References

[56] S. J. Plimpton, S. G. Moore, A. Borner, A. K. Stagg, T. P. Koehler, J. R. Torczynski, and M. A. Gallis, "Direct simulation monte carlo on petaflop supercomputers and beyond", Physics of Fluids **31**, 086101 (2019) DOI: 10.1063/1.5108534.

[57] L. S. Avila, ed., *The VTK user's guide: install, use and extend the visualization toolkit ; covers installation on PC, unix, and mac OSX, includes example scripts, c source code, images and data, shows how to extend VTK for your own applications*, 11. Edition (Kitware, Clifton Park, NY, 2010), ISBN: 978-1-930934-23-8.

[58] Kitware Inc, *Online documentation of the paraview package*, (2013) https://kitware.github.io/paraview-docs/latest/python/paraview.simple.PlotOverLine.html (visited on 07/18/2022).

[59] L. A. Viehland and E. A. Mason, "Transport properties of gaseous ions over a wide energy range, IV", Atomic Data and Nuclear Data Tables **60**, 37–95 (1995) DOI: 10.1006/adnd.1995.1004.

[60] E. Y.-K. Ng and N. Liu, "The impacts of time-step size in the application of the direct simulation monte carlo method to ultra-thin gas film lubrication", Journal of Micromechanics and Microengineering **12**, 567–573 (2002) DOI: 10.1088/0960-1317/12/5/309.

[61] Wißdorf, Walter, D. Erdogdu, M. Thinius, and T. Benter, "Ion Dynamics Simulation Framework (IDSimF)", in ASMS (2020).

[62] M. Rajkovic, W. Wißdorf, H. Kersten, and T. Benter, "Implementation of a molecular dynamics collision model for determination of ion mobilities in the ion dynamics simulation framework (IDSimF)", in IMSC (2022).

[63] C. Markert, "Investigation of charged droplets aspirated in the electrospray ionization process", Publisher: Bergische Universität Wuppertal, PhD thesis (Wuppertal, 2023), DOI: 10.25926/BUW/0-104.

[64] M. Dole, L. L. Mack, R. L. Hines, R. C. Mobley, L. D. Ferguson, and M. B. Alice, "Molecular beams of macroions", The Journal of Chemical Physics **49**, 2240–2249 (1968) DOI: 10.1063/1.1670391.

[65] M. Yamashita and J. B. Fenn, "Electrospray ion source. another variation on the free-jet theme", The Journal of Physical Chemistry **88**, 4451–4459 (1984) DOI: 10.1021/j150664a002.

[66] C. M. Whitehouse, R. N. Dreyer, M. Yamashita, and J. B. Fenn, "Electrospray interface for liquid chromatographs and mass spectrometers", Analytical Chemistry **57**, 675–679 (1985) DOI: 10.1021/ac00280a023.

[67] T. R. Covey, B. A. Thomson, and B. B. Schneider, "Atmospheric pressure ion sources", Mass Spectrometry Reviews **28**, 870–897 (2009) DOI: 10.1002/mas.20246.

[68] C. Afonso, R. B. Cole, and J.-C. Tabet, "Dissociation of even-electron ions", in *Electrospray and MALDI mass spectrometry*, edited by R. B. Cole (John Wiley & Sons, Inc., Hoboken, NJ, USA, Nov. 27, 2012), pp. 631–682, DOI: 10.1002/9780470588901.ch17.

[69] E. d. Hoffmann and V. Stroobant, *Mass spectrometry: principles and applications*, 3rd Edition (J. Wiley, Chichester, West Sussex, England ; Hoboken, NJ, 2007), ISBN: 978-0-470-03310-4.

[70] P. Kebarle and U. H. Verkerk, "Electrospray: from ions in solution to ions in the gas phase, what we know now", Mass Spectrometry Reviews **28**, 898–917 (2009) DOI: 10.1002/mas.20247.

[71] L. Rayleigh, "XX. on the equilibrium of liquid conducting masses charged with electricity", The London, Edinburgh, and Dublin Philosophical Magazine and Journal of Science **14**, 184–186 (1882) DOI: 10.1080/14786448208628425.

[72] G. I. Taylor and A. D. McEwan, "The stability of a horizontal fluid interface in a vertical electric field", Journal of Fluid Mechanics **22** (1965), https://doi.org/10.1017/S0022112065000538.

[73] J. Fernandez de la Mora, "Electrospray ionization of large multiply charged species proceeds via dole's charged residue mechanism", Analytica Chimica Acta **406**, 93–104 (2000) DOI: 10.1016/S0003-2670(99)00601-7.

[74] M. Cloupeau and B. Prunet-Foch, "Electrohydrodynamic spraying functioning modes: a critical review", Journal of Aerosol Science **25**, 1021–1036 (1994) DOI: 10.1016/0021-8502(94)90199-6.

[75] M. Cloupeau, "Recipes for use of EHD spraying in cone-jet mode and notes on corona discharge effects", Journal of Aerosol Science **25**, 1143–1157 (1994) DOI: 10.1016/0021-8502(94)90206-2.

References

[76] K. Tang and A. Gomez, "Generation by electrospray of monodisperse water droplets for targeted drug delivery by inhalation", Journal of Aerosol Science **25**, 1237–1249 (1994) DOI: 10.1016/0021-8502(94)90212-7.

[77] C. Markert, M. Thinius, L. Lehmann, C. Heintz, F. Stappert, W. Wissdorf, H. Kersten, T. Benter, B. B. Schneider, and T. R. Covey, "Observation of charged droplets from electrospray ionization (ESI) plumes in API mass spectrometers", Analytical and Bioanalytical Chemistry (2021), https://doi.org/10.1007/s00216-021-03452-y.

[78] R. L. Grimm and J. L. Beauchamp, "Evaporation and discharge dynamics of highly charged multicomponent droplets generated by electrospray ionization", The Journal of Physical Chemistry A **114**, 1411–1419 (2010) DOI: 10.1021/jp907162w.

[79] A. Gomez and K. Tang, "Charge and fission of droplets in electrostatic sprays", Physics of Fluids **6**, 404–414 (1994) DOI: 10.1063/1.868037.

[80] M. A. Abbas and J. Latham, "The instability of evaporating charged drops", Journal of Fluid Mechanics **30**, 663–670 (1967) DOI: 10.1017/S0022112067001685.

[81] J. W. Schweizer and D. Hanson, "Stability limit of charged drops", Journal of Colloid and Interface Science **35**, 417–423 (1971) DOI: 10.1016/0021-9797(71)90141-X.

[82] D. C. Taflin, T. L. Ward, and E. J. Davis, "Electrified droplet fission and the rayleigh limit", Langmuir **5**, 376–384 (1989) DOI: 10.1021/la00086a016.

[83] E. Davis and M. Bridges, "The rayleigh limit of charge revisited: light scattering from exploding droplets", Journal of Aerosol Science **25**, 1179–1199 (1994) DOI: 10.1016/0021-8502(94)90208-9.

[84] X. Feng, M. J. Bogan, and G. R. Agnes, "Coulomb fission event resolved progeny droplet production from isolated evaporating methanol droplets", Analytical Chemistry **73**, 4499–4507 (2001) DOI: 10.1021/ac0101555.

[85] B. A. Thomson and J. V. Iribarne, "Field induced ion evaporation from liquid surfaces at atmospheric pressure", The Journal of Chemical Physics **71**, 4451–4463 (1979) DOI: 10.1063/1.438198.

[86] J. V. Iribarne and B. A. Thomson, "On the evaporation of small ions from charged droplets", The Journal of Chemical Physics **64**, 2287–2294 (1976) DOI: 10.1063/1.432536.

[87] L. Konermann, E. Ahadi, A. D. Rodriguez, and S. Vahidi, "Unraveling the mechanism of electrospray ionization", Analytical Chemistry **85**, 2–9 (2013) DOI: 10.1021/ac302789c.

[88] Y. Kang, B. B. Schneider, and T. R. Covey, "On the nature of mass spectrometer analyzer contamination", Journal of the American Society for Mass Spectrometry **28**, 2384–2392 (2017) DOI: 10.1007/s13361-017-1747-3.

[89] W.L. Hosch, *Electrostatic induction*, (Dec. 18, 2011) https://www.britannica.com/science/electrostatic-induction (visited on 11/01/2023).

[90] S. Ramo, "Currents induced by electron motion", Proceedings of the IRE **27**, Conference Name: Proceedings of the IRE, 584–585 (1939) DOI: 10.1109/JRPROC.1939.228757.

[91] W. Nonner, A. Peyser, D. Gillespie, and B. Eisenberg, "Relating microscopic charge movement to macroscopic currents: the ramo-shockley theorem applied to ion channels", Biophysical Journal, 7 DOI: 10.1529/biophysj.104.047548.

[92] H. Spieler, *Semiconductor detector systems*, Series on semiconductor science and technology 12 (Oxford University Press, Oxford ; New York, 2005), ISBN: 978-0-19-852784-8.

[93] M. Thinius, "Kinetic energy measurements for ion dynamics studies in API-MS and modeling of an FT-QIT", Publisher: Bergische Universität Wuppertal, PhD thesis (2021), DOI: 10.25926/0y06-7727.

[94] B. N. Delaunay, "Sur la sphère vide", Bulletin de l'Académie des Sciences de l'URSS **6**, 793–800 (1934).

[95] D. Sinclair, "S-hull: a fast radial sweep-hull routine for delaunay triangulation", (2016), https://doi.org/10.48550/arXiv.1604.01428.

[96] R. A. Dwyer, "A faster divide-and-conquer algorithm for constructing delaunay triangulations", Algorithmica **2**, 137–151 (1987) DOI: 10.1007/BF01840356.

A. Appendix A

The velocity and pressure profiles functions for SIMION simulations are listed below.

A.1. Profiles for Section 5.4

Pressure Profile

The pressure is expressed by the following function:

$$p(x_\mathrm{m}) = 2816.750 \cdot \exp\left(-1016.371 \cdot x_\mathrm{m}\right) - 3.105$$

With p as the pressure in Pascal and x_m as the x position in meter. Furthermore, a maximum p_max and minimum p_min pressure value was defined by a Lua function.

$$p_\mathrm{min} = 2.09$$
$$p_\mathrm{max} = 1371.29$$

Velocity Profiles

$$v_\mathrm{x}(x_\mathrm{m}) = \begin{cases} (256\,866.871 \cdot x_\mathrm{m} - 127.02) \cdot 0.001 & x_\mathrm{m} < 0.0031 \\ (2094.019 \cdot \exp\left(-419.947 \cdot x_\mathrm{m}\right) + 144.181) \cdot 0.001 & x_\mathrm{m} \geq 0.0031 \end{cases}$$

With v_x as the velocity in x direction and the $v_\mathrm{x,min}$ and $v_\mathrm{x,max}$ as the minimum and maximum values.

$$v_\mathrm{x,min} = 0.0546$$
$$v_\mathrm{x,max} = 0.6284$$

For the y and z directions first length of the combined $|\vec{l}_{y,z}|$ is calculated and then used as a normalization factor for the overall radial velocity v_{radial}:

$$v_{\text{radial}}(x_{\text{m}}) = \begin{cases} (0.103 \cdot \exp{(2535.359 \cdot x_{\text{m}})} - 3.627) \cdot 0.001 & x_{\text{m}} < 0.0025 \\ (318.453 \cdot \exp{(-756.404 \cdot x_{\text{m}})} + 0.706) \cdot 0.001 & x_{\text{m}} \geq 0.0025 \end{cases}$$

With a maximum value of $v_{\text{radial}} = 0.043$. Then the velocity for the y and z direction are determined:

$$v_{\text{y}}(x_{\text{m}}, y_{\text{m}}) = \frac{y_{\text{m}}}{|\vec{l}_{\text{y,z}}|} \cdot v_{\text{radial}}(x_{\text{m}})$$

$$v_{\text{z}}(x_{\text{m}}, z_{\text{m}}) = \frac{z_{\text{m}}}{|\vec{l}_{\text{y,z}}|} \cdot v_{\text{radial}}$$

With y_{m} and z_{m} as the y and z position in meter.

A.2. Profiles for Section 6.2

Pressure Profile

The pressure is expressed by the following function:

$$p(x_{\text{m}}) = \begin{cases} 1323.49 & x_{\text{m}} < 1.3 \times 10^{-3} \\ 14\,720.829 \cdot \exp{(-1844.581 \cdot x_{\text{m}})} & x_{\text{m}} \geq 1.3 \times 10^{-3} \end{cases}$$

Velocity Profiles

The velocity in x direction is:

$$v_{\text{x}}(x_{\text{m}}) = \begin{cases} 1152.2 & x_{\text{m}} \leq 1.3 \times 10^{-3} \\ -3.87 \times 10^{7} \cdot x_{m}^{2} + 2.95 \times 10^{5} \cdot x_{\text{m}} + 8.21 \times 10^{2} & 1.3 \times 10^{-3} < x_{\text{m}} \leq 4 \times 10^{-3} \\ 9605.911 \cdot x_{\text{m}} + 1375.302 & x_{\text{m}} > 4 \times 10^{-3} \end{cases}$$

The radial velocity profile is distinguished between to different distances between the main axis and the radial position of the particle. First, the function for particles near the main axis is shown ($|\vec{l}_{y,z}| \leq 3.5 \times 10^{-4}$):

$$
v_{\text{radial}}(x_{\text{m}}) = \begin{cases} 0.0 & x_{\text{m}} \leq 1.3 \times 10^{-3} \\ -2.19 \times 10^8 \cdot x_{\text{m}}^2 + 9.01 \times 10^5 \cdot x_{\text{m}} - 8.10 \times 10^2 & 1.3 \times 10^{-3} < x_{\text{m}} \leq 2 \times 10^{-3} \\ 197.476 \cdot x_{\text{m}} + \exp\left(-299.087 \cdot x_{\text{m}}\right) & x_{\text{m}} > 2 \times 10^{-3} \end{cases}
$$

Second, the radial velocity for $|\vec{l}_{y,z}| > 3.5 \times 10^{-4}$ is listed:

$$
v_{\text{radial}}(x_{\text{m}}) = \begin{cases} 1.34 \times 10^8 \cdot x_{\text{m}}^2 - 5.25 \times 10^5 \cdot x_{\text{m}} + 9.0 \times 10^2 & x_{\text{m}} \leq 2 \times 10^{-3} \\ 624.157 \cdot x_{\text{m}} + \exp\left(-280.790 \cdot x_{\text{m}}\right) & x_{\text{m}} > 2 \times 10^{-3} \end{cases}
$$

A.3. Profiles for Section 6.3

In this section, the x position unit is changed to mm and the pressure unit is changed to mbar.

Pressure Profile

The pressure is expressed by the following function:

$$
p(x_{\text{mm}}) = \begin{cases} -5.85 \times 10^{-4} \cdot (x + 15.383)^2 + 0.348 & x < 0.16 \\ 3.97 \times 10^{-3} \cdot \exp\left(\frac{32.729}{x^{1.159}}\right) + 8.330 & 0.16 \leq x < 7.57 \\ 2.42 \times 10^{-3} \cdot \exp\left(\frac{1.470}{x^{4.459}}\right) + 5.85 \times 10^4 & 7.57 \leq x < 39.67 \\ -4.53 \times 10^{-6} \cdot x + 2.71 \times 10^{-3} & 39.67 \leq x < 131.05 \\ 4.618 * 0.374^{x-123.0} & 131.05 \leq x < 136.16 \end{cases}
$$

The minimum value of the pressure is: $p_{\text{min}} = 1 \times 10^{-5}$.

Velocity Profiles

In this section the radial velocity is omitted. Some of the segments are modeled by two Gaussian functions. For better readability, first the Gaussian function are given:

$$g_1(x_{\mathrm{mm}}) = 138.468 \cdot \exp\left(-\frac{(x - 2.123)^2}{2 \cdot 3.020^2}\right)$$

$$g_2(x_{\mathrm{mm}}) = 83.547 \cdot \exp\left(-\frac{(x - 0.979)^2}{2 \cdot 1.182^2}\right)$$

$$g_3(x_{\mathrm{mm}}) = 88.160 \cdot \exp\left(-\frac{(x - 9.663)^2}{2 \cdot 12.409^2}\right)$$

$$g_4(x_{\mathrm{mm}}) = 37.475 \cdot \exp\left(-\frac{(x - 10.550)^2}{2 \cdot 1.308^2}\right)$$

Followed by the velocity in x direction:

$$v_{\mathrm{x}}(x_{\mathrm{mm}}) = \begin{cases} 3.485 \cdot x + 58.816 & x < -1.98 \\ g_1(x_{\mathrm{mm}}) + g_2(x_{\mathrm{mm}}) & -1.98 \leq x < 5.10 \\ g_3(x_{\mathrm{mm}}) + g_4(x_{\mathrm{mm}}) & 5.10 \leq y < 15.96 \\ 23.164 \cdot 0.954^{x-35.929} & 15.96 \leq x < 125.13 \\ 1.641 \times 10^{-10} \cdot 3.003^{x-106.052} & 125.13 \leq x < 132.25 \\ 369.488 \cdot 0.637^{x-133.138} & 132.25 \leq x < 137.00 \\ -5.559 \cdot x + 824049 & x \geq 137.0 \end{cases}$$

B. Appendix B

B.1. Evaporation Model

Listing B.1: standalone_eva.lua

```lua
1  simion.workbench_program()
2  -- Units in SIMION is mm and microsec
3  -- for math functions eg. pi, sqrt
4  require "math"
5  local EVA = {}
6  EVA.segment = {}
7
8  -- if _evaporation_record = 0 evaporation log is turned off, 1 means turned
      on
9  adjustable _evaporation_record = 1
10
11 -- parameters to calculate the evaporationrate
12 -- use SI-Units
13 -- output is in SI-Units
14 -- example for a Waterdroplet in dry N2 @317K and 101325 Pa
15 adjustable _droplet_start_diameter = 2.75e-5 -- [m]
16 adjustable _mol_weight_vapor = 0.018 -- [kg mol^-1]
17 adjustable _mol_weight_gas = 0.028 -- [kg mol^-1]
18 adjustable _pressure = 101325 -- [Pa]
19 adjustable _collision_diameter_droplet_species = 2.85e-10 -- [m]
20 adjustable _collision_diameter_gas_species = 3.75e-10 -- [m]
21 adjustable collions_intergral = 1 -- unitless, usually of order 1
22 adjustable _vapor_pressure =  7381.4 -- [Pa] H2O@313K at the droplet surfcae
      temp
23 adjustable _bulk_gas_temp = 317 -- [K]
24 adjustable _droplet_density = 993.18 -- [kg m^-3] @310.95K
25
26 -- Define constants
27 local R = 8.314462618 -- [J mol^-1 K^-1]
28 local kb = 1.380649e-23 -- [J K^-1] Boltzmann
29 local Na = 6.022e23 -- unitless, Avogadro
```

```
30
31  -- Properties:
32  -- diamter of particle/ion
33  -- maps ion_number to refer
34  local ion_diameter = {}
35
36  -- SIMION initialize_run segment. Called once before run
37  -- Calculates the specific reduction rate of the given
38  -- particle (see references)
39  function segment.initialize_run()
40      local sigma = (_collision_diameter_droplet_species +
            _collision_diameter_gas_species)/2
41      local binary_diffusivity = 3/8 * ((Na/math.pi * ((_mol_weight_gas +
            _mol_weight_vapor)/(2*_mol_weight_gas*_mol_weight_vapor)))^(0.5)) * (
            kb*_bulk_gas_temp)^(1.5) * 1/(_pressure*sigma^2*collions_intergral)
42      reduction = (2*binary_diffusivity*_mol_weight_vapor*_vapor_pressure)/(
            _droplet_density*R*_bulk_gas_temp)
43      eva_time = _droplet_start_diameter^2 / reduction -- time the hole droplet
             is evaporated
44      squared_start_diameter = _droplet_start_diameter^2
45  end
46
47  EVA.segment.initialize_run = segment.initialize_run
48  -- SIMION initialize segment. Called on particle creation.
49  -- attach initial droplet diamater to the particles
50  function segment.initialize()
51      ion_diameter[ion_number] = _droplet_start_diameter
52  end
53  EVA.segment.initialize = segment.initialize
54
55  function segment.other_actions()
56      -- stops if time is too long
57      if (ion_time_of_flight > eva_time*1e6) then
58          return
59      end
60      local new_diameter_2 = squared_start_diameter - reduction * (
            ion_time_of_flight/1e6)
61      if (new_diameter_2 > 0) then
62          new_diameter = math.sqrt(new_diameter_2)
63      else
64          return
65      end
66      ion_diameter[ion_number] = new_diameter
67      -- log the new ion diameter with corresponding ID (= ion number) and TOF
```

```
68      if (_evaporation_record == 1) then
69          print('##',ion_number, ion_time_of_flight/1e6, ion_diameter[
                ion_number])
70      end
71  end
72  EVA.segment.other_actions = segment.other_actions
73
74  return EVA
75  -- References: Evaporation model:
76  -- Davis, E.J, 1992. Microchemical Engineering: The Physics and Chemistry of
77  -- the Microparticle. Advances in Chemical Engineering, Elsevier, pp.1-94
```

B.2. E-Field Fix

Listing B.2: fix_efield.h

```cpp
1   #ifdef FIX_CLASS
2   FixStyle(efield,FixEfield)
3   #else
4
5   #ifndef SPARTA_FIX_EFIELD_H
6   #define SPARTA_FIX_EFIELD_H
7   #include "fix.h"
8   #include "particle.h"
9
10  namespace SPARTA_NS
11  {
12      class FixEfield : public Fix {
13          public:
14              struct Vec3
15              {
16                  double x;
17                  double y;
18                  double z;
19              };
20              FixEfield(class SPARTA *, int, char **);
21              ~FixEfield();
22              int setmask() override;
23              void init() override;
24              void start_of_step() override;    // called at the beginning of
                    timestep
25              void perform();
26              void calc_velocity(Particle::OnePart *);    // calculate new
                    volcitys
```

```
27
28        protected:
29            Vec3 efield;                              // efield vectors
30            Vec3 force;                               // resulting force
31            Vec3 acceleration;                        // resultion
                  acceleration
32            double q;                                 // charge Q
33            double mass;                              // mass
34            double dt;                                // timestep
35            const double e = 1.602176634e-19;         // elementary
                  charge
36
37        private:
38            int ionspecies;            // index of ion species
39     };
40  } // namespace SPARTA_NS
41  #endif
42  #endif
```

Listing B.3: fix_efield.cpp

```
1   #include "math.h"
2   #include "stdlib.h"
3   #include "string.h"
4   #include "fix_efield.h"
5   #include "update.h"
6   #include "particle.h"
7   #include "error.h"
8
9   using namespace SPARTA_NS;
10  /* ------------------------------------------------------------------ */
11
12  enum Param : int
13  {
14      FixID = 0,
15      FixName,    // efield
16      EX,         // electricfieldvector in x-direction
17      EY,         // electricfieldvector in y-direction
18      EZ,         // electricfieldvector in z-direction
19      Species     // effected species
20  };
21
22  FixEfield::FixEfield(SPARTA *sparta, int narg, char **arg)
23      : Fix(sparta, narg, arg)
```

```
24  {
25      if (narg < 5)
26      {
27          error->all(FLERR,"Illegal fix efield command");
28      }
29
30      per_particle_flag = 1;      // 0/1 if per-particle data is stored
31      time_depend = 0;            // 1 if requires continuous timestepping
32      vector_flag = 0;            // 0/1 if compute_vector() function exists
33
34      // check if selected species is defined
35      ionspecies = particle->find_species(arg[Param::Species]);
36      if (ionspecies < 0)
37      {
38          error->all(FLERR, "Fix efield species does not exist");
39      }
40      // check if seleceted speciecs is charged
41      if (particle->species[ionspecies].charge == 0.0)
42      {
43          error->all(FLERR,"Fix efield ion species has charge == 0.0");
44      }
45
46      // assign args to variables
47      // checking if Efield-parameter is NaN (f != f is true, f is NaN)
48      efield.x = atof(arg[Param::EX]);
49      if (efield.x != efield.x)
50      {
51          error->all(FLERR,"Illegal fix efield command. Efield value (x) is NaN
                ");
52      }
53      efield.y = atof(arg[Param::EY]);
54      if (efield.y != efield.y)
55      {
56          error->all(FLERR,"Illegal fix efield command. Efield value (y) is NaN
                ");
57      }
58      efield.z = atof(arg[Param::EZ]);
59      if (efield.z != efield.z)
60      {
61          error->all(FLERR,"Illegal fix efield command. Efield value (z) is NaN
                ");
62      }
63
64      // Charge q of ion effected ion species
```

```
65      q = particle->species[ionspecies].charge * e;
66      // mass of ionspecies
67      mass = particle->species[ionspecies].mass;
68      // Timestep
69      dt = update->dt;
70      // Calculate the force
71      force.x = efield.x * q;
72      force.y = efield.y * q;
73      force.z = efield.z * q;
74      // Calculate acceleration of ions
75      acceleration.x = force.x / mass;
76      acceleration.y = force.y / mass;
77      acceleration.z = force.z / mass;
78   }
79   /* ---------------------------------------------------------------------- */
80   FixEfield::~FixEfield()
81   {
82
83   }
84   /* ---------------------------------------------------------------------- */
85   int FixEfield::setmask()
86   {
87     int mask = 0;
88     mask |= START_OF_STEP;
89     return mask;
90   }
91   /* ---------------------------------------------------------------------- */
92   void FixEfield::init()
93   {
94
95   }
96   /* ---------------------------------------------------------------------- */
97   void FixEfield::calc_velocity(Particle::OnePart *ip)
98   {
99       double *vi = ip->v;
100
101      constexpr int x = 0;
102      constexpr int y = 1;
103      constexpr int z = 2;
104
105      vi[x] += acceleration.x * dt;
106      vi[y] += acceleration.y * dt;
107      vi[z] += acceleration.z * dt;
108
```

143

B. Appendix B

```
109  }
110  /* ---------------------------------------------------------------------- */
111  void FixEfield::perform()
112  {
113      Particle::OnePart *particles = particle->particles;
114      int pnlocal = particle->nlocal;
115
116      for (int i = 0; i < pnlocal; i++)
117      {
118          if (particles[i].ispecies != ionspecies)
119          {
120              continue;
121          } else
122          {
123              calc_velocity(&particles[i]);
124          }
125      }
126  }
127  /* --------------------------------------------------------------------
128      callled at echt start of a timestep
129      ---------------------------------------------------------------- */
130  void FixEfield::start_of_step()
131  {
132      perform();
133  }
134  /* ---------------------------------------------------------------------- */
```